OPEN ACCESS

University of BRISTOL

This electronic thesis or dissertation has been downloaded from Explore Bristol Research, http://research-information.bristol.ac.uk

Author:
Mason, Joanna

Title:
Nonsmooth models of gear rattle in roots booster pumps

General rights
Access to the thesis is subject to the Creative Commons Attribution - NonCommercial-No Derivatives 4.0 International Public License. A copy of this may be found at https://creativecommons.org/licenses/by-nc-nd/4.0/legalcode This license sets out your rights and the restrictions that apply to your access to the thesis so it is important you read this before proceeding.

Take down policy
Some pages of this thesis may have been removed for copyright restrictions prior to having it been deposited in Explore Bristol Research. However, if you have discovered material within the thesis that you consider to be unlawful e.g. breaches of copyright (either yours or that of a third party) or any other law, including but not limited to those relating to patent, trademark, confidentiality, data protection, obscenity, defamation, libel, then please contact collections-metadata@bristol.ac.uk and include the following information in your message:

• Your contact details
• Bibliographic details for the item, including a URL
• An outline nature of the complaint

Your claim will be investigated and, where appropriate, the item in question will be removed from public view as soon as possible.

Nonsmooth Models of Gear Rattle in Roots Booster Pumps

Joanna Mason

Department of Engineering Mathematics

University of Bristol

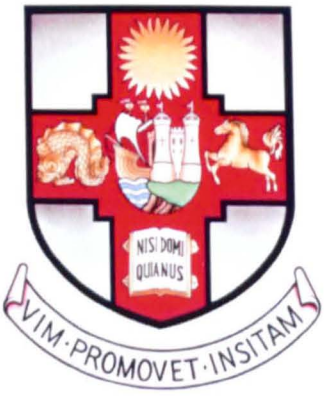

A dissertation submitted to the University of Bristol in accordance with the requirements of the degree of Doctor of Philosophy in the Faculty of Engineering.

September 2008

Paginated blank pages are scanned as found in original thesis

No information is missing

Abstract

This thesis is concerned with the study of gear rattle in Roots blower booster pumps. The pumps exhibit several hallmarks of nonlinearity, including intermittency and a sensitive dependence on parameters.

Chapter 1 introduces the general problem background. In Chapter 2, it is described how imperfect (eccentric) gear mounting can introduce a time-dependent forcing term that operates at the same rotation rate as the gears. A second-order nonsmooth ordinary differential equation to describe the dynamics of the pump is derived, where the nonlinearity arises from the backlash clearance between the gear teeth. A piecewise linear stiffness model and a simpler infinite stiffness impacting limit are introduced. In addition, the methodologies for the calculation of linear 'silent' solutions, and the construction of noisy rattling solutions are outlined. It is found that noisy solutions can coexist with silent ones, providing a possible explanation of why these systems can rattle intermittently.

The model is examined in more detail in Chapter 3 where basins of attraction are computed using cell-to-cell mapping techniques. Rich and delicate dynamics are revealed, and some of the transitions in the system's behaviour are analysed in terms of both smooth and discontinuity-induced bifurcations. The intricate stretching and folding of phase space is illustrated via computations of the grazing curve, and its preimages, and via manifold computations of basin boundaries using DsTool (Dynamical Systems Toolkit).

Chapters 4 and 5 develop and analyse more complicated models for design innovations which attempt to reduce the gear rattle. The effects of (i) breaking the symmetry of the machine, (ii) mounting the driving gear on its shaft by means of a torsional spring, and finally, (iii) the addition of a type of tuned vibration absorber are investigated. A blend of both linear and nonlinear techniques are used and the relative merits of each design solution are compared.

Finally, Chapter 6 presents conclusions and outlines areas for future work.

Acknowledgements

My sincere thanks to Eddie Wilson and Martin Homer for being such erudite and understanding supervisors - I have learnt a lot!

I am indebted to both former and current members of the Bristol Laboratory for Advanced Dynamics Engineering, especially Petri Piiroinen, James Ottewill, and my desk mates Tom Melvin and Jon 'Keano' Ward. I thank my family and friends for providing welcome distractions; particularly the Deb Phelps, Hannah 'Wollard' Woollard, Emma Carolan, Emma Doyle, Georgia Hamlin, Hannah Thorpe and Isabella Percy, for the zoo megamixes, pirate badgers and ginger beer. Thank you to Howell for his unwavering love and encouragement through the crises and the celebrations.

I gratefully acknowledge a CASE award from BOC Edwards Ltd and the Engineering and Physical Sciences Research Council.

Author's Declaration

I declare that the work in this dissertation was carried out in accordance with the regulations of the University of Bristol. The work is original except where indicated by special reference in the text and no part of the dissertation has been submitted for any other degree.

Any views expressed in the dissertation are those of the author and in no way represent those of the University of Bristol.

The dissertation has not been presented to any other University for examination either in the United Kingdom or overseas.

Signed: Joanna Mason

Dated: 7/2/09

Contents

Contents

List of Tables

List of Figures

Chapter 1

Introduction

1.1 Problem background

This thesis presents a mathematics in industry problem which originated in consultancy work commissioned by BOC Edwards Ltd (BOCE), in the summer of 2003 [57, 58]. BOCE (known as Edwards Ltd since July 2007) is a leading supplier of vacuum systems for science and industry [1].

In common with other manufacturers, BOCE have experienced unexplained and intermittent noise and vibration problems during the development of some of their booster pump products. Recent increases in the sizes and operating speeds of the pumps are thought to be the cause of the problem, which originates in the pumps' gearing mechanism [57, 58]. Indeed gear rattle is a rather widespread problem in rotating machinery with high inertia and high stiffness, but low damping. In this thesis we are concerned with understanding the underlying mathematics of gear rattle, as well as developing potential design solutions for booster pumps.

Gears are typically manufactured with a clearance between their teeth, known as the *backlash*, to ensure that they will not jam. Perfect concentric mounting of the gears on their shafts is not possible: tiny amounts of eccentricity introduce an oscillatory forcing effect which causes gear teeth to rattle within their clearance: an effect known as *backlash oscillation*. The rattle that we consider is an *order vibration*, in that its dominant frequency is the gross rotation rate of the machine. (Other types of manufacturing error can lead to gear rattle at the tooth-meshing frequency [34].) The practical challenge is to improve machine design so that it is less susceptible to noisy operation driven by eccentricity.

Our approach is that of a mathematical modeller: we attempt to identify the key parameters and capture the essential dynamics using simplified low degree-of-freedom models. We then analyse how to improve practical machines by analysing the dynamics' dependence on design parameters. Throughout this thesis there is a strong flavour of

both linear and nonlinear dynamics. We employ a combination of explicit construction, asymptotic methods, bifurcation theory and numerical techniques to classify complicated dynamic behaviour in realistic parameter regimes.

The remainder of this Introduction is organised as follows. To motivate the problem we begin with a broad summary of vacuum systems and their applications in industry in Section 1.2. We present a discussion of oil-free pumps in Section 1.3, focussing in particular on the two most common mechanisms: the claw and the Roots. To study systems with nonlinearities, such as backlash, we require some knowledge of *piecewise-smooth* dynamical systems. We give a brief introduction to such systems in Section 1.4. Finally, in Section 1.5 we give an outline of the thesis.

1.2 Vacuum systems in science and industry

Vacuum pumps are used in the manufacture of microelectronics devices, including scientific instruments, solar cells and flat-panel displays. However, the bulk of BOCE's vacuum pump sales are to the semiconductor industry. We proceed to outline an example industrial vacuum process.

Chemical Vapour Deposition (CVD) is a chemical process for depositing thin films of various materials. CVD is widely used in the semiconductor industry, as part of the semiconductor device fabrication process. In a typical CVD process the substrate (or wafer) is exposed to one or more gaseous precursors. The desired deposit is produced by reaction or decomposition on the substrate surface.

Most modern CVD process are carried out at sub-atmospheric pressures, since this gives more even film thickness. For example, Ultra-High Vacuum CVD processes are typically below 10^{-7} millibars, and therefore require sophisticated systems of pumps to maintain the vacuum and remove waste gases. There exist many different types of individual pump, each of which is designed to be optimal for a certain pressure range, see Figure 1.1. This thesis focuses on booster pumps, which operate in a pressure range of a few to 10^{-3} millibars (approximately 10^{-3} to 10^{-6} atmospheres). Boosters are a type of positive displacement pump; they trap and transport a fixed volume from an inlet port to an outlet (or exhaust) port.

Conventionally, pump chambers are lubricated with oil to provide sealing in the swept volume. However, semiconductor processes are chemically very sensitive to small amounts of oil vapour, and there is the further possibility of the degradation of the lubricant. In 1984, in response to the increasingly stringent requirements of the semiconductor industry, the first commercial *dry pumps* were launched [56]. The term dry

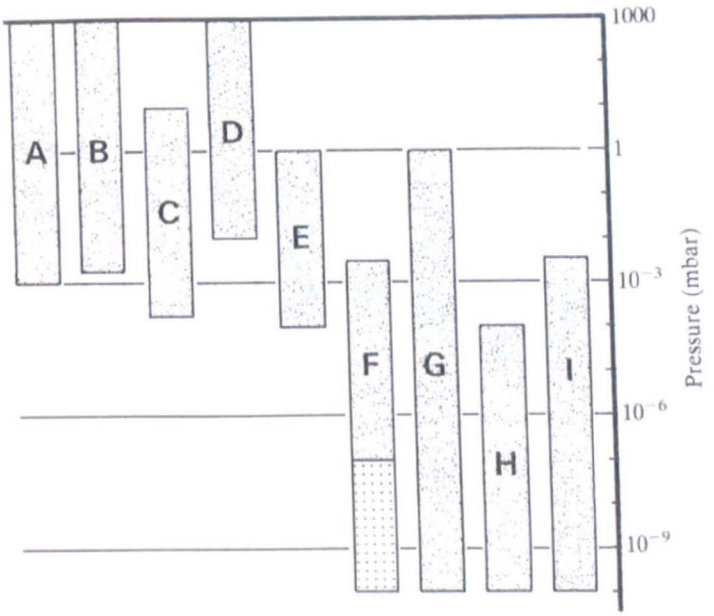

KEY	PUMP
A	Sorption
B	Mechanical rotary
C	Mechanical booster (normally used with a rotary pump)
D	'Dry pump'
E	Vapour booster
F	Diffusion (low pressures obtained with accessories)
G	Turbomolecular
H	Ion
I	Cryo

Figure 1.1. Typical vacuum pump operating ranges from atmospheric pressure down to 10^{-12} millibars. Reproduced from *Modern Vacuum Practice* by N.S. Harris (McGraw-Hill 1990) [25].

pump describes a positive displacement pump in which the swept volume is free of lubricants and sealing fluids. We continue our background discussion by giving some basic detail of how dry pumps work.

1.3 Dry pump mechanisms

A variety of different dry pump mechanisms exist. These include Roots, claw, scroll, screw compressor and reciprocating piston pumps [22]. Each pump type has its own optimal compression ratio and maximum flow rate. Combinations of Roots and claw mechanisms are common in semiconductor industry applications. By arranging the Roots and claw stages such that each works in the pressure region at which its performance is optimal, see Figure 1.2, high throughput with low power input is achieved at low pressure [59]. See Figure 1.3 for an example of such a multistage pump.

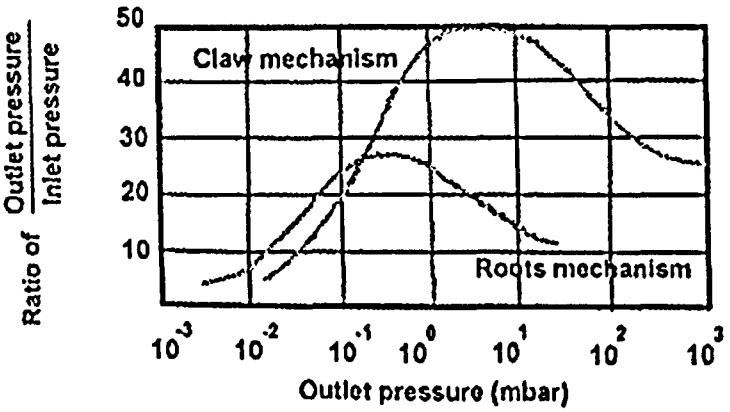

Figure 1.2. Attainable pressure ratio (for air) for a claw and Roots mechanism, as a function of outlet pressure with no gas throughput. Above 0.5 millibars the claw mechanism produces higher compression ratios than the Roots. The Roots is used at the inlet stages, at pressures in the region of 10^{-2} millibars. Reproduced from the BOCE training handout *Dry Pumps and Boosters* from the "Practical Vacuum Technology" course [2].

The common feature of both Roots and claw pumps is a system of counter-rotating rotors, with parallel shafts, which are 1:1 geared so that their motions are synchronous. The gears and drive mechanisms are lubricated outside the swept volume so as to avoid contamination. The rotors themselves are rigid bodies with uniform cross-section in planes perpendicular to the shafts. Consequently, the cross-section of the pumping chamber itself is the overlapping union of two discs. Further, the rotors themselves, which usually have the same cross-section up to symmetry, must rotate so as to trap gas (i.e., there must be a small clearance distance between them at all times), but not to collide. This implies that rotors must be designed with a particular geometry so that their surfaces 'sweep over each other' as they rotate. See [26] for a review of the geometric principles involved in rotor design.

1.3.1 Claw mechanism

The claw mechanism, unlike the Roots, is a true compressor. The name is derived from the geometry: it is cylindrical for most of the circumference, but is interrupted by a deep depression followed by a protruding 'claw'. During rotation the claw from one rotor enters the depression from the other, and vice versa. The rotors also have a valve function as the inlet and exhaust ports are periodically opened and closed. As one section of the pumping chamber compresses and exhausts the gas, the other section is open to the inlet and fills up with gas. The claw pumping mechanism achieves a high compression ratio, due to the combination of compression and valve function, at the expense of high throughput. Due to this compression the pump gearbox normally

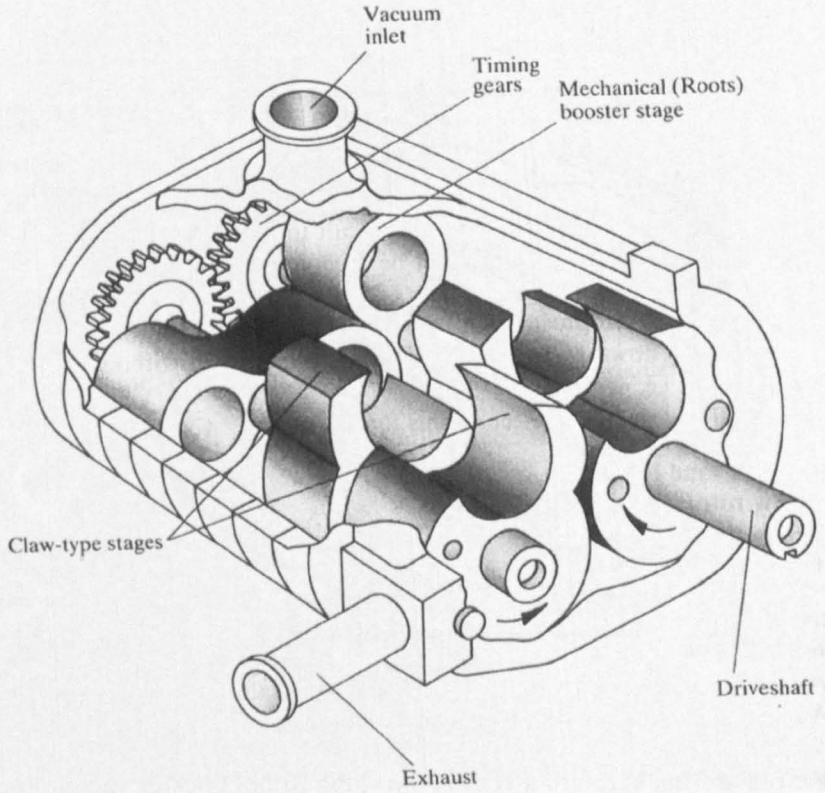

Figure 1.3. A cut-away view of a three-stage pump, with one Roots and two claw-type stages. The inter-meshing pairs of Roots and claw rotors are mounted on common shafts and synchronised by timing gears. Reproduced from *Modern Vacuum Practice* by N.S. Harris (McGraw-Hill 1990) [25].

carries a high torque, and therefore gear rattle rarely occurs in pumps which incorporate a claw stage.

1.3.2 Roots mechanism

The Roots mechanism, or booster pump, is named after the Roots brothers of Indiana, who patented the design in 1860 for use in blast furnaces, mine ventilation, and other industrial applications. It is a compact and efficient mechanism for compression and delivery of large volumes of gas at low pressures [26]. It uses two counter-rotating rotors, each of which has two or more rotating lobes. Rotors with three-lobes are more often used at higher pressures.

The rotors (when two-lobed) are shaped rather like a 'figure of eight' and are constrained in a chamber, see Figure 1.4 for a cross-section through a typical two-lobe pump. The stages in one cycle of the Roots pumping mechanism are shown schematically in Figure 1.5. The Roots booster traps a volume of fluid at low pressure, see Figure

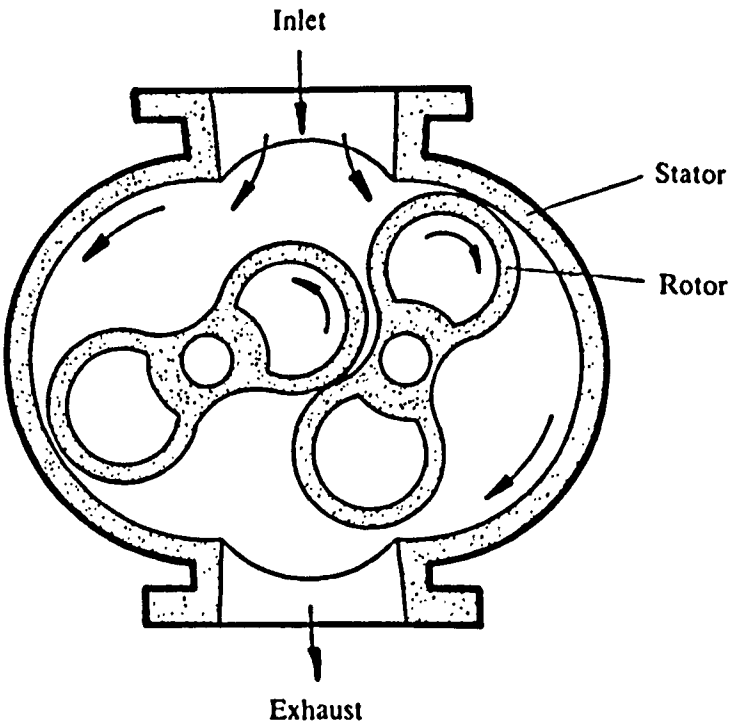

Figure 1.4. A cross-section through a typical two-lobe Roots booster vacuum pump. The two figure of eight rotors (sometimes referred to as impellers) are synchronised by external timing gears (not shown). The rotors rotate in opposite directions, and they never contact each other, or the stator walls. Reproduced from *Modern Vacuum Practice* by N.S. Harris (McGraw-Hill 1990) [25].

1.5(b), and transfers this volume, shown in Figures 1.5 (c) and (d), without compression. In the final stage, the trapped volume is squeezed by the backward motion of the other impeller, shown in Figure 1.5(e), and the now compressed fluid is ejected to the high pressure region (f).

In high-vacuum applications the Roots mechanism is never used alone. Rather, its high pumping speed can be employed to increase (boost) the pumping speed of other vacuum pumps in the medium to low vacuum range. Typical booster pumps that we consider are single stage, water-cooled, positive displacement Roots booster pumps, with two lobes per rotor. However, the evolution of pump design has led to an undesirable noise and vibration problem, which motivates the work in this thesis.

1.4 Piecewise-smooth systems

As outlined in Section 1.1, rattle is a generic problem in lightly-loaded geared systems. Halse [23, 24] was sponsored by Jaguar Cars and was interested in the underlying

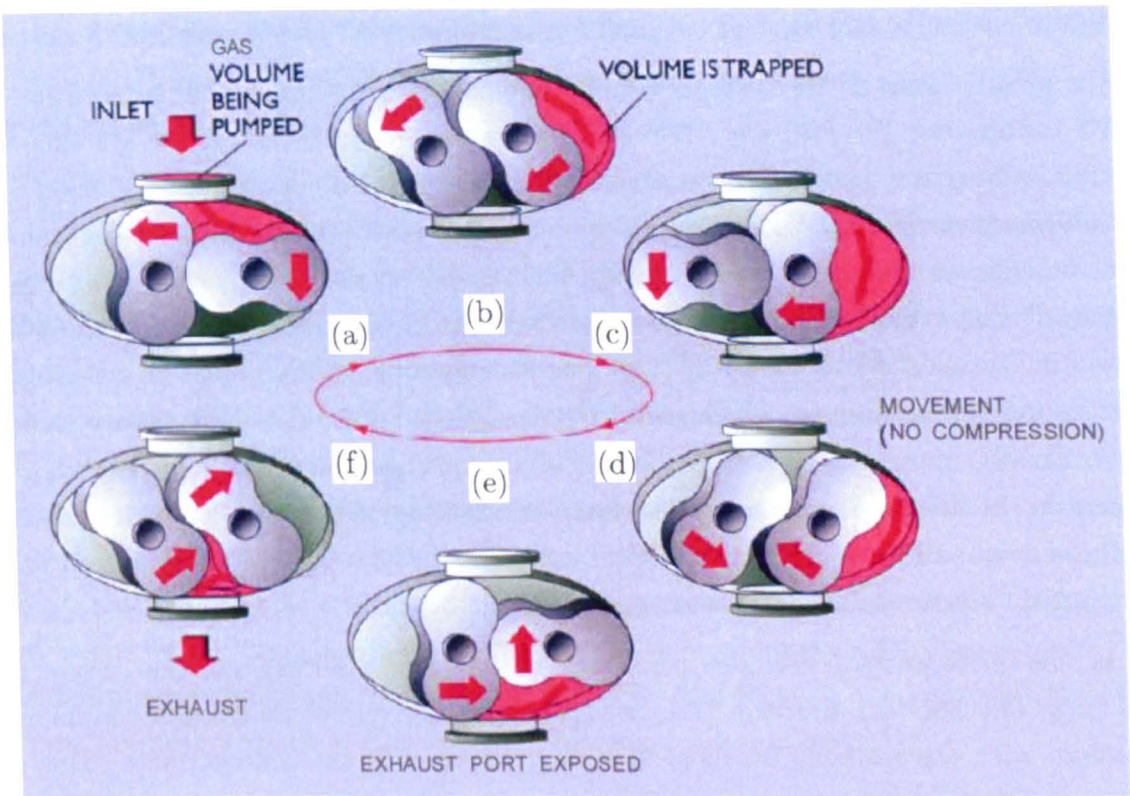

Figure 1.5. The pumping mechanism of a two-lobe Roots type booster. During each rotation the two rotors trap a specified amount of gas in the gaps between them, and push it against the stator as they rotate towards the exhaust port. Reproduced from The Technology of Dry Vacuum Pumps, from the website of Edwards Ltd `http://www.edwardsvacuum.com/` [1].

dynamics of the unloaded gear pairs used in manual automotive transmissions. He proposed a prototype model to investigate the oscillatory forcing effect introduced by the torque cycle of the engine. We build on this model, with the difference that the oscillatory forcing effect in Roots boosters is caused by eccentric mounting of the gears. Our most basic model is a simple low degree-of-freedom oscillator, with a nonlinearity arising from the backlash between the gear teeth. This *backlash nonlinearity* describes the restoring force between two gears and takes the form

$$B(\Phi) = \begin{cases} \Phi - \beta, & \Phi \geq +\beta, \\ 0, & |\Phi| < \beta, \\ \Phi + \beta, & \Phi \leq -\beta, \end{cases} \tag{1.1}$$

where Φ describes the relative rotational displacement of the gears and 2β is the backlash width. Formula (1.1) is an example of a *piecewise-smooth* (PWS) function. PWS systems occur in many diverse applications in nature, biology, engineering and electronics. Examples include suspension bridge dynamics [18] and the DC/DC buck converter

(a power electronic circuit) [16] (see [17] for a comprehensive review of this area).

In broad terms, PWS systems can be categorised into three different types: (i) *PWS continuous*, (ii) *Filippov PWS* and (iii) *impacting systems*. These systems are regular in every way except at prescribed codimension one sets in phase space, known as *discontinuity surfaces*. PWS continuous systems have vector fields which are continuous but not differentiable at the discontinuity surface, giving rise to only mild irregularity in the solution orbits. In Filippov systems, the vector field is fully discontinuous at the discontinuity surface, in such a way that the definition of a solution must be generalised to allow for *sliding solutions* which are constrained to lie within the discontinuity surface itself. Finally, impacting systems are a kind of 'hybrid' between smooth and nonsmooth dynamics. In this case discontinuity surfaces separate permitted and forbidden regions of phase space. Between impacts the system is smooth, however at impact a reset map is required, which results in a discontinuous change of state.

In this thesis we shall consider gear rattle models that are PWS systems of type (i) and (iii). The backlash function (1.1) is an example of a piecewise-smooth continuous function, with discontinuity surfaces $\Phi = \pm\beta$, where it is not differentiable. Due to a large stiffness in our system we will also use an *impacting limit* model of backlash, where we approximate crossings of $\Phi = \pm\beta$ by instantaneous elastic impacts.

The mathematical interest is that PWS systems have the potential for both rich and complex dynamics not described by standard bifurcations (see [32] for a review). Exotic phenomena include period-adding bifurcations [17] and instantaneous jumps to chaos (without period-doubling cascades), which have led to a new theory of *discontinuity-induced* bifurcations (DIBs). The classical example of a DIB is the *grazing bifurcation* [44], which occurs when a trajectory approaches a discontinuity surface tangentially, and the way in which these organise the dynamics of our system shall form an important part of the analysis presented in Chapter 3.

1.5 Thesis outline

The outline of the thesis is as follows.

In Chapter 2 we develop our most basic gear rattle model, motivated by a Roots booster pump, and we derive a system of piecewise-smooth ordinary differential equations to describe its dynamics. We outline the methodology for finding linear (effectively silent) solutions, and describe the construction techniques that we employ in the analysis of nonlinear, rattling ('noisy') solutions. In both cases we find bounds for the existence of periodic solutions, and examine these bounds as the key design parameters are varied, with reference to realistic machine designs. In particular, we establish formulae

for the *critical eccentricity* of the gearing mechanism, above which silent operation is impossible. However, we shall see that rattling behaviour remains possible even below the critical eccentricity.

In Chapter 3 we explore parameter space in detail by computing basins of attraction for both the impacting and piecewise-linear models of backlash. Halse *et al* [23, 24] established that gear models have regions in parameter space where a large number of stable noisy (rattling) solutions can coexist with a quiet (non-rattling) solution, and so we explore this idea further. Anecdotal evidence indicates that striking a pump with a hammer can cause a noisy pump to operate more quietly, supporting the proposition that coexistence and intermittency are important in real-world pumps. Consequently, the physical importance of a solution is governed by the size of its basin of attraction, since in practice a stable solution with a small basin of attraction will be unobservable. We are particularly concerned with efficient computation of the basins of attraction, so that basins for different parameter values can easily be compared. The basins reveal rich and delicate dynamics, and we analyse some of the transitions in the system's behaviour in terms of both smooth and discontinuity-induced bifurcations.

The later chapters in the thesis propose design solutions that may increase the critical eccentricity, enhancing the likelihood of quiet operation. In Chapter 4 we generalise our basic model to allow for the moments of inertia of the parallel assemblies to be unequal. We use this model to find modified analytical bounds for the existence of various types of solution, both 'silent' and 'noisy'. In conclusion, we find that breaking the symmetry of the machine gives only a marginal improvement in its behaviour. We then develop a three degree-of-freedom model for a sprung-gear solution proposed by BOCE [10] and for which a patent has been applied [12]. In summary, the critical eccentricity may be substantially increased by this type of device but the performance in fully nonlinear regimes remains a question for future work.

In Chapter 5 we investigate the introduction of centrifugal pendulum vibration absorbers (CPVAs), [54] which employ free balancing absorbers in a circular race on the gear. CPVAs are widely used in industry for reducing unwanted vibration in a range of applications, such as light aircraft engines [42] and helicopter rotors [36, 51], but we believe that this is the first time they have been proposed to reduce gear rattle. Specifically, to explore this idea we develop a four degree-of-freedom model for the pump in a simplified situation where a CPVA is attached to one gear, with eccentricity on the other. Linear theory is used to estimate some key CPVA design parameters, and some aspects of the behaviour are then investigated by numerical simulation. The results are inconclusive, but we present several ideas for future investigation.

Finally, in Chapter 6 we present our conclusions, and outline some areas for further work.

Please note that this thesis originally contained a confidential appendix, which included material that is too commercially sensitive for the library copy of the thesis.

Chapter 2

Modelling and Basic Solution Types

Rattle is a potential problem in any geared system. In quiet operation, meshing gears are in permanent contact. However, it is impossible to operate gears which mesh perfectly; a small amount of play between the gears is essential to ensure that they will not jam. This means that a gap is designed for between the trailing face of one tooth and the leading face of the next tooth. This gap is known as the backlash, and its width is the distance that the driving gear can be rotated without moving the driven gear. Because the gear wheels can consequently lose contact (see Figure 2.1(b)), there is a range of relative rotational displacements for which there is no restoring torque between a pair of gears: this effect is known as *freeplay.*

In summary, meshing gears have one of three possible configurations at any instant: see Figure 2.1 (full details are given in [40]):

(a) X drives Y,

(b) Freeplay,

(c) Y drives X.

In quiet ('normal') operation, the gears remain in permanent contact, and the system resides permanently in regime (a), as shown in Figure 2.1(a). However, in noisy operation, the gears lose contact, and then re-establish contact with an audible impact. There are in fact two broad types of noisy operation. Starting from contact (configuration (a)), the system can pass through freeplay (configuration (b)) to torque reversal (configuration (c)) and back again; in this situation, X drives Y and Y drives X alternately with periods where the gears are not in contact. Alternatively, the system can simply oscillate between configurations (a) and (b); this corresponds to X driving Y, occasionally visiting the freeplay region. Both types are known as *backlash oscillation.* We believe that the former oscillations are the noisiest (and certainly torque reversal is highly undesirable), while the latter, although not silent, result in quieter operation.

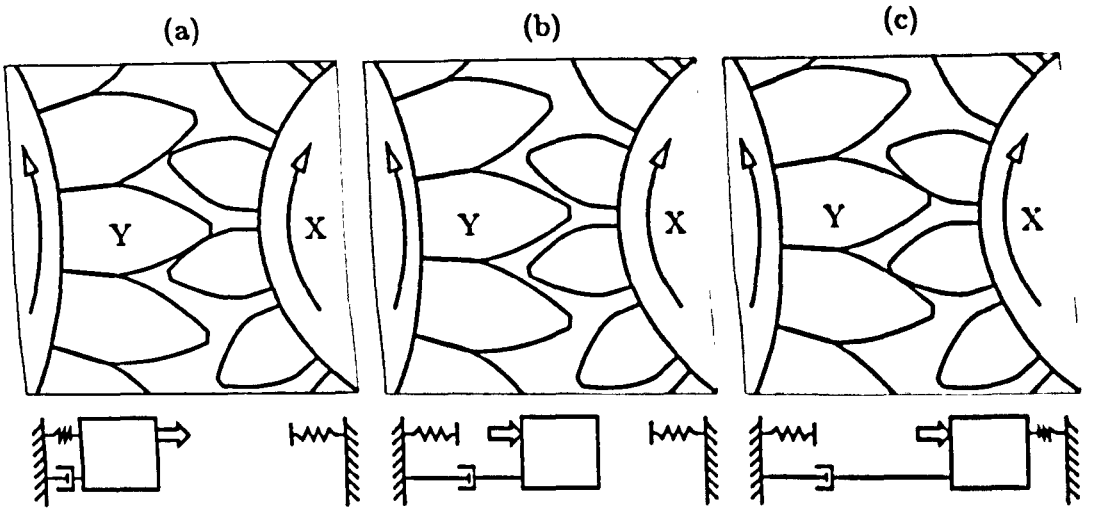

Figure 2.1. The three configurations of meshing gears. From left to right: (a) X drives Y, (b) Freeplay, (c) Y drives X. In configuration (a) the gears are in contact, with the X-shaft driving the Y-shaft. (b) illustrates *'freeplay'*; in this configuration there is no contact between the gears. (c) shows torque reversal, where the Y-shaft drives the X-shaft.

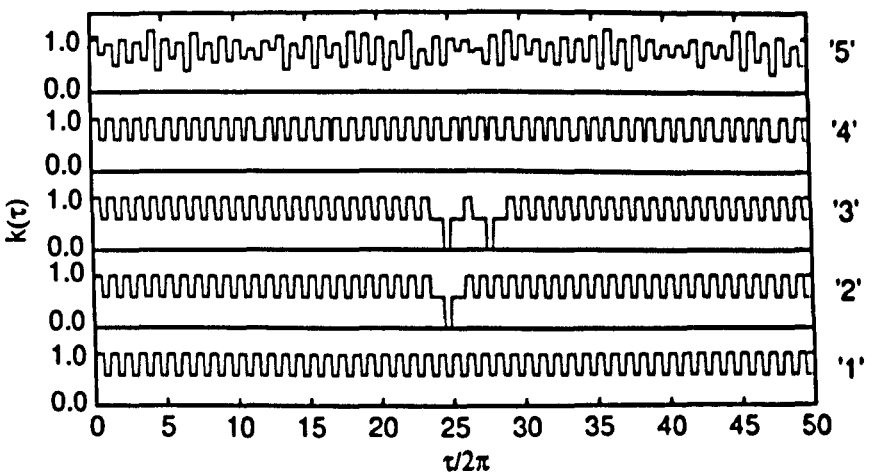

Figure 2.2. Several realizations of a time-varying meshing stiffness. '1' corresponds to a perfect gear, whilst '2' and '3' correspond to gears with one and two broken teeth, respectively. '4' has a randomised distance between increasing teeth contacts and '5' is a randomised meshing stiffness. Reproduced with permission from *Dynamics of a gear system with faults in meshing stiffness* by G. Litak and M.I. Friswell (Nonlinear Dynamics 2005) [34].

There is a large body of literature devoted to the study of geared systems, see [48, 49] for reviews. When the load and the damping are both light, only a small amount of oscillatory forcing is needed to cause rattle. Forcing due to a time-dependent stiffness operating at the tooth-meshing frequency is well-studied [29, 34, 53], see Figure 2.2.

However, motivated by experimental observations in Roots booster pumps [20] our aim is to investigate gear rattle, which is caused by periodic forcing at the gross rotation frequency; a phenomenon which we shall call *order vibration*. When compared with rattle at the tooth-meshing frequency, this produces noise and vibration with a larger amplitude but at a much lower frequency; typically, at small-integer multiples of the rate of rotation. Consequently, we assume a decoupling of timescales and neglect the periodic components in stiffness, which operate at the tooth-meshing frequency.

The outline of the chapter is as follows. Section 2.1 develops the framework for modelling Roots booster gear vibration by listing the forces at work and developing notation for the geometry. In particular we describe how imperfect gear mounting can introduce oscillatory effects which operate at the rotation rate of the gears. Section 2.2 then derives a scalar second-order ordinary differential equation for the relative displacement of the gears. This equation incorporates a piecewise-linear function to model the backlash in the gearing mechanism, which can in turn lead to interesting dynamics. This is the basic equation which we generalise and analyse in the latter parts of the thesis.

In Section 2.3 we find bounds for the existence of rattle-free solutions (where the gears reside permanently in configuration (a)). We shall refer to these solutions as *Permanent Linear Contact* (PLC) as they are confined within a range of phase space where the backlash function is wholly linear. In summary, we find a bound on the gear eccentricity above which this (almost silent) operation is impossible. This bound is of similar order to the design tolerances in many Roots booster products and we indicate how parameters may be altered to improve (increase) the bound.

Unfortunately, the existence of rattle-free solutions does not exclude the possibility that rattling (backlash oscillation) solutions may coexist at the same parameters. Therefore, in Section 2.4 we introduce a fully nonlinear analysis using both a piecewise-linear backlash function and an impacting limit to understand possible rattling behaviours.

A first version of Sections 2.1–2.4 appeared in the Master's thesis *Mathematical Modelling of Gear Rattle in Dual-Shaft Vacuum Pumps*, (2004) [37]. Material from this chapter has also been published in the Journal of Sound and Vibration (co-authors M.E. Homer and R.E. Wilson) [38].

2.1 Forces and geometry

A Roots booster pump consists of two rotors, denoted by X and Y, with a typical clearance of 250μm (for a small booster). The rotors are rigidly attached to two counter-rotating parallel shafts. The X-shaft is driven by an electric motor, while the Y-shaft

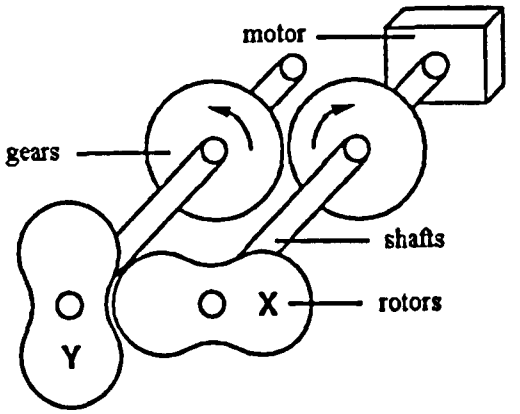

Figure 2.3. Schematic diagram of the moving parts of a Roots booster pump, illustrating the parallel arrangement of rotors, shafts and gears. Note that the only contact between the two shafts is through the gears: the rotors never collide.

is coupled by means of a 1:1 gearing mechanism. A schematic diagram of the pump is shown in Figure 2.3. For a photograph of a typical gearing mechanism, see Figure 2.4.

Here we model each shaft with its attached gear and rotor as a single rigid body. We will focus on the dynamics induced by the gearing mechanism, since earlier work [57, 58] has indicated that this is the source of noise and vibration problems. In particular, we will not attempt to analyse the fluid dynamics processes of intake and compression in detail, but rather we model the interaction between the rotors and the pumped gas with a simple linear drag model. Note that although freeplay and elastic deformation of gears and shafts imply that the pump rotors are not perfectly synchronised, the relative rotational displacement is never sufficiently large to overcome the 250μm clearance and cause the rotors to collide: the rattling originates only in the gearing mechanism of the pump.

We consider two meshing gears as shown in Figure 2.5, with the X-shaft driven by a time-dependent motor torque $T(\tau)$. We assume that the shaft centres are in the same horizontal plane, and since each gear and each rotor is balanced, we may neglect gravity since it has no resultant torque on either shaft.

To derive the equations of motion for the system, we must consider the external torques acting on the two shafts, as shown schematically in Figure 2.5. Here:

- I_X and I_Y denote the moments of inertia of the fully assembled shafts.
- r_X and r_Y correspond to the radii of the pitch circle at which contact occurs between the X- and Y-gears. We later assume the radii to be identical: $r_X = r_Y$ (which is necessary for synchronous shafts).

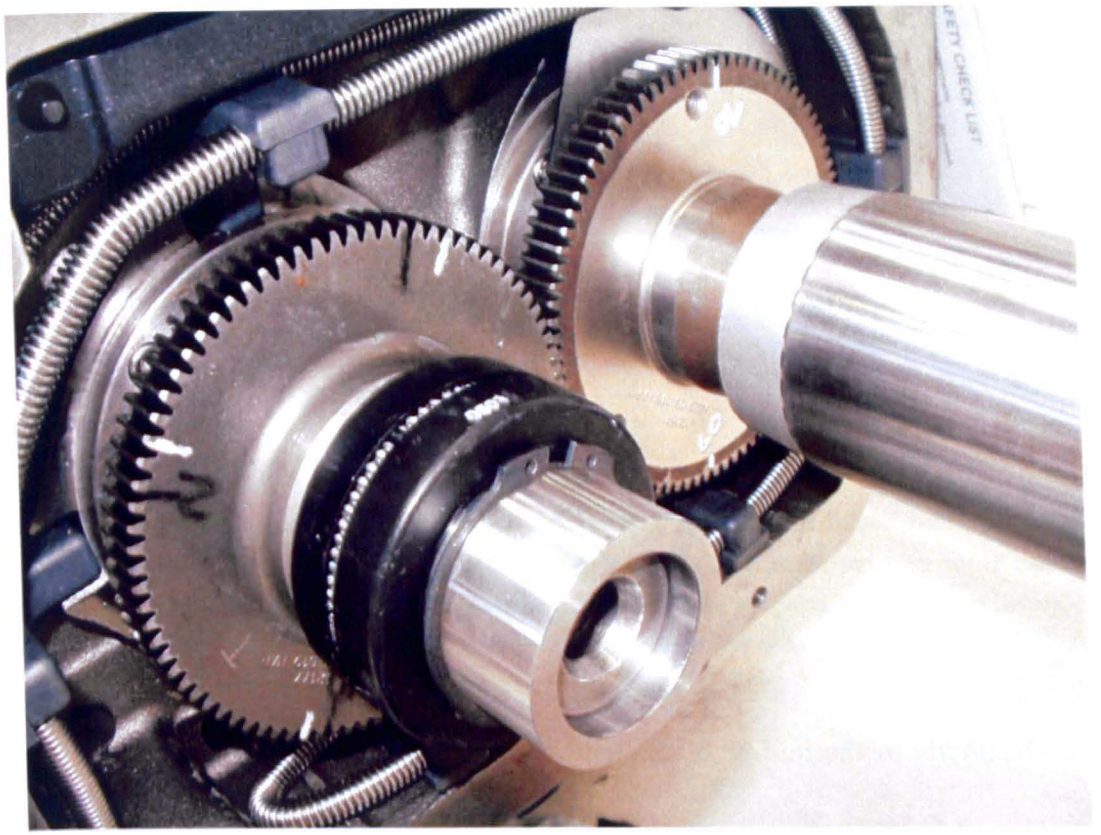

Figure 2.4. The 1:1 spur gearing mechanism in a Roots booster pump where the housing has been removed. Each gear has the same number of teeth, order 100.

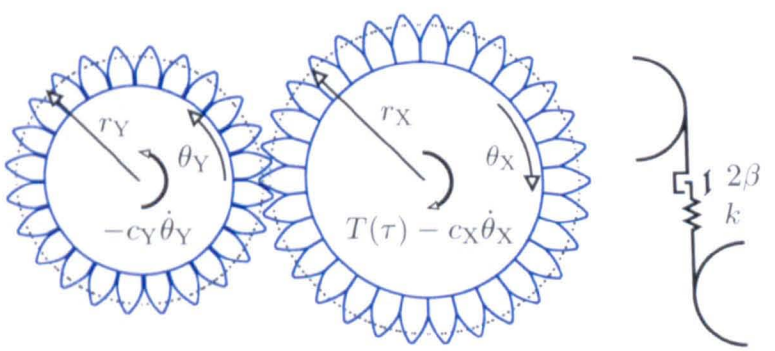

Figure 2.5. The external torques acting on the shafts of meshing gears. Here, for full generality, we suppose that the gears are of different radii, although later we shall assume the radii to be equal, so $r_X = r_Y$. The right hand side drawing illustrates the interaction force between the gears.

- θ_X and θ_Y denote the angular displacements of the two gears, with directions chosen so that both co-ordinates increase in time. The origins of θ_X and θ_Y are selected so that, in the absence of eccentricity and when $r_X = r_Y$, then $\theta_X - \theta_Y = 0$

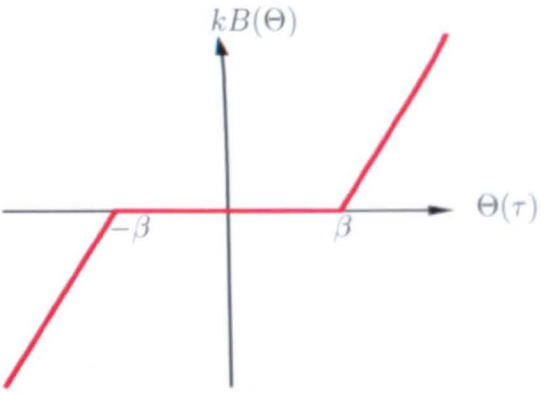

Figure 2.6. The backlash function giving the restoring force between the two gears as a function of their relative rotational displacement. When the gears are in contact Hooke's law holds, i.e., the amount of torque transmitted is proportional to the displacement.

corresponds to the middle of the freeplay region .

- c_X and c_Y are linear damping coefficients acting on the X- and Y-shafts. We assume that both the X- and Y-shafts suffer resistive torques against the direction of motion, given by $c_X\dot{\theta}_X$ and $c_Y\dot{\theta}_Y$, respectively. The linear damping terms arise from lubrication losses, friction in the seals, and a crude attempt to model the force applied in pumping the gas load. A more complicated model of the gas load would involve oscillatory terms that describe the different pumping stages outlined in Figure 1.5.

- The relative rotational displacement is defined generally by $\Theta := r_X\theta_X - r_Y\theta_Y$. For our special case $r_X = r_Y$, we work with the non-dimensional relative rotational displacement $\Theta := \theta_X - \theta_Y$.

- The stiffness coefficient k is a measure of the lumped torsional rigidity of the shaft assemblies. Each gear experiences a restoring normal reaction force kB, which we suppose for simplicity acts normal to the shafts, and which is dependent on the relative position of the gear teeth (and hence the relative rotational displacement). When the gear teeth are in contact, we use a simple 'lumped' approach and suppose that each assembly deforms according to Hooke's Law. Here B is a nonlinear backlash function, illustrated in Figure 2.6, that is made up of three linear components. We have

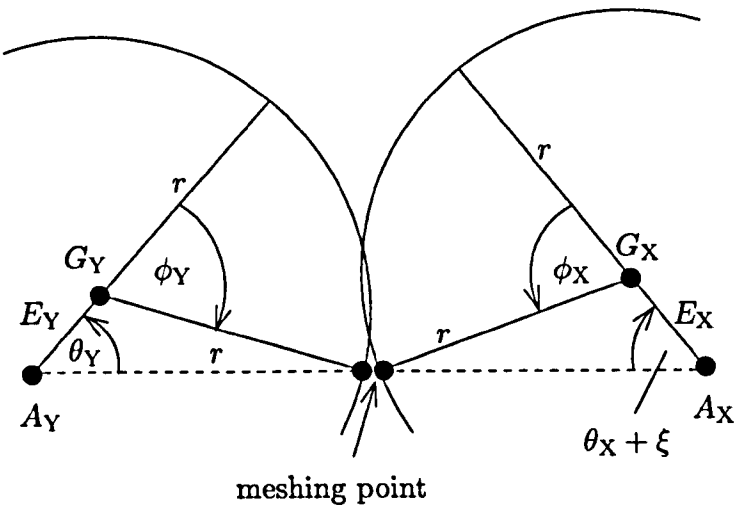

Figure 2.7. A schematic diagram of the eccentric mounting of the gears. For the purposes of visualisation the eccentricities $E_{X,Y}$ between axles $A_{X,Y}$ and geometric centres $G_{X,Y}$ of the X- and Y-gears have been severely exaggerated. Note that the meshing point lies approximately on the horizontal line containing A_X and A_Y.

$$B(\Theta) = \begin{cases} \Theta - \beta, & \Theta \geq \beta, & \text{(X drives Y)} \\ 0, & |\Theta| < \beta, & \text{(freeplay)} \\ \Theta + \beta, & \Theta \leq -\beta, & \text{(Y drives X)} \end{cases} \tag{2.1}$$

where the (non-dimensional, i.e., angular) backlash width is given by 2β. The linear sections (gradient one) correspond to Hooke's Law and the gradient zero section to freeplay. Note that the lumped description is deliberately vague about where the inertia is located and where strain occurs. A precise (and equivalent) argument is developed in full in Appendix A. Finally, this backlash function could be adjusted to incorporate other nonlinear effects, for example lubrication and friction, however these refinements are beyond the scope of this thesis.

Motivated by earlier work [57, 58], we seek forcing mechanisms which operate at the gross rotation rate of the pump. There may be several such mechanisms, but we focus on one only: eccentric mounting of the gears. In manufacture, technicians strive to mount the gears and bearings on their shafts as concentrically as they possibly can. However, perfect concentric mounting is not possible, and although typical eccentricities are only order tens of microns, this can be sufficient to drive noisy operation, irrespective of other forcing mechanisms, such as torque ripple from the drive.

We now describe the mechanism by which eccentricity introduces an oscillatory term into our equations of motion. For an eccentrically mounted gear, the co-ordinate which

describes the rotational displacement about the shaft is not the same as the angle which uniformly parameterises the outer radius of the gear at the meshing point. Whereas the rate of change of angular momentum should be expressed about the shaft, the relative rotational displacement involved in computing the meshing force should be computed at the meshing point. The goal is therefore to relate the two angles.

With reference to Figure 2.7, $E_{X,Y}$ denote the eccentricities, that is the distances between the axes of rotation $A_{X,Y}$ and the geometric centres $G_{X,Y}$ of the X- and Y-gears, respectively. E_X and E_Y are related by ξ, a constant phase angle which describes the relative orientation of the eccentricities. Here $\theta_{X,Y}$ give the angular displacement of each gear about its axis of rotation and $\phi_{X,Y}$ parametrise points on the pitch circle of each gear measured relative to the geometric centres $G_{X,Y}$, in frames which are fixed in the body of each gear. The goal is to relate $\phi_{X,Y}$ at the meshing point to the angular displacements $\theta_{X,Y}$.

The co-ordinate of a point on the rim of the X-gear measured from the axis of rotation A_X can be expressed by the Cartesian co-ordinates

$$(-E_X\cos(\xi+\theta_X)-r\cos(\xi+\theta_X-\phi_X), E_X\sin(\xi+\theta_X)+r\sin(\xi+\theta_X-\phi_X)). \quad (2.2)$$

Similarly, a co-ordinate of a point on the rim of the Y-gear measured from the axis of rotation A_Y can be expressed in the form

$$(E_Y\cos\theta_Y+r\cos(\theta_Y-\phi_Y), E_Y\sin\theta_Y+r\sin(\theta_Y-\phi_Y)). \quad (2.3)$$

We make the approximation (valid for $E_{X,Y} \ll r$) that the point of contact between the gears is in the same horizontal plane as the shaft axes $A_{X,Y}$. If we thus set the vertical displacements in equations (2.2) and (2.3) to zero and rearrange, we have

$$\sin(\xi+\theta_X-\phi_X) = -\frac{E_X}{r}\sin(\xi+\theta_X), \quad (2.4)$$

$$\sin(\theta_Y-\phi_Y) = -\frac{E_Y}{r}\sin\theta_Y. \quad (2.5)$$

Since the eccentricities $E_{X,Y}$ are small in comparison to the radii r, $\sin(\xi+\theta_X-\phi_X)$ and $\sin(\theta_Y-\phi_Y)$ are also small. This implies that $\xi+\theta_X-\phi_X$ and $\theta_Y-\phi_Y$ are also small, since other solutions are incompatible with the geometry. Therefore, applying small angle formulae, we have

$$\phi_X-\xi \simeq \frac{E_X}{r}\sin(\xi+\theta_X)+\theta_X, \quad (2.6)$$

$$\phi_Y \simeq \frac{E_Y}{r}\sin\theta_Y+\theta_Y. \quad (2.7)$$

If we define $\Theta_{\text{outer}} = \phi_X - \phi_Y - \xi$, and $\Theta_{\text{shaft}} = \theta_X - \theta_Y$, and we suppose that the dominating mean motion is $\theta_X = \theta_Y \simeq 2\pi\Omega\tau$, we obtain

$$\Theta_{\text{outer}} = \Theta_{\text{shaft}} + E\cos(2\pi\Omega\tau). \tag{2.8}$$

Here Ω is the gross rotational frequency (assumed approximately constant) and E is a non-dimensional effective eccentricity given by

$$E = \frac{1}{r}\sqrt{E_X^2 + E_Y^2 - 2E_X E_Y \cos\xi}. \tag{2.9}$$

The presence of the phase angle ξ explains anecdotal evidence [20] that a noisy machine can be made quiet by disassembling and reassembling the gears (hence altering ξ). As an extreme example, if $E_X \approx E_Y$, we may reduce rattle by matching gears with similar eccentricities and mounting them 'long axes together' so that $\xi = 0$, and we have $E \approx 0$ according to (2.9). In this set-up the four centres line up in sequence A_Y, G_Y, G_X, A_X then G_Y, A_Y, A_X, G_X half a rotation later, so that the gears move in and out with no 'shearing' effect. In comparison, $\xi = \pi$ is the worst possible situation, which maximises E according to (2.9). In this set-up, the in-out motion is minimised but the 'shearing' effect is maximised. These observations have resulted in improvements in manufacturing procedures [35].

We now move on to construct equations of motion for the two shaft assemblies, which will include the correction term for the eccentric mounting of the gears.

2.2 Equations of motion

2.2.1 Resolving torques

We apply Newton's second law of motion in angular co-ordinates (i.e., the rate of change of angular momentum is equal to the sum of the applied torques), to derive equations of motion for the two shaft assemblies.

If we consider the forces discussed in Section 2.1, for the X-shaft assembly we have

$$I_X\ddot{\theta}_X = -c_X\dot{\theta}_X - r_X g(\theta_X, \theta_Y, \tau) + T(\tau), \tag{2.10}$$

and for the Y-shaft assembly, we have

$$I_Y\ddot{\theta}_Y = -c_Y\dot{\theta}_Y + r_Y g(\theta_X, \theta_Y, \tau), \tag{2.11}$$

where dots denote differentiation with respect to time τ. Here g is the 'interaction force' between the gear teeth which we assume acts normal to the shafts, and the other notation is as introduced in Section 2.1.

Equations (2.10) and (2.11) can be rearranged to give

$$I_X\ddot{\theta}_X + c_X\dot{\theta}_X + r_X g(\theta_X, \theta_Y, \tau) = T(\tau), \tag{2.12}$$

and

$$I_Y\ddot{\theta}_Y + c_Y\dot{\theta}_Y - r_Y g(\theta_X, \theta_Y, \tau) = 0. \tag{2.13}$$

Moreover, the interaction force $g(\theta_X, \theta_Y, t)$ between the two gears is given by

$$g(\theta_X, \theta_Y, \tau) = kB(\theta_X - \theta_Y + e(\tau)), \tag{2.14}$$

i.e., a backlash function computed at the outer radius of the gear including a time-dependent term $e(\tau) = E\cos(2\pi\Omega\tau)$ to incorporate the effect of eccentricity, as described in Section 2.1.

2.2.2 Parameter estimation

We now list simplifying assumptions concerning the model parameters and we describe how they may be identified for any one given pump. The standard parameters that we use are based on a pump which we shall refer to as type A. We shall also occasionally refer to two larger pumps known as types B and C.

- We assume that the radii of the two gears are equal and from now on we shall take $r_X = r_Y =: r$. Slight eccentric mounting would imply that the radii at which the meshing force acts are unequal and time dependent, but we shall neglect this effect since eccentricity is small in comparison to the gear radii.
- The backlash may be measured by fixing one gear, whilst permitting the other to rotate within the clearance and applying the probe of a dial indicator to the surface of the movable teeth. (See [40] for further details.) In non-dimensional angular co-ordinates, we find booster pumps typically have half-backlashes in the range 4 to 8 $\times$ 10^{-4} radians.
- The combined torsional stiffness of the shaft assemblies may be measured by clamping the end of one shaft and applying torque to the other. This results in the stiffness coefficient k being a measure of the lumped torsional rigidity of the shaft assembly.

- We suppose that the damping coefficients on each shaft are identical, i.e., $c_X = c_Y =: c$. This seems to be a reasonable assumption given the symmetric construction of the machine, and enables us to estimate their value from a run-down test [20]. When the motor is switched off, we have $T(\tau) = 0$; adding the equations for the X- and Y-shaft assemblies (2.12) and (2.13) gives

$$I_X\ddot{\theta}_X + I_Y\ddot{\theta}_Y + c_X\dot{\theta}_X + c_Y\dot{\theta}_Y = 0. \tag{2.15}$$

If we take $I_X = I_Y =: I$, and $c_X = c_Y =: c$, then

$$I(\ddot{\theta}_X + \ddot{\theta}_Y) + c(\dot{\theta}_X + \dot{\theta}_Y) = 0. \tag{2.16}$$

Integration then gives

$$\dot{\theta}_X + \dot{\theta}_Y = \text{const} \times \exp\left(\frac{-c\tau}{I}\right). \tag{2.17}$$

Thus by fitting a simple exponential to a time-series of the rotation speed, the damping c may be simply determined, provided the moment of inertia I is known.

- We may model the total motor torque T by

$$T(\tau) = \overline{T} + A\cos(2\pi n\Omega\tau + \xi_{\text{motor}}), \tag{2.18}$$

where $\overline{T} > 0$ is the mean motor torque, and A (typically $\ll \overline{T}$) is the amplitude of a ripple component, due to the imperfect rotational symmetry of the armature. We find a typical ripple is of the order of a few percent of the mean torque [20]. Further $n \in \mathbb{Z}$ is a positive integer describing the order of symmetry of the armature, and ξ_{motor} is a phase constant which is required since the model also contains a time-dependent term describing the effects due to eccentricity.

- The mean torque $\overline{T}$ balances with the drag terms when the machine is running steadily, and so it need not be given as a separate parameter. To see this, let $\overline{\dot{\theta}_X}$, $\overline{\dot{\theta}_Y}$ and $\overline{g}$ denote the time-average values of $\dot{\theta}_X$, $\dot{\theta}_Y$ and g, respectively. If we assume that both shafts rotate on average at the same constant speed Ω, and average the equations for the X- and Y-shaft assemblies (2.12) and (2.13) by integrating with respect to time, we have

$$c_X\overline{\dot{\theta}_X} + r_X\overline{g} = \overline{T}, \tag{2.19}$$

and

$$c_Y\overline{\dot{\theta}_Y} - r_Y\overline{g} = 0, \tag{2.20}$$

since the time averages of the second derivatives are zero, as angular velocities are

bounded. Assuming $\overline{\dot{\theta}_X} = \overline{\dot{\theta}_Y} = 2\pi\Omega$, adding equations (2.19) and (2.20) gives

$$\overline{T} = c(\overline{\dot{\theta}_X} + \overline{\dot{\theta}_Y}) = 4\pi c\Omega, \tag{2.21}$$

and the mean torque balances the drag terms, as claimed.

2.2.3 Non-dimensionalisation

For a typical Roots booster, the moments of inertia of the two shafts differ by less than 10%. If we use the approximation that they are equal, it is possible to reduce the equations for the X- and Y-shaft assemblies (2.12) and (2.13) to a single non-autonomous second-order differential equation. Assuming that $I_X = I_Y =: I$, subtracting equation (2.13) from (2.12) yields

$$I\ddot{\Theta} + c\dot{\Theta} + 2rkB(\Theta + e(\tau)) = \overline{T} + A\cos(2\pi n\Omega\tau + \xi_{\text{motor}}), \tag{2.22}$$

where $\Theta = \theta_X - \theta_Y$ is the relative rotational displacement of the gears.

If we non-dimensionalise and use the re-normalised relative angular displacement $\Phi = \Theta + e(t)$, we are able to recast the equation of motion (2.22) in the form

$$\begin{aligned} & \Phi'' + \delta\Phi' + 2\kappa B(\Phi) \\ = \;& \alpha + \gamma\cos(2\pi nt + \xi) + e'' + \delta e' \\ = \;& 4\pi\delta - 4\pi^2\varepsilon\cos(2\pi t) - 2\pi\delta\varepsilon\sin(2\pi t) + \gamma\cos(2\pi nt + \xi), \end{aligned} \tag{2.23}$$

where we recall

$$B(\Phi) = \begin{cases} \Phi - \beta, & \Phi \geq +\beta, \\ 0, & |\Phi| < \beta, \\ \Phi + \beta, & \Phi \leq -\beta. \end{cases} \tag{2.24}$$

Here, dashes denote differentiation with respect to non-dimensional time t, and

$$t = \Omega\tau, \quad \delta = \frac{c}{\Omega I}, \quad \kappa = \frac{rk}{\Omega^2 I}, \quad \varepsilon = \frac{E}{r}, \quad \alpha = \frac{\overline{T}}{\Omega^2 I} = 4\pi\delta, \quad \gamma = \frac{A}{\Omega^2 I}. \tag{2.25}$$

The values of the non-dimensional parameters are summarised in Table 2.1. We note that:

- The rescaled damping δ, half-backlash width β and eccentricity parameter ε are small and of a similar order of magnitude $\sim 10^{-4}$. Thus they are good candidates for use as small parameters in perturbation analysis.

Quantity	symbol	value(s)
Damping constant	δ	3×10^{-4}
Torsional stiffness	κ	1100
Typical eccentricity	ε	1×10^{-4} rads
Half-backlash	β	$4-8 \times 10^{-4}$ rads
Mean motor torque	α	$4\pi\delta$ rads
Motor torque symmetry	n	$1, 2, \ldots,$
Motor torque phase	ξ	$0-2\pi$

Table 2.1. Non-dimensional parameters for the standard pump known as type A.

- In comparison, the rescaled stiffness parameter κ is large. It is tempting to write $\kappa = O(\varepsilon^{-1})$ but in fact we proceed in Section 2.4 essentially by setting $\kappa = \infty$, and replacing the linear stiffness sections of the backlash function (2.1) with instantaneous impacts governed by a law of restitution.

Next, note that we are able to directly compare the effective forcing magnitudes of torque ripple and eccentricity since they both appear as oscillatory forcing terms in the right hand side of our differential equation. Note that the ripple component γ of the mean motor torque α is very small ($\gamma \approx 3\%\,\alpha$) Hence equation (2.23) may be approximated by

$$\boxed{\Phi'' + \delta\Phi' + 2\kappa B(\Phi) = 4\pi\delta - 4\pi^2\varepsilon\cos(2\pi t) - 2\pi\delta\varepsilon\sin(2\pi t).} \tag{2.26}$$

Consequently, for the remainder of this thesis we neglect the forcing term due to torque ripple and concentrate on the effect of eccentricity only. Furthermore, observe that if we wish the right hand side of (2.26) may be further simplified by a small phase shift.

Typical numerical simulations of the initial value problem (2.24), (2.26) are shown in Figure 2.8. These numerics indicate that the system exhibits very rich dynamics, and we shall return to these simulations later in the chapter.

As it stands, (2.26) is a nonlinear second-order differential equation, with the nonlinearity arising from the $B(\Phi)$ term, (2.24). However, equation (2.26) can also be split up by the three linear regimes of B:

(a) $\Phi > \beta$ (X-shaft drives Y-shaft),

$$\Phi'' + \delta\Phi' + 2\kappa\Phi = 2\kappa\beta + 4\pi\delta - 4\pi^2\varepsilon\cos(2\pi t) - 2\pi\delta\varepsilon\sin(2\pi t). \tag{2.27}$$

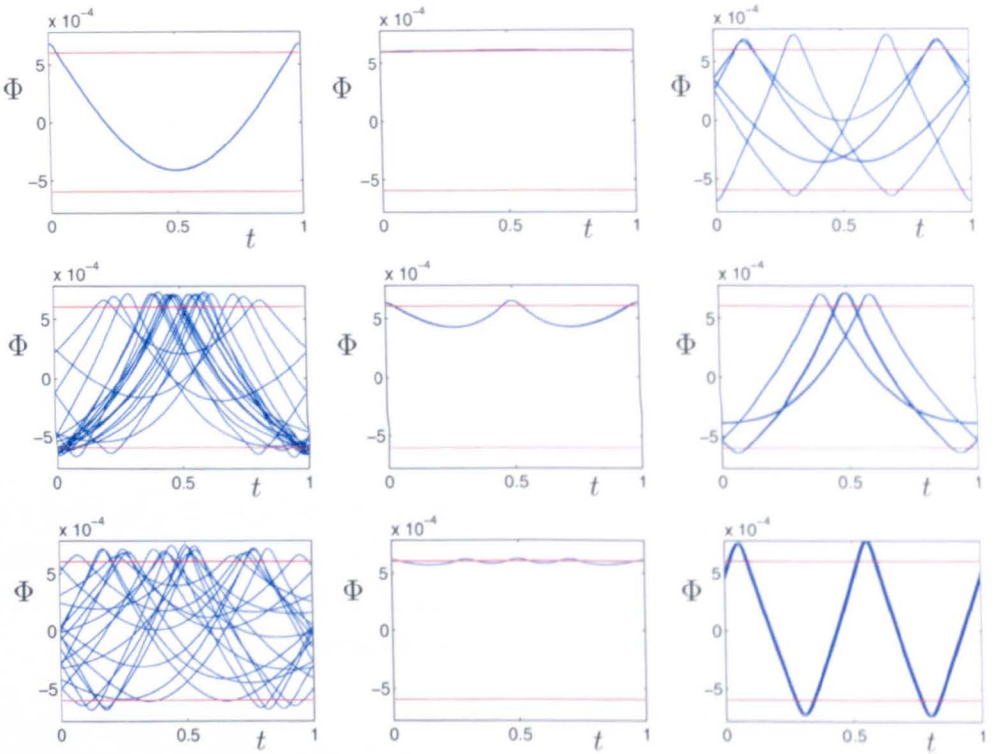

Figure 2.8. Numerical simulations of the initial value problem (2.24), (2.26) for identical machine parameters but an ensemble of initial conditions. Each graph is a plot of the relative rotational displacement $\Phi(t)$ against t, plotted over 20 gross rotations, with $\Phi = \pm\beta$ shown as horizontal lines. In each case a substantial start-up transient has been discarded. These show a mixture of noisy solutions and 'less noisy' solutions which never impact the lower backlash boundary. Note that row 1, column 2 displays a solution which at this scale is indistinguishable from $\Phi = \beta$. In fact this is a *permanent linear contact* solution where $\Phi > \beta$ for all time.

(b) $|\Phi| < \beta$ (freeplay),

$$\Phi'' + \delta\Phi' = 4\pi\delta - 4\pi^2\varepsilon\cos(2\pi t) - 2\pi\delta\varepsilon\sin(2\pi t). \tag{2.28}$$

(c) $\Phi < -\beta$ (Y-shaft drives X-shaft),

$$\Phi'' + \delta\Phi' + 2\kappa\Phi = -2\kappa\beta + 4\pi\delta - 4\pi^2\varepsilon\cos(2\pi t) - 2\pi\delta\varepsilon\sin(2\pi t). \tag{2.29}$$

Equations (2.27), (2.28) and (2.29) are *linear* second-order differential equations, which can each be solved explicitly for Φ using standard techniques. The nonlinearity in the problem arises because typically the motion will not be confined to any one of the

regimes for all time, but will swap when Φ passes through the values $\pm\beta$. Equations (2.27)–(2.29) thus constitute a nonlinear system. The exception arises when solutions remain permanently in the X drives Y regime which results in silent machine operation. (We shall later show that permanent motions in freeplay or in the Y drives X regime are not possible.)

Having derived the equations of motion for the pump, we now proceed to analyse solutions in an attempt to locate regimes of quiet and noisy operation. We shall begin in the next section by focusing on quiet solutions, where the X-shaft continuously drives the Y-shaft. In contrast, Section 2.4 is concerned with an analysis of rattling periodic orbits.

2.3 Conditions for silent operation

Recall that we have defined the three configurations of meshing gears, see Figure 2.1. For 'silent' operation the system resides permanently in regime (a), which we shall call 'permanent linear contact' (PLC) (illustrated in Figure 2.9). PLC corresponds to the X-shaft continuously driving the Y-shaft with no loss of contact between the gears, and hence no noisy re-engagement. The PLC regime is therefore highly desirable from a design point of view, and we wish to find a bound on the eccentricity, ε, for the existence of solutions in this regime. Increasing ε above this bound, which we shall call the critical eccentricity ($\varepsilon_{\text{crit}}$), will destroy the PLC solutions.

The outline of our method is as follows. In permanent linear contact the backlash function takes the form

$$B(\Phi) = \Phi - \beta \qquad \text{for all } t, \tag{2.30}$$

and the relative rotational displacement must satisfy

$$\Phi(t) > \beta \qquad \text{for all } t. \tag{2.31}$$

(see equation (2.24)).

Equation (2.30) simplifies the equations of motion (2.26) to a linear ordinary differential equation (2.27) which can be solved using standard techniques. We must, however, apply an *a posteriori* check for the validity of solutions we find, namely that (2.31) is always satisfied. This will then give the condition required on ε.

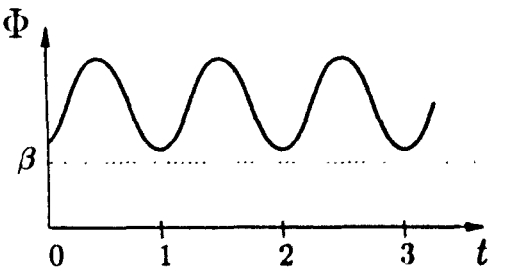

Figure 2.9. Sketch of a permanent linear contact solution. Solutions of this type correspond to the X-shaft continuously driving the Y-shaft with no loss of contact between the gears.

2.3.1 Permanent linear contact solutions

Permanent linear contact solutions of the model (2.26) satisfy

$$\Phi'' + \delta\Phi' + 2\kappa\Phi = 2\kappa\beta + \alpha - 4\pi^2\varepsilon\cos 2\pi t - 2\pi\delta\varepsilon\sin 2\pi t. \tag{2.32}$$

The solution of (2.32) consists of a particular solution in the form

$$\Phi(t) = \frac{\alpha}{2\kappa} + \beta + p\cos(2\pi t + \lambda), \tag{2.33}$$

where

$$p = \pi\varepsilon\sqrt{\frac{4\pi^2 + \delta^2}{(\kappa - 2\pi^2)^2 + \pi^2\delta^2}}, \tag{2.34}$$

and λ is a phase shift, plus an exponentially decaying complementary function component which we shall neglect, since we are concerned with $t \to \infty$ dynamics.

We require that equation (2.31) is satisfied, that is,

$$\frac{\alpha}{2\kappa} + p\cos(2\pi t + \lambda) > 0 \qquad \text{for all } t. \tag{2.35}$$

The minimum of the LHS in (2.35) is $\alpha/2\kappa - |p|$, and so we require $|p| < \alpha/2\kappa$. Using $\alpha = 4\pi\delta$, and rearranging, we obtain

$$\boxed{\varepsilon < \varepsilon_{\text{crit}} := \frac{2\delta}{\kappa}\sqrt{\frac{(\kappa - 2\pi^2)^2 + \pi^2\delta^2}{4\pi^2 + \delta^2}},} \tag{2.36}$$

as an upper bound on the eccentricity, ε, for the existence of the PLC solution. Increasing ε above this bound will destroy the PLC solution, force nonlinear solutions and guarantee noisy pump operation.

Booster type	Critical eccentricity
A	9.2×10^{-5} rads
B	6.5×10^{-5} rads
C	4.2×10^{-5} rads

Table 2.2. Calculated (non-dimensional) critical eccentricities for booster pumps of types A, B and C.

2.3.2 Commentary

If we use the parameter values from Table 2.1 in formula (2.36) we find that for our standard type A booster pump, $\varepsilon_{\text{crit}} = 9.2 \times 10^{-5}$ rads is the critical value of eccentricity above which the permanent linear contact solution cannot exist. It is curious to note that a typical measured eccentricity, 1×10^{-4} rads, is of the same order of magnitude as the critical eccentricity. This could explain why the same machine can behave inconsistently and 'identical' machines behave differently, since the PLC solution can be eliminated with a small change in the typical machine parameters.

As $\kappa \to \infty$, (motivated by the values in Table 2.1) we have

$$\varepsilon_{\text{crit}} \sim \frac{\delta}{\pi} \quad + \quad \text{higher order terms} \tag{2.37}$$

(as $\delta = 3 \times 10^{-4}$, see Table 2.1, this consolidates our calculated value for $\varepsilon_{\text{crit}}$).

We have also used (2.36) to calculate critical eccentricity values for two larger booster pumps known as types B and C. The results of these calculations are shown in Table 2.2. We find that increasing the inertia decreases $\varepsilon_{\text{crit}}$ and will therefore make rattle more likely. These calculations corroborate the anecdotal evidence that larger pumps are more susceptible to noise.

Expression (2.37) implies that if we can implement changes in the machine which increase the damping coefficients, we increase the critical eccentricity for 'silent operation' and therefore the likelihood that pumps operate 'quietly'. There are three potential ways to increase the damping coefficient, δ:

- Use more viscous lubrication in the gears. However, this is not a practical solution as power consumption is directly proportional to the damping, and increasing δ would make the machine more expensive to run.
- Decreasing the rotational speed Ω increases δ (see the rescaling formulae (2.25)), but this is not desirable as it would result in a lower pumping rate.

- Decrease the moment of inertia I. We shall return to this idea in Chapter 4.

However, it is important to note that satisfying the critical eccentricity bound (2.36) does not necessarily guarantee silent operation since there may exist a whole range of rattling solutions which coexist with the permanent linear contact solution.

2.4 Rattling solutions

In Section 2.3 we discussed permanent linear contact solutions, where the X-shaft continuously drives the Y-shaft with no loss of contact between the gears. However, although these solutions are desirable as they result in almost silent machine operation, the machine may operate in other ways, and indeed must do so if the eccentricity exceeds its critical value.

We now proceed to analyse periodic solutions where the gears do not remain permanently in contact. The constructions that we present here originate with Halse [23, 24]. Figure 2.8 shows some numerical simulations of the initial value problem for a realistic range of machine parameters (for which silent PLC solutions exist), where a variety of different initial data have been chosen. The figures were generated using the in-built Matlab ODE solver, ODE45, in conjunction with an 'Events' function to detect the crossings of the backlash boundaries [4]. The purpose of the event detection is to determine which regime the system is operating in, and therefore which case of equations (2.27)–(2.29) is to be solved.

Figure 2.8 reveals a very rich structure of coexisting rattling behaviours including stable periodic orbits, chaotic solutions etc., that coexist with quiet operation. Here we construct rattling periodic solutions, whilst in Chapter 3 we shall investigate their basins of attraction. In Figure 2.8, it would seem that noisy solutions (where the gears lose contact) predominate. We observe that these solutions spend the the majority of their time in freeplay. The large stiffness value κ (see Table 2.1) results in impact-like events of short duration. This motivates an *impacting-contact* model. We may approximate contact via the $\kappa \to \infty$ limit, namely by instantaneous elastic impacts [30] with a classical coefficient of restitution law (with coefficient of restitution $= 1$). See Figure 2.10. Thus in this case the only differential equation we need solve is (2.26) in the freeplay region, where $B(\Theta(t) + e(t)) = 0$, see equation (2.28). Therefore, as an alternative to equations (2.26), (2.24), we may analyse (2.28) with perfectly elastic impact events at times t_{imp}

$$\Phi'(t_{\text{imp}}+) = -\Phi'(t_{\text{imp}}-) \qquad \text{with} \qquad |\Phi(t_{\text{imp}})| = \beta. \tag{2.38}$$

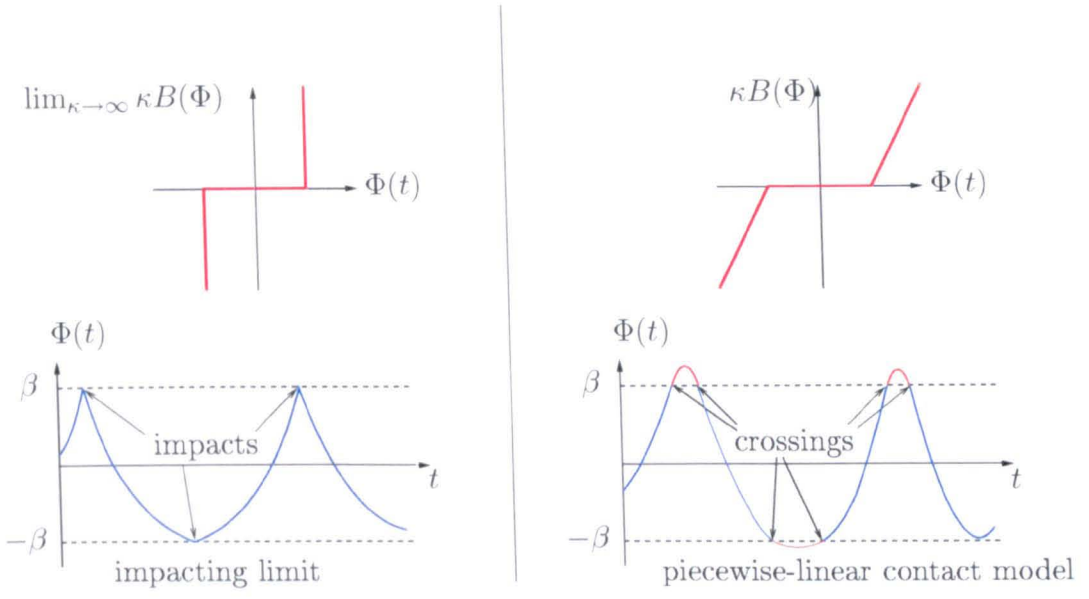

Figure 2.10. The two backlash models with illustrative trajectories. When the gears are in contact in the piecewise-linear model, Hooke's law holds. The impacting-contact model approximates the Hooke's law regime via instantaneous, completely elastic impacts with coefficient of restitution one.

Here $\Phi'(t_{\rm imp}-) = \lim_{t\uparrow t_{\rm imp}} \Phi'(t)$ and $\Phi'(t_{\rm imp}+) = \lim_{t\downarrow t_{\rm imp}} \Phi'(t)$ denote the velocities immediately before and after impact, respectively. The perfect elasticity implies the absence of chattering, see [6, 45, 46] (essentially, an infinite number of impacts in a finite time) which significantly simplifies our analysis and computations. Note that the conservation of angular momentum is not required to describe impacts here because we do not work with $\theta_{\rm X}$ and $\theta_{\rm Y}$ co-ordinates separately, only with their difference.

2.4.1 Classification of periodic orbits

As a starting point, we focus our nonlinear analysis to consider the special case of periodic solutions. More complicated solutions might be reached from these via their bifurcation. For convenience we use the notation introduced in [23, 24] to identify different types of periodic solution. We let $P(m, n^+, n^-)$ denote a periodic solution, of period $m \in \mathbb{Z}$, where $n^\pm$ denote the number of times per period that the orbit contacts the $\Phi = \pm\beta$ boundaries, respectively. In the case of the continuous backlash model (2.24), n^+ (respectively n^-) counts the number of time intervals per period for which $\Phi(t) > \beta$ (respectively $\Phi(t) < -\beta$). In the infinite stiffness $\kappa \to \infty$ limit, n^+ (respectively n^-) counts the number of impacts at which $\Phi(t) = \beta$ (respectively $\Phi(t) = -\beta$). Halse *et al* [23, 24] carried out a detailed analysis of the two simplest families of periodic solutions, for both the impacting limit and piecewise-linear models

UNIVERSITY OF BRISTOL LIBRARY ENGINEERING

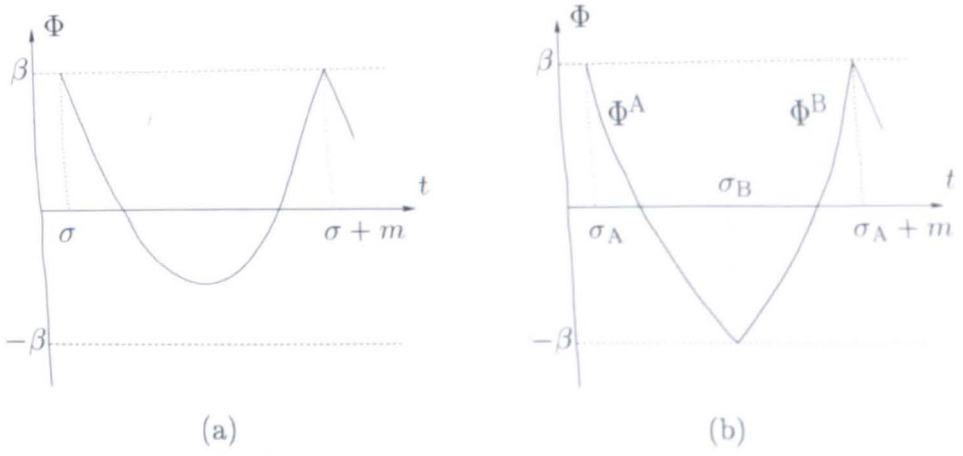

Figure 2.11. Sketches of $P(m,1,0)$ and $P(m,1,1)$ orbits in the impacting-contact model. (a) illustrates the impacts at the $\Phi = +\beta$ boundaries at times σ and $\sigma + m$. (b) illustrates the impacts at the $\Phi = +\beta$ and $\Phi = -\beta$ boundaries at times σ_{A} and σ_{B}. The impact times are not known *a priori* and must be determined during the construction of solutions.

of backlash. The solutions investigated were of types $P(m,1,0)$ and $P(m,1,1)$: that is, orbits that repeat themselves every m cycles of the forcing, with just one impact or crossing of the $\Phi = +\beta$ boundary or one crossing of both the $\Phi = -\beta$ and $\Phi = +\beta$ boundaries, respectively, each period. They showed that, to leading order, existence and stability criteria for these two families of solution are identical for the finite and infinite stiffness models in the limit $\kappa \to \infty$. Thus, for convenience we consider only the impacting model of backlash in the remainder of this chapter, though the problem is still harshly nonlinear due to the impacts. Sketches of the two types of orbit in the impacting limit are illustrated in Figure 2.11.

We now proceed to outline the general procedure for solution construction, where the overall aim is to find bounds for existence of the rattling solutions, and therefore determine how they can be eliminated. Note that the construction techniques which we shall introduce here can be extended to other families of periodic solution with more complex itineraries.

2.4.2 Solution construction technique

The first step in the construction of periodic solutions is to solve the differential equation (2.28) in the freeplay region to determine explicit expressions for Φ and $\Psi := \Phi'$

$$\Phi(t) = 4\pi t + \varepsilon\cos(2\pi t) + c_1 + c_2 e^{-\delta t}, \tag{2.39}$$

$$\Psi(t) := \Phi'(t) = 4\pi - 2\pi\varepsilon\sin(2\pi t) - \delta c_2 e^{-\delta t}, \tag{2.40}$$

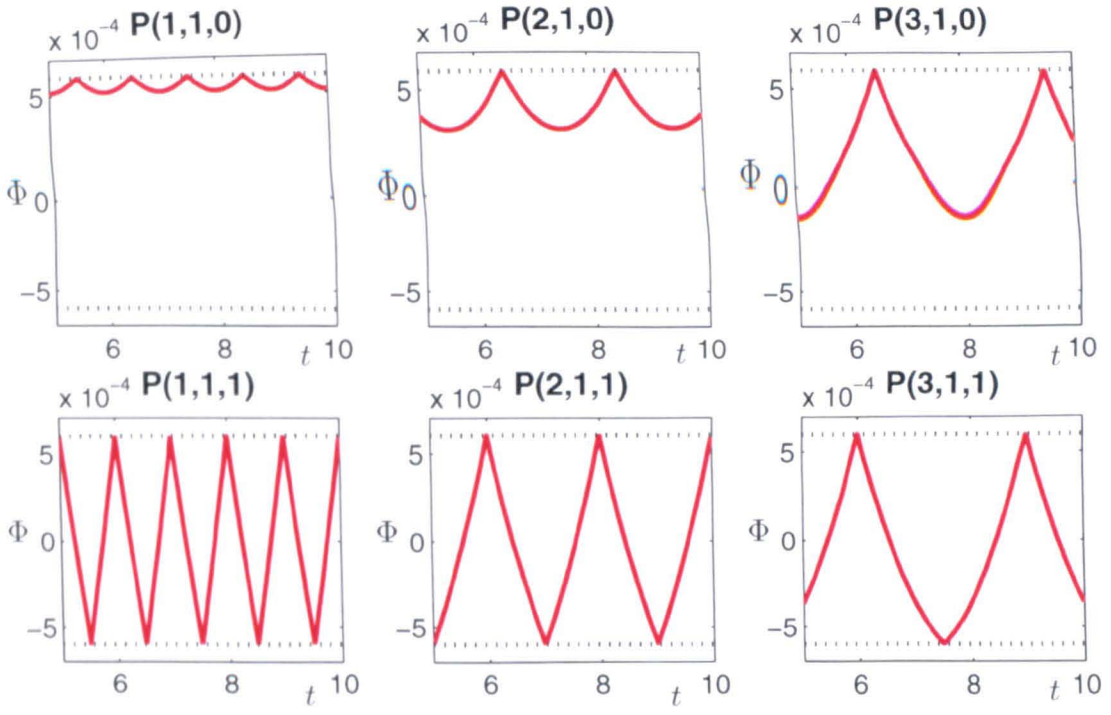

Figure 2.12. Numerical integration of the initial value problem for the piecewise-linear model (2.24), (2.26) illustrating coexisting stable $P(m,1,0)$ and $P(m,1,1)$ orbits for realistic machine parameters and $1 \leq m \leq 3$. The initial conditions for these plots were generated using the solution construction techniques outlined in Section 2.4.1. These solutions all coexist with a quiet solution in which the gears are in permanent linear contact with $\Phi \geq \beta$. Reproduced with permission from *Nonlinear Dynamics of the Automotive Driveline* by C.K. Halse (PhD Thesis 2004) [23].

where c_1 and c_2 are constants of integration. We then patch solution segments together with the impact and periodicity conditions in each case.

The method of construction is similar for both types of solution, although for the $P(m,1,1)$ orbits there is also an impact of the $\Phi = -\beta$ boundary to take into account. In this case we therefore write the solution Φ as the combination of two parts; see Figure 2.11(b), so that

$$\Phi(t) = \begin{cases} \Phi^{\mathrm{A}}(t), & \sigma_{\mathrm{A}} < t < \sigma_{\mathrm{B}}, \\ \Phi^{\mathrm{B}}(t), & \sigma_{\mathrm{B}} < t < \sigma_{\mathrm{A}} + m, \end{cases} \tag{2.41}$$

(and similarly for Ψ). σ_{A} and σ_{B} denote the impact times with the $\Phi = \pm\beta$ boundaries. Here we construct solutions of type $P(m,1,0)$, and then show in Section 2.4.3 how the technique can be extended to solutions of type $P(m,1,1)$. With reference to Figure 2.11(a) our solution loses contact with the $\Phi = +\beta$ boundary at some initial unknown time σ, with velocity $-v$; the periodicity condition then implies that our solution re-impacts the $\Phi = +\beta$ boundary at some time $\sigma + m$ with velocity v. Hence:

$$\Phi(\sigma) = \beta, \qquad \Psi(\sigma) = -v. \tag{2.42}$$

$$\Phi(\sigma + m) = \beta, \qquad \Psi(\sigma + m) = v. \tag{2.43}$$

By applying conditions (2.42)-(2.43) to (2.39) and (2.40) we obtain a system in the form $Ac = b$ to solve for the four unknowns c_1, c_2, v and σ,

$$\begin{pmatrix} 1 & e^{-\delta\sigma} & 0 \\ 1 & e^{-\delta(\sigma+m)} & 0 \\ 0 & -\delta e^{-\delta\sigma} & 1 \\ 0 & -\delta e^{-\delta(\sigma+m)} & -1 \end{pmatrix} \begin{pmatrix} c_1 \\ c_2 \\ v \end{pmatrix} = \begin{pmatrix} \beta - 4\pi\sigma - \varepsilon\cos(2\pi\sigma) \\ \beta - 4\pi(\sigma + m) - \varepsilon\cos(2\pi\sigma) \\ -4\pi + 2\pi\varepsilon\sin(2\pi\sigma) \\ -4\pi + 2\pi\varepsilon\sin(2\pi\sigma) \end{pmatrix}, \tag{2.44}$$

where $c = [c_1, c_2, v]^{\mathrm{T}}$. The important point to note is that this well-determined system is linear in the constants of integration (c_1, c_2, and effectively v) but nonlinear in the impact time σ.

To solve the system of equations (2.44) we find a matrix P such that PA is in echelon form. Consequently, we can then find expressions for c_1, c_2 and v and generate an algebraic constraint on the impact time, σ. P takes the form

$$\begin{pmatrix} \dfrac{e^{-\delta m}}{e^{-\delta m} - 1} & -\dfrac{1}{e^{-\delta m} - 1} & 0 & 0 \\ -\dfrac{e^{\delta\sigma}}{e^{-\delta m} - 1} & \dfrac{e^{\delta\sigma}}{e^{-\delta m} - 1} & 0 & 0 \\ -\dfrac{\delta}{e^{-\delta m} - 1} & \dfrac{\delta}{e^{-\delta m} - 1} & 1 & 0 \\ \delta\coth\left(\dfrac{\delta m}{2}\right) & -\delta\coth\left(\dfrac{\delta m}{2}\right) & 1 & 1 \end{pmatrix}. \tag{2.45}$$

If we premultiply b by P we find that the impact time σ takes the form

$$\sigma = \frac{1}{2\pi}\sin^{-1}\left[\frac{1}{\varepsilon}\left(2 - \delta m\coth\left(\frac{\delta m}{2}\right)\right)\right]. \tag{2.46}$$

There are two admissible solutions to (2.46); we expand them in terms of the small parameter δ to give:

$$\sigma = \begin{cases} \dfrac{-\delta^2 m^2}{12\pi\varepsilon} + O(\delta^4): & \text{in-phase solution,} \\ \dfrac{1}{2} + \dfrac{\delta^2 m^2}{12\pi\varepsilon} + O(\delta^4): & \text{out-of-phase solution.} \end{cases} \tag{2.47}$$

Note as the damping $\delta \to 0$, the argument of the arcsin function in (2.46) tends to zero which implies that $\sigma \to 0$ or $1/2$. This corresponds to a solution which is in phase, and a solution which is $\pi/2$ out of phase with the forcing. Numerical evidence indicates

that the in-phase solution is stable, and the out-of-phase solution is unstable. However a rigorous stability analysis, as detailed in [23, 24], requires a combination of classical Floquet analysis and the method of discontinuity mappings to correct for impacts with the backlash boundaries.

2.4.3 Construction of $P(m,1,1)$ solutions

We now outline the construction procedure for (less desirable) solutions of type $P(m,1,1)$ which impact both $\Phi = \pm\beta$ boundaries. As before, we can patch our solution segments together with the impact and periodicity conditions. With reference to Figure 2.11(b) our solution loses contact with the $\Phi = +\beta$ boundary at some initial unknown time σ_A, with velocity $-v_A$; it then impacts the $\Phi = -\beta$ boundary at some unknown time σ_B, with velocity $-v_B$. Hence:

$$\Phi_A(\sigma_A) = \beta, \qquad \Psi_A(\sigma_A) = -v_A, \tag{2.48}$$

$$\Phi_A(\sigma_B) = -\beta, \qquad \Psi_A(\sigma_B) = -v_B. \tag{2.49}$$

The impact and periodicity conditions then imply

$$\Phi_B(\sigma_B) = -\beta, \qquad \Psi_B(\sigma_B) = v_B, \tag{2.50}$$

$$\Phi_B(\sigma_A + m) = \beta, \qquad \Psi_B(\sigma_A + m) = v_A. \tag{2.51}$$

By applying conditions (2.48)-(2.51) to equations (2.39) and (2.40) we obtain a system in the form $\boldsymbol{A}\boldsymbol{c} = \boldsymbol{b}$ to solve for the eight unknowns c_1^A, c_2^A, c_1^B, c_2^B, v_A, v_B, σ_A and σ_B, where

$$A = \begin{pmatrix} 1 & e^{-\delta\sigma_A} & 0 & 0 & 0 & 0 \\ 1 & e^{-\delta\sigma_B} & 0 & 0 & 0 & 0 \\ 0 & 0 & 1 & e^{-\delta\sigma_B} & 0 & 0 \\ 0 & 0 & 1 & e^{-\delta(\sigma_A+m)} & 0 & 0 \\ 0 & -\delta e^{-\delta\sigma_A} & 0 & 0 & 1 & 0 \\ 0 & 0 & 0 & -\delta e^{-\delta(\sigma_A+m)} & -1 & 0 \\ 0 & -\delta e^{-\delta\sigma_B} & 0 & 0 & 0 & 1 \\ 0 & 0 & 0 & -\delta e^{-\delta\sigma_B} & 0 & -1 \end{pmatrix}, \tag{2.52}$$

$$b = \begin{pmatrix} -4\pi\sigma_A - \varepsilon\cos 2\pi\sigma_A + \beta \\ -4\pi\sigma_B - \varepsilon\cos 2\pi\sigma_B - \beta \\ -4\pi\sigma_B - \varepsilon\cos 2\pi\sigma_B - \beta \\ -4\pi(\sigma_A + m) - \varepsilon\cos 2\pi\sigma_A + \beta \\ 2\pi\varepsilon\sin 2\pi\sigma_A - 4\pi \\ 2\pi\varepsilon\sin 2\pi\sigma_A - 4\pi \\ 2\pi\varepsilon\sin 2\pi\sigma_B - 4\pi \\ 2\pi\varepsilon\sin 2\pi\sigma_B - 4\pi \end{pmatrix}, \tag{2.53}$$

and $\mathbf{c} = [c_1^A, c_2^A, c_1^B, c_2^B, v_A, v_B]^T$. In contrast to system (2.44) for the $P(m,1,0)$ orbits, the expressions for the impact times, σ_A and σ_B are not solvable in closed form. However progress may be made either with asymptotics [23, 24] or with a numerical root-finding procedure.

2.4.4 Consistency checks and bounds for existence

Once we have solved for impact times and solution coefficients, we must make a consistency check to ensure that the itinerary matches our construction, that is, that there are no additional crossings of the discontinuity boundaries $\Phi = \pm\beta$. Since more progress can be made with explicit calculations, we show how this procedure works for $P(m,1,0)$ solutions. We require:

(i) No crossings of the $\Phi = -\beta$ boundary, which would contradict the assumptions used in the solution construction. We must check that the minimum displacement of Φ is greater than $-\beta$.

We also require

(ii) validity of σ, i.e., the argument of the arcsin function (2.46) lies between ± 1.

The latter requirement gives a condition on eccentricity,

$$\varepsilon > \varepsilon_{\text{crit}} := \frac{\delta^2 m^2}{6} + O(\delta^4), \tag{2.54}$$

for the existence of simple $P(m,1,0)$ solutions. We must then check requirement (i). To do this we must find the minimum displacement; we thus require $\hat{t}$ such that $\Phi'(\hat{t}) = \Psi(\hat{t}) = 0$; we try a power series solution in the form

$$\hat{t} = \sigma + \frac{m}{2} + \hat{t}_0 + \hat{t}_1\delta + O(\delta^2). \tag{2.55}$$

We have four cases corresponding to in-phase/out-of-phase solutions and m odd/even. In each case we solve for the coefficients $\hat{t}_i$, substitute these expressions for $\hat{t}$ into the condition $\Phi(\hat{t}) > -\beta$ and expand as a series to give bounds on the existence of this type of solution. Figure 2.13 displays the results in the δ–ε plane for m odd, where the various boundaries may be identified as bifurcations [23, 24].

We observe that as the periodicity m is increased, or the damping δ reduced, the number of coexisting solutions increases. In region (b) both the in-phase and out-of-phase $P(m,1,0)$ solutions exist, in region (c) only out-of-phase $P(m,1,0)$ solutions can exist. Neither solution exists in region (d). If we follow the dashed line we can follow the sequence of bifurcations: a saddle-node where the in-phase and out-of-phase solutions are born, a grazing where the in-phase solution is destroyed, and finally a grazing where the out-of-phase solution is destroyed.

It is possible to construct a similar bifurcation diagram for the $P(1,1,1)$ solutions, although it is necessary to resort to numerical root-finding procedures. For these types of solution, numerical evidence indicates that the stability is opposite to that of the $P(m,1,0)$ solutions. We find that the out-of-phase solution is typically stable, and the in-phase solution is unstable. In Figure 2.14 we plot a schematic diagram of these numerical existence bounds in the δ–ε plane. We find a similar sequence of events: the grazing curves are the same (because they correspond to bifurcations at which $P(m,1,0)$ solutions interact), but in contrast the curve of saddle-node bifurcations is very slightly raised, and there is an additional bifurcation curve which represents the out-of-phase solution losing stability in a period-doubling bifurcation. Similarly, no in-phase or out-of-phase solution of type $P(1,1,1)$ can exist in region (d).

Note that the curve of saddle-node bifurcations (in blue), for both types of solution, is virtually indistinguishable from the x-axis. In the case of $P(m,1,0)$ solutions this bound corresponds to (2.54). This bound will always be satisfied for real machine parameters since in practice ε and δ are of similar magnitude, and hence (according to this theory) it is almost impossible to eliminate rattling solutions by reducing eccentricity.

2.5 Discussion

In this chapter we have introduced two nonsmooth differential equation models for the dynamics of the pump, motivated by real machine parameters. We calculated a bound on the eccentricity, above which non-rattling solutions cannot exist. This bound is found to be of the same order of magnitude as typical measured eccentricities. In practice our calculated bound will be slightly pessimistic, due to limitations in our model, for example the neglection of lubrication between the gear teeth. We have also

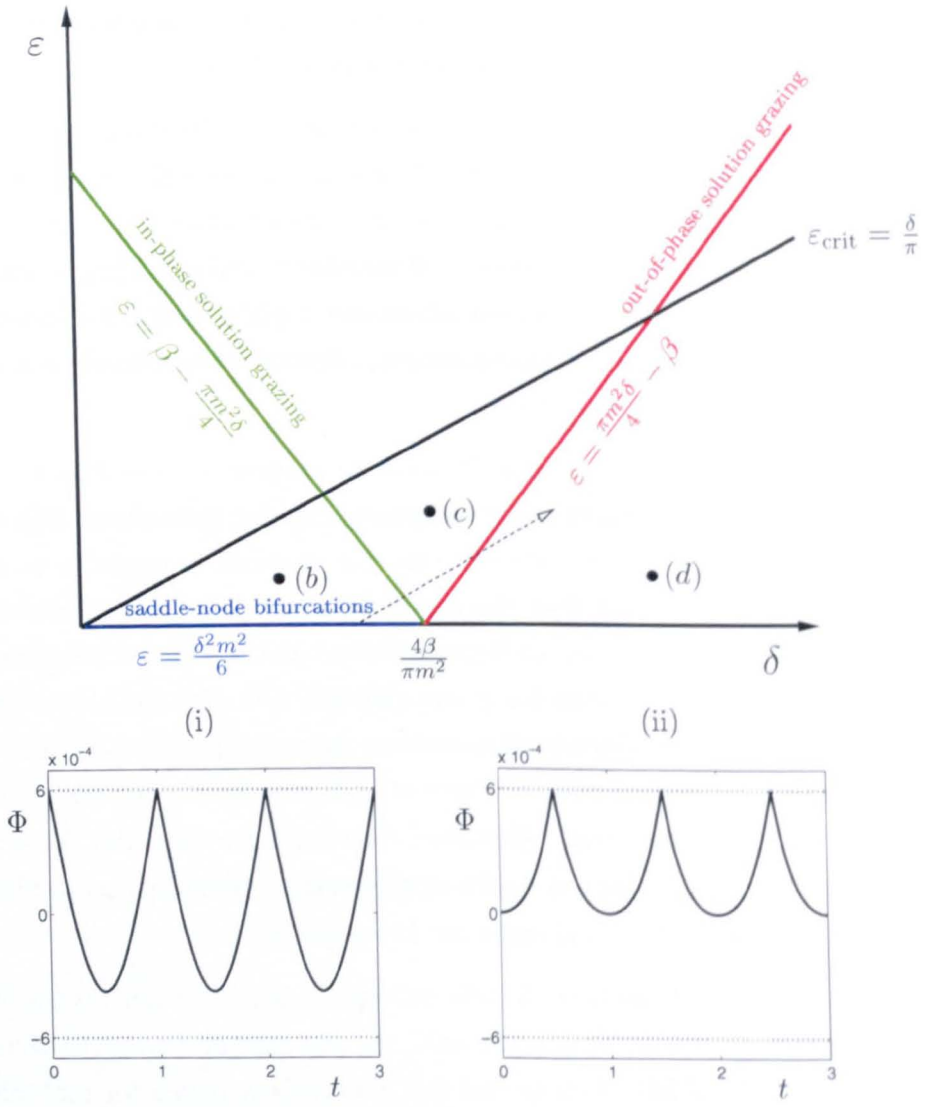

Figure 2.13. Sketch of the existence bounds for the $P(m,1,0)$ solutions (in the case $m=1$). The in-phase and out-of-phase solution grazings with $\Phi = -\beta$ are shown in green and red, respectively. Note that the curve of saddle-node bifurcations, illustrated in blue, corresponding to the bound (2.54), is virtually indistinguishable from the x-axis. The critical eccentricity bound, (2.37) is also shown in black. (i) and (ii) are numerical integrations of (2.28), (2.38) and illustrate coexisting in-phase (stable) and out-of-phase (unstable) $P(1,1,0)$ solutions, respectively. In region (b) solutions of types (i) and (ii) exist, in region (c) we have only solutions of type (ii). Neither solution exists in region (d). If we follow the dashed line we have a sequence of bifurcations: a saddle-node where the in-phase and out-of-phase solutions are born, a grazing where the in-phase solution is destroyed, and finally a grazing where the out-of-phase solution is destroyed.

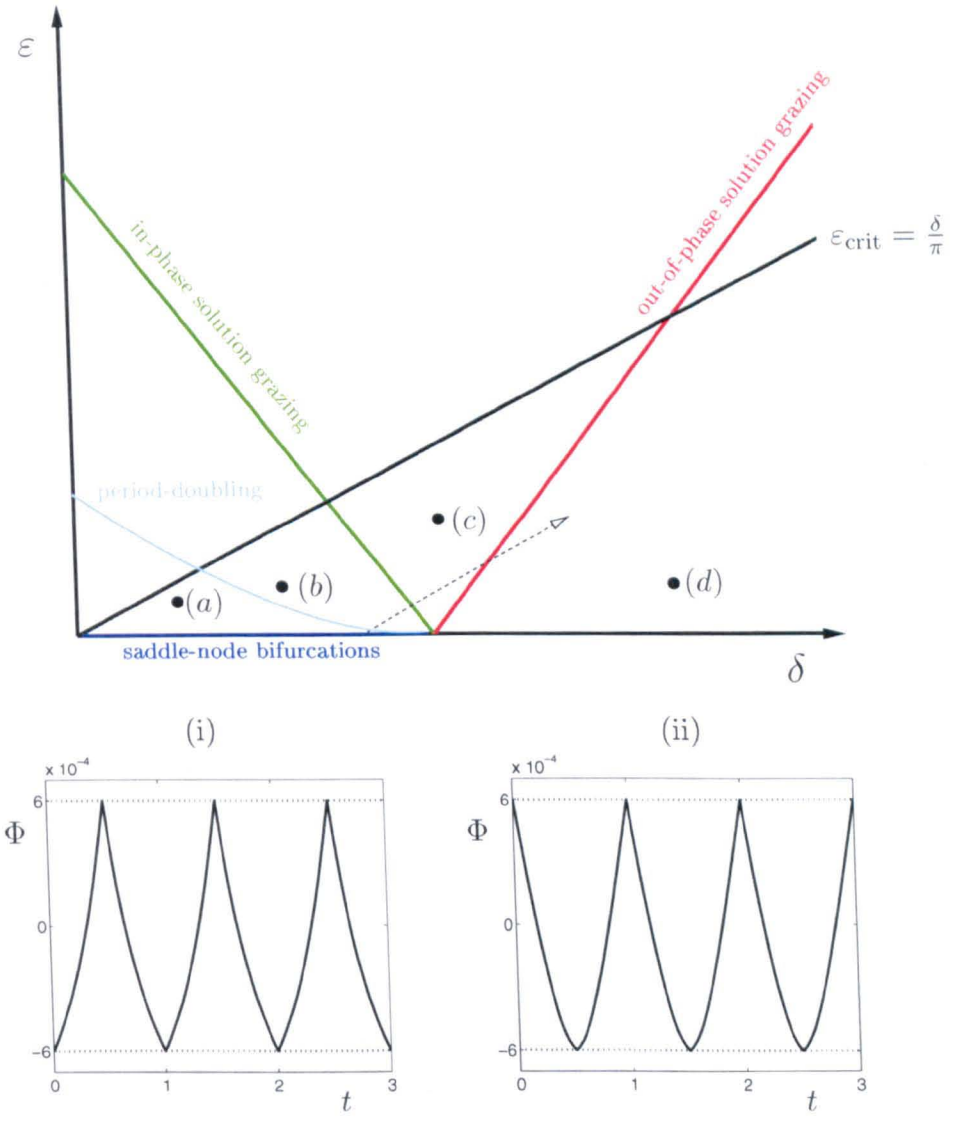

Figure 2.14. Sketch of the existence bounds for the $P(1,1,1)$ solutions. The in-phase and out-of-phase solution grazings with $\Phi = -\beta$ are shown in green and red, respectively. Note that the curve of saddle-node bifurcations, illustrated in blue, is also virtually indistinguishable from the x-axis. Period-doubling of the out-of-phase solution is illustrated in cyan, and the critical eccentricity bound, (2.37) is shown in black. (i) and (ii) are numerical integrations of (2.28), (2.38) and illustrate coexisting out-of-phase and in-phase $P(1,1,1)$ solutions, respectively. In region (a) solutions of type (i) (out-of-phase, stable) and (ii) (in-phase, unstable) exist. In (b) these two solutions still exist, although the out-of-phase solutions are now unstable. In region (c) we have only solutions of type (i). Neither solution exists in region (d). If we follow the dashed line we have a sequence of bifurcations: a saddle-node where the in-phase and out-of-phase solutions are born, a period-doubling where the out-of-phase solution loses stability, a grazing where the in-phase solution is destroyed, and finally a grazing where the out-of-phase solution is destroyed.

observed that increasing the operating speeds or sizes of the pumps (for example using either a booster of type B or C instead of our standard pump) decreases the critical eccentricity (i.e., increases the propensity to rattle).

Preliminary numerical investigations indicate a rich structure of coexistence. We have used a combination of explicit construction, asymptotic methods and numerical techniques to investigate two types of nonlinear solution families. In particular, we derived (asymptotic) analytical bounds for the existence of various classes of periodic solution as a function of machine parameters.

We have found that it is impractical to eliminate rattling $P(m,1,0)$ solutions by reducing eccentricity. Furthermore, we have established that reducing the coefficient of restitution offers no significant benefits. If we repeat the construction of $P(m,1,0)$ solutions with impacts of coefficient of restitution ρ, $0 < \rho < 1$, we find

$$\sigma = \frac{1}{2\pi}\sin^{-1}\left[\frac{1}{\varepsilon}\left(2 - \frac{2\delta m}{(1+\rho)}\frac{(\rho + e^{-\delta m})}{(1-e^{-\delta m})}\right)\right]. \tag{2.56}$$

In the same way as before, the $P(m,1,0)$ solutions do not exist if the argument of the arcsin function in (2.56) exceeds one in modulus. Therefore to leading order we require

$$\varepsilon > \delta m\left(\frac{1}{6}\delta m - \frac{(1-\rho)}{(1+\rho)}\right). \tag{2.57}$$

Note that for $\rho = 1$ we recover (2.54) as expected, nevertheless we observe that the $\varepsilon \sim O(\delta^2)$ scaling is independent of the coefficient of restitution ρ.

At this stage it is not obvious how to solve the noise and vibration problem at the nonlinear level: the bound on ε for the destruction of simple $P(m,1,0)$ solutions is impossible to achieve in practice. This motivates exploring machine design changes - an idea which we shall return to in Chapters 4 and 5.

There are two possible ways forward:

- Explore improvements in the machine design - see Chapters 4 and 5.
- Explore the basins of attraction of rattling solutions for the basic machine. It may well be the case that most initial data select the permanent linear contact solution, even if stable rattling behaviours coexist. See Chapter 3.

Chapter 3

Basins of Attraction Computations

In Chapter 2 we established that families of periodic solution that rattle can coexist with quiet operation, even if the eccentricity bound (2.36) is satisfied. See Figures 2.8 and 2.12 for some illustrative examples. Moreover, some of these rattling solutions are linearly stable and consequently Roots booster pumps have the potential for intermittency. As we have seen, it is not possible to destroy all rattling solutions for practical machine parameters.

It is therefore a matter of practical concern to establish which linearly stable solutions dominate the $t \to \infty$ dynamics. Consequently, this chapter is concerned with the computation of basins of attraction using cell-to-cell mapping techniques [27, 28]. Recall that for a Roots booster pump the rescaled damping δ, half backlash β and eccentricity ε are all small ($\sim 10^{-4}$), and the rescaled stiffness parameter κ is large ($\sim 10^{3}$). These parameters present a computational challenge for two independent reasons. Firstly, the large stiffness value introduces a small time-scale which must be resolved. Secondly, the small damping value gives rise to long transients and slender features in basin diagrams. This latter problem is severe for the parameter values quoted here, and consequently in this chapter we work with scaled-up values for the purposes of illustration. However, we expect the qualitative details of the structures and transitions we observe to persist at more realistic parameter values.

In Section 2.4 we introduced an impacting-contact model of backlash, which is considerably simpler to analyse than the piecewise-linear model, (2.24), (2.26). However, it has the disadvantage that it does not admit quiet solutions for which $\Phi \geq +\beta$ for all time. Consequently a proper understanding of the relative dominance of quiet and rattling behaviour can only be achieved by analysing equations (2.28), (2.38) in comparison with equations (2.24), (2.26). Other authors [13–15] have computed basins of attraction for an impacting-contact gear model and established the existence of chaotic regimes. But we go further and use equations (2.24), (2.26) to calculate the basins of attraction for quiet solutions – a matter of some importance from the engineering point of view.

Furthermore, we also describe more computationally-efficient methods by which the basins of attraction may be produced. In particular, we calculate stable manifolds, which form the basin boundaries, using Man1D, a module of DsTool [5, 19, 31]. To our knowledge this is the first time that this package has been used to analyse a one degree-of-freedom backlash oscillator system such as the one described here.

The outline of the chapter is as follows. We begin by describing in detail the reduction of the impacting-contact equations (2.28), (2.38) and full piecewise-linear equations (2.24), (2.26) models to Poincaré maps, applied at the section $\Phi = +\beta$. See Sections 3.1 and 3.2. These impact maps considerably simplify the analysis, visualisation and computations that follow. In particular, they enable the direct application of the *cell-to-cell mapping* technique, which we introduce in Section 3.3. Section 3.3 also describes our refinements to the cell-to-cell mapping technique, that we employ to minimise the effect of long transients. Basins of attraction for several ranges of parameter values (which all satisfy equation (2.36)) are computed in Section 3.4. We observe complicated dynamics and we present an explanation of some of the transitions in the system's behaviour in terms of smooth and discontinuity-induced bifurcations (see [17]). In addition, in Section 3.5 we discuss the important role that the discontinuity in our system plays in the intricate stretching and folding of the phase space.

The material in this chapter is based on the paper *Basins of attraction in nonsmooth models of gear rattle*, (2008) which has been accepted for publication in the International Journal of Bifurcation and Chaos (co-authors P.T. Piiroinen, R.E. Wilson and M.E. Homer) [39].

3.1 Reduction to map: impacting limit

The model equations (2.24), (2.26) and (2.28), (2.38) are non-autonomous single degree-of-freedom nonlinear oscillators with phase space (t, Φ, Φ'). In this chapter we analyse their dynamics via their reduction to Poincaré maps. In such periodically forced systems, the usual approach is to reduce to a two-dimensional stroboscopic map which generates a sequence (Φ_0, Φ_0'), (Φ_1, Φ_1'), (Φ_2, Φ_2'), ..., at $t = 0, 1, 2, \ldots$. However, for our system it is more natural to use one of the impact conditions as the Poincaré section. This is because the impacting system (2.28), (2.38) is linear between impacts, and consequently we may exploit its explicit solution

$$\Phi(t) = c_1 + c_2 e^{-\delta t} + \varepsilon \cos 2\pi t + 4\pi t, \tag{3.1}$$

since this proves to be more efficient than solving the ordinary differential equation equation (2.28) by time integration. Note that a solution of equations (2.28), (2.38)

consists of a sequence of segments described by (3.1) with the constants c_1 and c_2 repeatedly reset at impacts when $\Phi = \pm\beta$. Although (3.1) gives Φ explicitly in time, the task of finding times at which impact conditions $\Phi = \pm\beta$ apply reduces to the numerical solution of transcendental equations.

We now consider the itinerary of impacts. When $\Phi' = 0$, (2.28) yields

$$\Phi''(t) = 4\pi\delta - 2\pi\varepsilon(4\pi^2 + \delta^2)^{\frac{1}{2}} \cos(2\pi t + \xi), \tag{3.2}$$

where ξ is a phase shift. This expression is always positive provided

$$\varepsilon < \varepsilon_{\text{crit}}^{(2)} := \frac{2\delta}{(4\pi^2 + \delta^2)^{\frac{1}{2}}} \qquad (\sim \frac{\delta}{\pi} \quad \text{as} \quad \delta \to 0). \tag{3.3}$$

For sufficiently large κ, we have $\varepsilon_{\text{crit}} < \varepsilon_{\text{crit}}^{(2)}$, hence enforcing equation (2.36) guarantees the positivity of Φ'' at smooth local extrema. Hence local maxima of Φ are only possible at $\Phi = +\beta$ where Φ' is discontinuous, but local minima may be achieved smoothly for $|\Phi| < \beta$ or discontinuously at $\Phi = -\beta$, or (rarely) when $\Phi = -\beta$ and $\Phi' = 0$ simultaneously.

Let us now consider the fate of trajectories with initial data $-\beta < \Phi \leq +\beta$ and $\Phi' < 0$. Such a trajectory must impact at some subsequent time with either $\Phi = +\beta$ or $\Phi = -\beta$. To see this, assume the contrary, in which case (3.1) applies for all time, yielding $\Phi \to +\infty > +\beta$ as $t \to \infty$ and hence a contradiction. In the case where the next impact is with $\Phi = -\beta$, the velocity will reverse to a non-negative value. The subsequent impact after this one must be with $\Phi = +\beta$, since if the next impact were with $\Phi = -\beta$, a (smooth) local maximum would be required. Hence solutions must repeatedly return to the $\Phi = +\beta$ impact boundary, although they need not ever visit the $\Phi = -\beta$ boundary.

Thus $\Phi = +\beta$ defines a natural Poincaré section, and we work with a two-dimensional impact map P on $(t, v) \in [0, 1) \times (0, \infty)$ which describes times and velocities of impacts. Here time t is taken modulo one due to the period-one forcing. By convention, we take $v = \Phi'(t-) = -\Phi'(t+) > 0$ for the velocity co-ordinate at impact at time t. Later, when the piecewise-linear model (2.24), (2.26) is used, trajectories cross the surface $\Phi = +\beta$ and this idea needs refinement.

We now turn our attention to the structure of the impact map under consideration. To summarise our discussion above, for parameters which satisfy equation (2.36), there are two main outcomes (see Figure 3.2) for a given initial condition with $\Phi = +\beta$ and $\Phi' = -v_0 < 0$ at time t_0:

Case (a) The next impact is with $\Phi = +\beta$, see Figure 3.2(a).

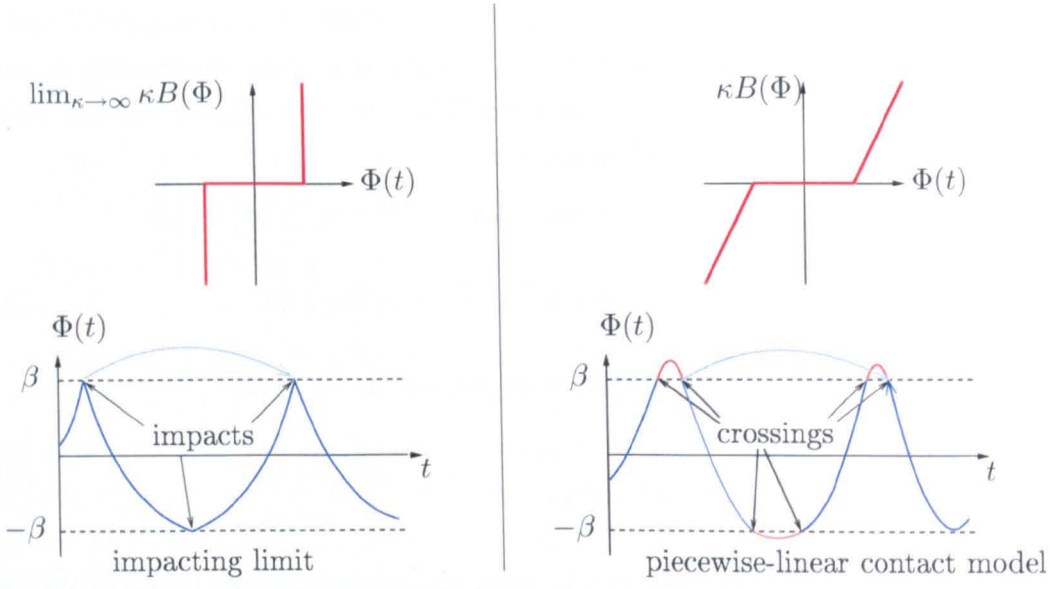

Figure 3.1. The two backlash models with illustrative trajectories. The cyan arrows label the impact (first return) map which maps the time and velocity from departure at $\Phi = \beta$ to the next crossing or impact leaving $\Phi = \beta$.

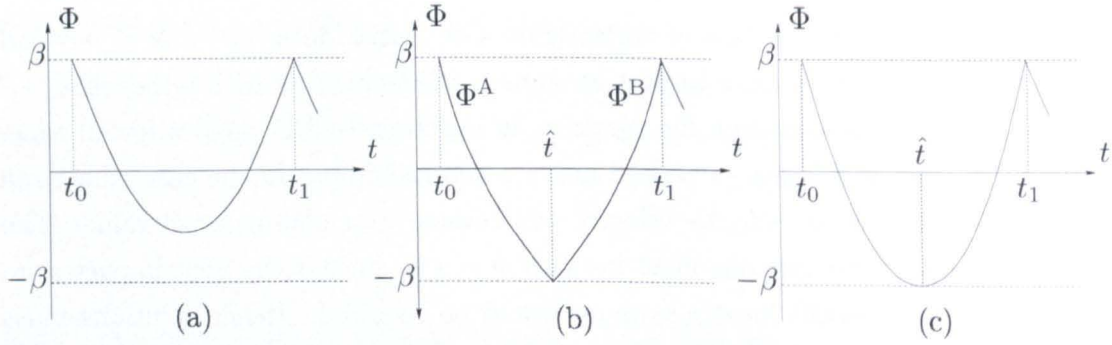

Figure 3.2. Sketches of the three different types of trajectory. From left to right : (a) illustrates a trajectory whose next impact is with the $\Phi = +\beta$ boundary, (b) a trajectory whose next impact is with the $\Phi = -\beta$ boundary before it re-impacts the $\Phi = +\beta$ boundary and (c) a grazing trajectory that grazes the $\Phi = -\beta$ boundary.

Case (b) The next impact is with $\Phi = -\beta$ and the next but one impact is with $\Phi = +\beta$, see Figure 3.2(b).

Furthermore, we have:

Case (c) The trajectory grazes the $\Phi = -\beta$ boundary with zero velocity before re-impacting the $\Phi = +\beta$ boundary, see Figure 3.2(c).

In fact, case (c) separates cases (a) and (b) in the sense that if data (t_0, v_0^*) give rise to case (c), then (t_0, v_0) is case (a) if $v_0 < v_0^*$ or is case (b) if $v_0 > v_0^*$. This may be proven

by a monotonicity argument which establishes that if Φ_1 and Φ_2 are solutions of (3.1) with initial data $\Phi_1(t_0) = \Phi_2(t_0) = \beta$ and $\Phi_1'(t_0) = -v_1$ and $\Phi_2'(t_0) = -v_2$ with $v_2 > v_1$, then $\Phi_1(t) > \Phi_2(t)$ for all $t > t_0$. The monotonicity principle itself may be established by noting that $\Phi_{\text{diff}}(t) := \Phi_1(t) - \Phi_2(t)$ satisfies $\Phi_{\text{diff}}'' + \delta\Phi_{\text{diff}}' = 0$ from (2.28), together with $\Phi_{\text{diff}}(t_0) = 0$, and so $\Phi_{\text{diff}}(t) = A[1 - e^{(-\delta(t-t_0))}]$.

For a given t_0, it follows that there is a unique $v_0^*(t_0)$ which satisfies case (c). Three example trajectories leaving the $\Phi = +\beta$ boundary at the same time with different initial velocities are illustrated in Figure 3.3(a).

The remainder of this section describes how we construct the impact map on (t, v) pairs and how we tackle the resulting transcendental equations robustly. Section 3.1.1 sets up and solves systems of equations which define the grazing curve $v^*(t)$ described by case (c). Once this curve is computed, any given data (t, v) may be classified as case (a) (described in Section 3.1.2) or case (b) (described in Section 3.1.3). Note that the construction for case (b) poses particular difficulties since it consists of two trajectory segments, hence two impact times and two distinct root-finding procedures.

3.1.1 Solution for the grazing curve

We begin by constructing trajectories that impact the $\Phi = -\beta$ boundary with zero velocity, see Figure 3.2(c). Solutions of this type start at the $\Phi = +\beta$ boundary at time t_0 with velocity $\Phi'(t_0+) = -v_0^*(t_0)$ (to be determined) and graze the $\Phi = -\beta$ boundary at time $\hat{t}$ with zero velocity. Hence from equation (3.1) we have

$$(\Phi(t_0) =) \quad c_1 + c_2 e^{-\delta t_0} + \varepsilon \cos 2\pi t_0 + 4\pi t_0 = \beta, \tag{3.4}$$

$$(\Phi'(t_0) =) \quad -\delta c_2 e^{-\delta t_0} - 2\pi\varepsilon \sin 2\pi t_0 + 4\pi = -v_0^*, \tag{3.5}$$

$$(\Phi(\hat{t}) =) \quad c_1 + c_2 e^{-\delta \hat{t}} + \varepsilon \cos 2\pi \hat{t} + 4\pi \hat{t} = -\beta, \tag{3.6}$$

$$(\Phi'(\hat{t}) =) \quad -\delta c_2 e^{-\delta \hat{t}} - 2\pi\varepsilon \sin 2\pi \hat{t} + 4\pi = 0, \tag{3.7}$$

as a system of four equations in the unknowns c_1, c_2, $\hat{t}$ and v_0^*. However, it is ultimately only v_0^* that is of interest.

If we subtract (3.6) from (3.4) and use (3.7) to substitute for c_2 we obtain a single equation

$$\frac{1}{\delta}(4\pi - 2\pi\varepsilon \sin 2\pi\hat{t})(e^{\delta(\hat{t}-t_0)} - 1) + \varepsilon(\cos 2\pi t_0 - \cos 2\pi\hat{t}) + 4\pi(t_0 - \hat{t}) - 2\beta = 0, \tag{3.8}$$

to solve numerically for $\hat{t}$ as a function of t_0. The only remaining question concerns the counting of solutions and whether the solver finds the correct root. In this case provable

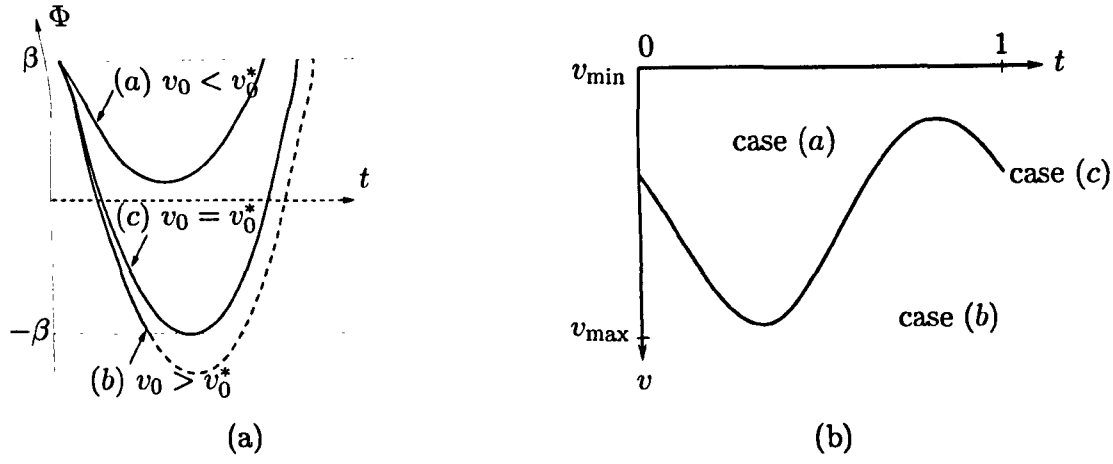

Figure 3.3. (a) Example trajectories of type (a), (b) and (c) (described in Sections 3.1.2, 3.1.3 and 3.1.1, respectively) leaving $\Phi = +\beta$ at the same time, but with different velocities. Solid lines represent true trajectories, and the dashed line represents a trajectory ignoring the impact with $\Phi = -\beta$. (b) The division of the (t, v) space into regions characterised by trajectories of type (a), (b) and by the grazing curve (c).

robustness is not critical because the grazing curve $v^*(t)$ is computed in full prior to the basin computation, and a failure to find the correct root $\hat{t}$ for individual values of t_0 can be identified by visual inspection. However, in our examples no such problems occurred.

In fact, for each initial time t_0, it turns out that two values $\hat{t}$ satisfy (3.8), but only one of these satisfies $\hat{t} > t_0$. In the first instance we therefore solve (3.8) via the Newton method (see for example [9]) with an initial guess $t_0 + 1/2$, and we have found that this converges to the correct root in all the cases that we have tried. Once $\hat{t}$ has been calculated for a single value of t_0, we compute further t_0^k, $\hat{t}^k$ pairs using a 'continuation' type method where t_0^k is stepped in small increments and the solution $\hat{t}^k$ at one t_0^k-value is used as the Newton solver's initial guess for the next t_0^k-value. Each $\hat{t}^k$-value can then be converted to a corresponding velocity v_0^* using (3.5), and an interpolating curve $(t, v^*(t))$ is thus constructed. As we have discussed, this *grazing curve* acts as the separatrix of the trajectories whose next impact is with either the $\Phi = +\beta$ or $\Phi = -\beta$ boundary, see Figure 3.3(b).

3.1.2 Case (a) : next impact with $\Phi = +\beta$

We now analyse trajectory segments of the form shown in Figure 3.2(a), and thus we develop the impact map $P(t_0, v_0) = (t_1, v_1)$ with $v_0 < v_0^*(t_0)$. We have

$$(\Phi(t_0) =) \quad c_1 + c_2 e^{-\delta t_0} + \varepsilon \cos 2\pi t_0 + 4\pi t_0 = \beta, \tag{3.9}$$

$$(\Phi'(t_0+) =) \quad -\delta c_2 e^{-\delta t_0} - 2\pi\varepsilon \sin 2\pi t_0 + 4\pi = -v_0, \tag{3.10}$$

$$(\Phi(t_1) =) \quad c_1 + c_2 e^{-\delta t_1} + \varepsilon \cos 2\pi t_1 + 4\pi t_1 = \beta, \tag{3.11}$$

$$(\Phi'(t_1-) =) \quad -\delta c_2 e^{-\delta t_1} - 2\pi\varepsilon \sin 2\pi t_1 + 4\pi = v_1, \tag{3.12}$$

cf. equations (3.4)–(3.7). If we subtract (3.9) from (3.11), we can define $f(t_1) = \Phi(t_1) - \Phi(t_0)$ and then solve $f(t_1) = 0$ for t_1 in terms of fixed t_0. This may then be expanded using (3.10) to substitute for c_2, to give

$$f(t_1) = \frac{1}{\delta}(4\pi + v_0 - 2\pi\varepsilon \sin 2\pi t_0)\,(e^{-\delta(t_1-t_0)} - 1) + \varepsilon(\cos 2\pi t_1 - \cos 2\pi t_0) + 4\pi(t_1 - t_0) = 0. \tag{3.13}$$

By using the relationship with Φ, we have $f(t_0) = 0$ and $f'(t_0) < 0$; moreover we have $\lim_{t\to\infty} f(t) = +\infty$. It follows that there is a unique root $t_1 > t_0$ which may be bracketed by successive doubling of the initial guess for t_1. Then either interval bisection or the method of false position will find the root robustly.

However, for δ small, a convexity argument may be used to establish the robust convergence of the Newton method. Note that $f(t)$ is not globally convex, even though it has a unique local minimum. To see this, we use (3.1) to derive

$$\Phi''(t) = \delta^2 c_2 e^{-\delta t} - 4\pi^2 \varepsilon \cos 2\pi t, \tag{3.14}$$

which displays oscillatory behaviour as $t \to \infty$. However, since

$$c_2 = \frac{4\pi + v_0 - 2\pi\varepsilon \sin 2\pi t_0}{\delta} e^{\delta t_0}, \tag{3.15}$$

a sufficient condition for convexity is given by

$$t < t_{\max} := t_0 + \frac{1}{\delta} \log_e \left[\frac{\delta(4\pi + v_0 - 2\pi\varepsilon \sin 2\pi t_0)}{4\pi^2 \varepsilon} \right]. \tag{3.16}$$

Then $t_{\max} > t_0$ is established by showing that the argument of the logarithm exceeds one, for which it suffices that

$$\varepsilon < \varepsilon_{\text{crit}}^{(3)} := \frac{\delta}{\pi + \delta/2} \sim \frac{\delta}{\pi}, \tag{3.17}$$

cf. (3.3), which thus generally holds throughout this chapter. The interest however is in the limit $\delta \to 0$ with (3.17) maintained, for which $t_{\max} \to \infty$. In this case, successive doubling may be used to establish an interval which verifiably brackets the desired root t_1 and on which Φ and hence f are convex. The Newton method thus displays robust one-sided second order convergence for any initial guess in this interval which is to the right of the root.

3.1.3 Case (b) : next impact with $\Phi = -\beta$

We now proceed to construct trajectories that impact the $\Phi = -\beta$ boundary before re-impacting the $\Phi = +\beta$ boundary. Trajectories of this type consist of two pieces (see Figure 3.2(b)), so two root finding procedures are required, to find the times of impact with the $\Phi = -\beta$ and $\Phi = +\beta$ boundaries, respectively.

The first section of trajectory (Φ^{A}) starts from the $\Phi = +\beta$ boundary with initial times and velocities (t_0, v_0) and then impacts the $\Phi = -\beta$ boundary with unknown times and velocities $(\hat{t}, \hat{v})$. In addition to equations (3.4) (replacing v_0^* by v_0), (3.5) and (3.6) we have

$$\Phi'(\hat{t}) = -\delta c_2 e^{-\delta \hat{t}} - 2\pi\varepsilon \sin 2\pi\hat{t} + 4\pi = \hat{v}. \tag{3.18}$$

If we subtract (3.4) from (3.6) and use (3.5) to substitute for c_2, we have

$$\frac{1}{\delta}\left(4\pi + v_0 - 2\pi\varepsilon \sin 2\pi t_0\right)\left(e^{-\delta(\hat{t}-t_0)} - 1\right) + \varepsilon(\cos 2\pi\hat{t} - \cos 2\pi t_0) + 4\pi(\hat{t} - t_0) + 2\beta = 0. \tag{3.19}$$

However (see Figure 3.3(a)) this equation has two roots via its relationship to Φ and we seek only the smallest one for which a convexity argument applied to Φ may be used to establish the robust performance of the Newton method. To see this, note

$$\Phi'(t_{\max}) = 4\pi\left(1 - \frac{\pi\varepsilon}{\delta}\right) - 2\pi\varepsilon \sin 2\pi t_{\max}, \tag{3.20}$$

which is positive for ε sufficiently small, positive, and less than δ/π. Here $t_{\max}$ is given by (3.16). It follows that the local minimum of Φ is less than $t_{\max}$, and since $\hat{t}$ is less than the local minimum, Φ and hence f are convex on the interval $[t_0, \hat{t}]$. Hence for an underestimate of $\hat{t}$ such as $t_0 + 2\beta/v_0$, the Newton method will give robust one-sided convergence to $\hat{t}$. The corresponding impact velocity can then be found from equation (3.18) which is then reversed for the initial data of the second part of the trajectory.

The second piece of trajectory (Φ^{B}) leaves the $\Phi = -\beta$ boundary with known times and velocities $(\hat{t}, -\hat{v})$ and impacts the $\Phi = +\beta$ boundary with unknown times and

velocities $(t_1, -v_1)$. From equation (3.1) we have

$$\Phi(\hat{t}) = \hat{c_1} + \hat{c_2}e^{-\delta\hat{t}} + \varepsilon\cos 2\pi\hat{t} + 4\pi\hat{t} = -\beta, \tag{3.21}$$

$$\Phi'(\hat{t}) = -\delta\hat{c_2}e^{-\delta\hat{t}} - 2\pi\varepsilon\sin 2\pi\hat{t} + 4\pi = -\hat{v}, \tag{3.22}$$

$$\Phi(t_1) = \hat{c_1} + \hat{c_2}e^{-\delta t_1} + \varepsilon\cos 2\pi t_1 + 4\pi t_1 = \beta, \tag{3.23}$$

$$\Phi'(t_1) = -\delta\hat{c_2}e^{-\delta t_1} - 2\pi\varepsilon\sin 2\pi t_1 + 4\pi = -v_1. \tag{3.24}$$

If we subtract (3.21) from (3.23) and use (3.22) to substitute for $\hat{c_2}$, we have

$$\frac{1}{\delta}\left(4\pi - \hat{v} - 2\pi\varepsilon\sin 2\pi\hat{t}\right)\left(e^{-\delta(t_1-\hat{t})}-1\right)+\varepsilon(\cos 2\pi t_1-\cos 2\pi\hat{t})+4\pi(t_1-\hat{t})-2\beta = 0, \tag{3.25}$$

to solve for t_1, for which the convergence issues are similar to those for case (a) discussed in Section 3.1.2. Note that for small δ, the trajectory is approximately reversible in time and hence $2\hat{t} - t_0$ constitutes a good initial guess for t_1. Once t_1 is found, the corresponding impact velocity v_1 is given by (3.24).

We have constructed a complete map P for the impacting-contact model given by equations (2.28), (2.38), and we now proceed to construct a similar map for the piecewise-linear model equations (2.24), (2.26).

3.2 Construction of P for the piecewise-linear model

To calculate the Poincaré map P for the piecewise-linear model we can adapt the impact map described in Section 3.1 by replacing elastic impacts with the backlash boundaries with excursions into one of the linear stiffness regimes. As before we construct a map in time and velocity at the point of departure ($\Phi' < 0$) from the $\Phi = +\beta$ boundary to the next such departure, noting attraction to permanent linear contact if no such departure exists.

In contrast to the impacting-contact model, where the robustness of our numerical procedures can be guaranteed, here we have to proceed by formal arguments which nevertheless appear to converge to the correct root in all cases that we have examined. Details of proofs have not been attempted.

Consider a trajectory with initial data $-\beta < \Phi \leq +\beta$ and $\Phi' < 0$. As before, such a trajectory must impact either $\Phi = +\beta$ or $\Phi = -\beta$ at some subsequent time. We note that any crossing of the $\Phi = -\beta$ boundary from freeplay must be followed by another crossing of $\Phi = -\beta$ back into freeplay, by the following argument.

At a turning point $\Phi' = 0$ in $\Phi \leq -\beta$ we have

$$\Phi'' = -2\kappa\beta + 4\pi\delta - 2\kappa\Phi - 2\pi\varepsilon(4\pi^2 + \delta^2)^{\frac{1}{2}}\cos(2\pi t + \xi), \tag{3.26}$$

UNIVERSITY OF BRISTOL LIBRARY
ENGINEERING

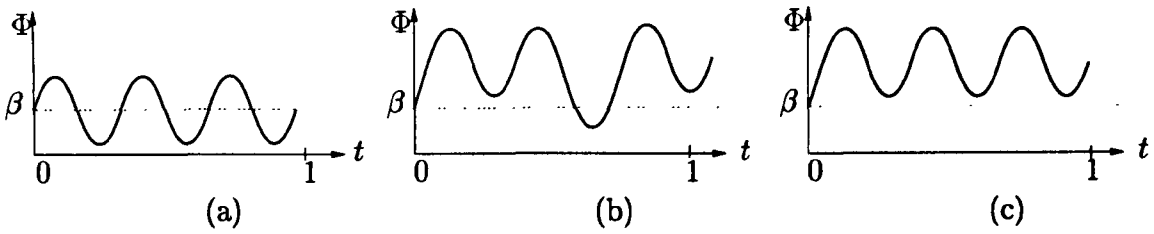

Figure 3.4. Sketches of three example trajectories departing from $\Phi = +\beta$ with $\Phi' > 0$. From left to right: (a) the trajectory oscillates between linear contact and freeplay, (b) trajectory returns to freeplay (within one gross rotation) after several maxima and minima in linear contact, (c) the trajectory stays in permanent linear contact.

where ξ is a phase shift. This expression is always positive provided

$$\varepsilon < \frac{2\delta - (\beta + \Phi)}{(4\pi^2 + \delta^2)^{\frac{1}{2}}}. \tag{3.27}$$

Since equation (2.36) holds and $\Phi \leq -\beta$ in this regime, this bound is always satisfied and there can be no local maxima in the torque reversal regime.

Let us now consider trajectories where $\Phi > +\beta$ and $\Phi' > 0$, i.e., a trajectory in the linear contact regime with positive velocity. There can be many maxima and minima of Φ before the trajectory re-crosses the $\Phi = +\beta$ section and returns to the freeplay region, if it in fact does ever return. We assume that if a trajectory does not re-cross $\Phi = +\beta$ within one gross rotation that it will never re-cross and it will remain in the linear contact regime for all time, i.e., permanent linear contact. Some example trajectories with initial data $\Phi = +\beta$ and $\Phi' > 0$ are illustrated in Figure 3.4.

To locate exit points from the linear contact regime, and hence re-crossings of $\Phi = +\beta$, we must first find the maxima (and minima, if any) within it. Unfortunately, it is not possible to find these maxima and minima in closed form. However, we can calculate good approximations, motivated by the relative sizes of terms, as outlined below.

The general solution of (2.26) in the linear contact regime has the form

$$\Phi(t) = \sqrt{A^2 + B^2} e^{-\frac{\delta t}{2}} \cos(qt + \zeta) + \beta + \frac{2\pi\delta}{\kappa} + p\cos(2\pi t + \lambda), \tag{3.28}$$

where A and B are constants of integration which can be expressed in terms of the

initial conditions, and

$$\zeta = \arctan\left(-\frac{A}{B}\right), \tag{3.29}$$

$$q = \sqrt{2\kappa - \frac{\delta^2}{4}} \approx \sqrt{2\kappa}, \tag{3.30}$$

$$p = -\pi\varepsilon\sqrt{\frac{4\pi^2+\delta^2}{(\kappa-2\pi^2)^2+\pi^2\delta^2}} \approx -\frac{2\pi^2\varepsilon}{\kappa}, \tag{3.31}$$

$$\lambda = \arctan\left(\frac{\delta(\kappa-2\pi^2)-2\pi^2\delta}{\pi\delta^2-2\pi(\kappa-2\pi^2)}\right) \approx -\frac{\delta}{2\pi}. \tag{3.32}$$

To determine if an exit from the linear contact regime is possible we must find the turning points of (3.28). We require t_m such that $\Phi'(t_m) = 0$, i.e.,

$$-q\sqrt{A^2+B^2}e^{-\frac{\delta t_m}{2}}\sin(qt_m+\zeta)-\frac{\delta}{2}\sqrt{A^2+B^2}e^{-\frac{\delta t_m}{2}}\cos(qt_m+\zeta)-2\pi p\cos(2\pi t_m+\lambda) = 0. \tag{3.33}$$

Equation (3.33) cannot be solved in closed form. However, if we examine both the frequencies and amplitudes of the three sinusoidal terms we can identify the leading order terms. We note that the first two terms of (3.33) oscillate significantly faster, rate $O(\sqrt{\kappa})$, than the third term, rate $O(1)$ and hence there is a decoupling of time scales. In addition, the amplitude of the first term, is proportionately considerably larger than that of the second, by a ratio $O(\sqrt{\kappa})$ to $O(\delta)$.

Hence, as a good approximation to the solution of equation (3.33) we solve:

$$\sin(qt_m+\zeta) = 0 \quad \Rightarrow t_m = \frac{m\pi-\zeta}{q}, \tag{3.34}$$

where $m \in \mathbb{Z}$. Equation (3.34) approximates a maximum of (3.28) if m is odd and a minimum if m is even.

We can then use t_m to to determine if a crossing of $\Phi = +\beta$ exists within one gross rotation (namely if there exists a $\Phi(t_m) < +\beta$ with m even) and further to bracket such a crossing. Due to the possibility of multiple crossings of $\Phi = +\beta$, we cannot guarantee that Newton's method will locate the correct (i.e. the first) root, and hence we employ instead a combination of interval bisection and secant methods. That is, we use (3.34) to approximate the first minimum of $\Phi < +\beta$, as well as the previous maximum, which together bracket the root. Equation (3.28) then gives the exact values of Φ' at the interval endpoints; if both are negative the secant method should locate the crossing of $\Phi = +\beta$ with superlinear convergence. If the gradients are of different sign, see Figure 3.5, we can use interval bisection until the gradients are of the same sign; the secant method can then be applied with confidence.

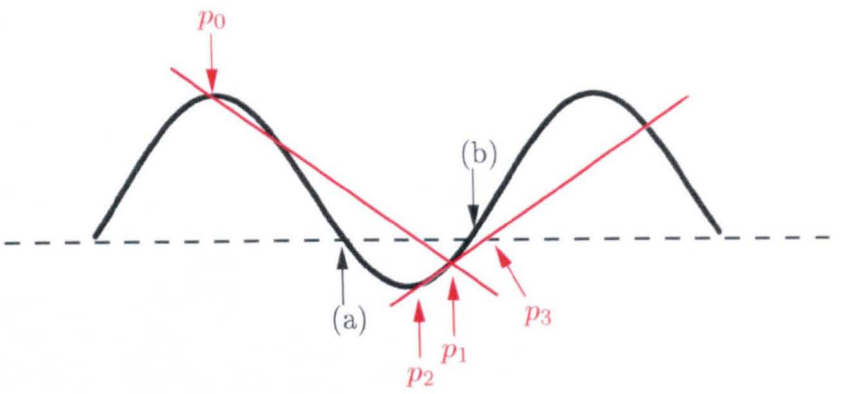

Figure 3.5. A schematic diagram illustrating how the secant method can fail to locate the correct (first) root, and why in certain cases we need to initially use the method of interval bisection. The first two iterations of the secant method are shown. The black curve illustrates the function, the red lines are the secants and the initial guesses are denoted by p_i. Since the gradient is positive at p_1 and p_2 the root at (b) is located, instead of the root at (a).

A similar method can be used to find the minimum in $\Phi \leq -\beta$ to locate an initial guess for the exit point from the torque reversal regime.

Our method (for initial conditions departing from $\Phi = +\beta$ with negative velocity) can be summarised as follows.

- Identify whether the the next crossing is with $\Phi = +\beta$ or $\Phi = -\beta$ using the pre-computed grazing curve.
- If the next crossing is with $\Phi = -\beta$:
  - Locate the next crossing of $\Phi = -\beta$ using the Poincaré map for the impacting-contact model.
  - Approximate the minimum that occurs in $\Phi \leq -\beta$.
  - Temporarily neglect the existence of the freeplay region, and approximate the next maximum (note that this maximum is non-physical)
  - The root of $\Phi = -\beta$ is bracketed by this minimum and the maximum.
  - Apply the secant method to locate the crossing.
- Use the Poincaré map for the impacting-contact model to locate the next crossing of $\Phi = +\beta$.
- To determine whether the trajectory remains in permanent linear contact, or not:

- Temporarily neglect the existence of the freeplay region, and approximate the first minimum that occurs in $|\Phi| < \beta$ within one gross rotation (note that this minimum is non-physical). If there is no such minimum this initial condition is marked as one that results in PLC.
- Approximate the previous maximum.
- The root of $\Phi = +\beta$ is bracketed by this minimum and the maximum.
- Use (3.28) to find the exact gradients of Φ at the interval endpoints.
- If the gradients of both points are negative, use the secant method to locate the crossing of $\Phi = +\beta$.
- If the gradients at these points are of different signs, use interval bisection until the new endpoints are both negative. Apply the secant method to locate the crossing.

Having constructed the Poincaré map P for the full piecewise-linear model, (see equations (2.24), (2.26)), in addition to that for the impacting-contact model, (see equations (2.28), (2.38)), we now proceed to describe how they are used to compute the basins of attraction of solutions of these models.

3.3 Cell-to-cell mapping in nonsmooth systems

Our objective is to calculate the basins of attraction of both the full piecewise-linear and impacting-contact gear rattle models (see (2.24), (2.26) and (2.28), (2.38)), by the brute-force simulation of a large number of initial conditions. To this end, we employ the method of *cell-to-cell mapping* [27, 28], applied to the Poincaré maps P defined in Sections 3.1 and 3.2. The region of interest (in this instance a closed bounded subset of the domain of P, namely the time and velocity (t, v) of departures from $\Phi = +\beta$) is divided into a uniform rectangular grid of cells, where each cell has a unique cell number associated with it, see Figure 3.6.

The centre point of each cell (t^c, v^c) corresponds to one set of initial data. The dynamics of the system are described by a mapping, in our case the Poincaré map $P : (t_i, v_i) \mapsto (t_{i+1}, v_{i+1})$. This mapping can then be applied to each initial condition to yield a 'cellular' form of the Poincaré map, which we call a *cell-map* $P_{\text{cell}} : (t_i^c, v_i^c) \mapsto (t_{i+1}^c, v_{i+1}^c)$ which maps cell-centres to cell-centres (or, equivalently, cells to cells). The cell-map is a composition of the Poincaré map P, and a 'correction' map P_{corr} that maps points to the nearest cell-centre (see Figure 3.7(a)). We now know to which cell in the grid each initial condition maps. The implicit assumption is that all points within

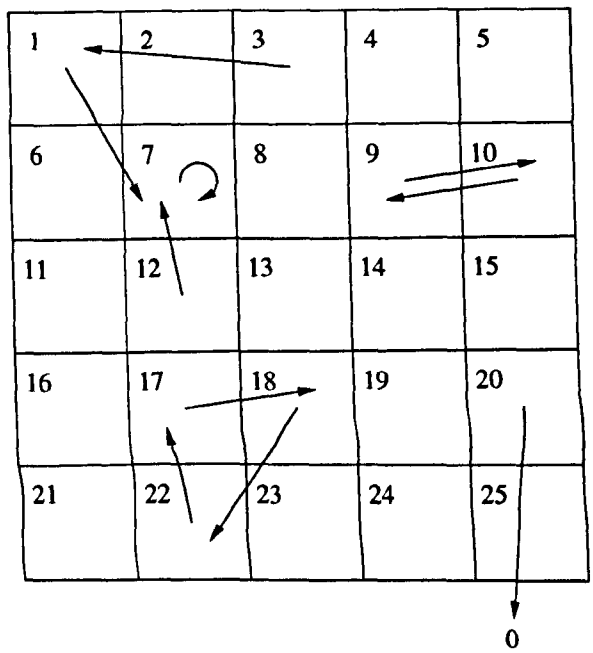

Figure 3.6. An example cell-map. {1, 3, 12} all belong to the basin of 7, a fixed point. {9, 10} and {17, 18, 22} make up period-2 and period-3 orbits, respectively. Cell 20 maps outside the grid.

a given cell map to the same cell; a finer grid gives better accuracy, but requires more computation. In principle, as we let the cell-size tend to zero, the cell-map will converge to the Poincaré map itself. As there are a finite number of cells in this framework, every cell in the cell-map is either a periodic attractor or maps outside the grid. One implication of this is that chaotic solutions cannot be directly identified, but can be inferred as being solutions of large period, which increases as cell-size tends to zero.

Solutions with small damping, δ, as is characteristic for the systems we study, suffer from particularly long transients. To determine the long term behaviour we adapt Hsu's method [43]. We apply the Poincaré map to each initial condition and record the terminal positions. We then repeat this procedure many times using the 'uncorrected' terminal points as the new starting conditions. That is, we compute $P_{\text{corr}}(P^k(t^c, v^c))$, rather than $P^k_{\text{cell}}(t^c, v^c)$; see Figure 3.7(b). This method is akin to long time integration to eliminate transients but is computationally much cheaper, yet more accurate than a simple iteration of the cell-map. We need to be careful in choosing the number of iterations, k, of the Poincaré map to ensure that the correct periodicity is calculated. A simple way to do this, without the need for any extra computer code, is to choose k to be a large prime number. In this way the true periodicity of each basin of period less than k (from the point of view of the cell-map) is calculated.

To efficiently extract the global properties from the mapping, algorithms described in

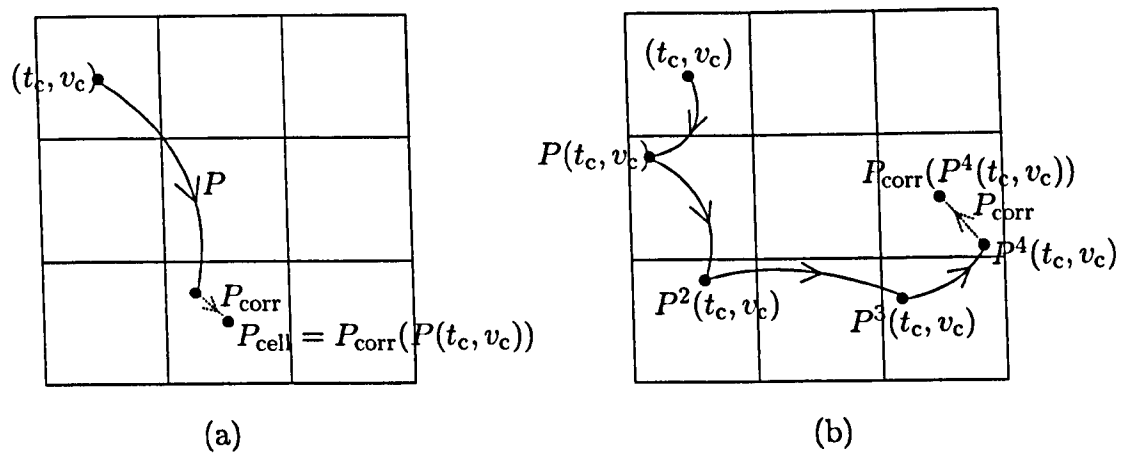

Figure 3.7. Schematic illustrations of (a) the cell-map P_{cell}, and (b) the map we use to minimise the effect of long transients $P_{\text{corr}} \circ P^k$, where the Poincaré map P is applied k times (here $k = 6$) followed by the correction map, P_{corr} to re-centre the terminal point.

[27, 28] can be employed to determine all the information that we require for constructing the basins of attraction, see Figure 3.8. For each cell there are three possibilities: the cell is a *periodic cell*, i.e., this cell belongs to a periodic orbit; the cell is mapped outside the grid, or the cell is mapped into a periodic cell. For each cell the algorithm assigns: a group number (basin number), a periodicity number (the number of impacts of $\Phi = +\beta$ before the trajectory repeats itself), and a step number (the number of steps it takes to map this particular cell into a periodic cell). Note that there are as many group numbers as there are periodic orbits, and that a step number of zero implies a periodic cell.

In what follows, we will use the cell-to-cell mapping technique to explore the solution of the gear-rattle models by computing their basins of attraction. For the purposes of visualisation, we colour each basin according to its itinerary, i.e., the pattern of impacts that occur with both backlash boundaries. Shorter itineraries are represented by shorter wavelength (bluer) colours. At the two extremes of the colour scale; dark blue denotes behaviour akin to permanent linear contact and red denotes chaotic behaviour. This results in a uniform colour scale across the results below; the same colour in more than one picture denotes the same solution type.

To identify the many different periodic solutions, we use the notation introduced in Section 2.4.1. Recall that $P(m, n^+, n^-)$ denotes a periodic solution, of period $m \in \mathbb{Z}$, where $n^{\pm}$ denote the number of times per period that the orbit impacts/crosses the $\Phi = \pm\beta$ boundaries, respectively. Whilst this notation is useful it does not apply to all solution types, or identify the order in which impacts of $\Phi = +\beta$ and $\Phi = -\beta$ occur (so that there are sometimes sets of solutions which are not distinguishable from one another by this notation).

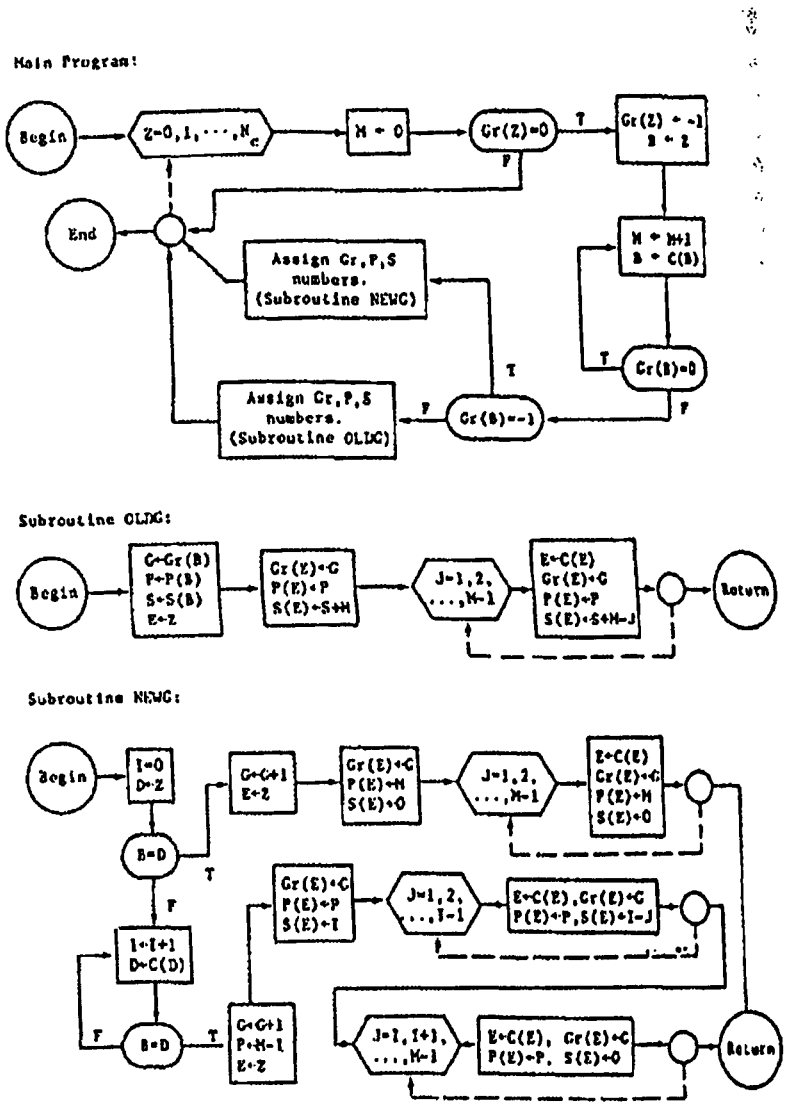

Figure 3.8. Flow chart for Hsu's algorithm for assigning group (Gr), period (P) and step (S) numbers for each cell. Reproduced from *An Unravelling Algorithm for Global Analysis of Dynamical Systems: An Application of Cell-to-Cell Mappings* by C.S. Hsu and R.S. Guttalu (Journal of Applied Mechanics 1980) [28].

It is important to emphasise here the subtle difference between periodicity and impact periodicity. As we use an impact-based map, the periodicity that we calculate is the impact periodicity; this is the number of times the trajectory impacts $\Phi = +\beta$ before repeating. For example, in one time period $t \in [0, 1]$ a solution may impact $\Phi = +\beta$ twice (with different velocities) before repeating, therefore having an impact periodicity of two, but a period of one in terms of the forcing period.

3.4 Basin of attraction computations

To investigate changes in the dynamics as parameters are varied, we perform three sets of numerical experiments: we vary stiffness, eccentricity and damping in turn, and observe how the solution structure changes, by computing basins of attraction and bifurcation diagrams. Each basin-of-attraction plot presented in this section (Figures 3.9–3.13 and Figures 3.15–3.19) illustrates the cell-map $P_{\text{corr}} \circ P^k$ computed on a regular grid of 1000 × 1000 cells, where each cell represents a different initial condition. We experimented with different grid sizes, and found that 1000×1000 cells was the optimum trade-off between accuracy and computation time. As described above, k is chosen to be a large prime; here we use $k = 1499$, as we find that using a larger prime does not result in any visible changes in the basins. In each case, the grazing curve is overlaid in white, and the scale is chosen so that transitions either side of the grazing curve can be observed.

3.4.1 Varying stiffness

We begin by examining the effect of varying stiffness κ in the piecewise-linear model, given by equations (2.24), (2.26), with fixed damping $\delta = 0.6$, eccentricity $\varepsilon = 0.1$, and backlash $\beta = 0.6$. We have chosen these parameters as scaled-up versions of the realistic machine parameters. The results of these computations are shown in Figure 3.9; we show the basins of attraction where stiffness changes by an order of magnitude between each panel, increasing from $\kappa = 100$ to $\kappa = 100000$.

We also compare the dynamics of the piecewise-linear model, (2.24), (2.26) with the impacting-contact model (2.28), (2.38), at the same values of δ, β and ε. The basins of attraction are shown in Figure 3.10, for both models, where the stiffness has been taken to be an order of magnitude bigger again ($\kappa = 1000000$). Figure 3.10 also illustrates several common solution types under the two different models:

- The basin of permanent linear contact (PLC) solutions is represented in dark blue.

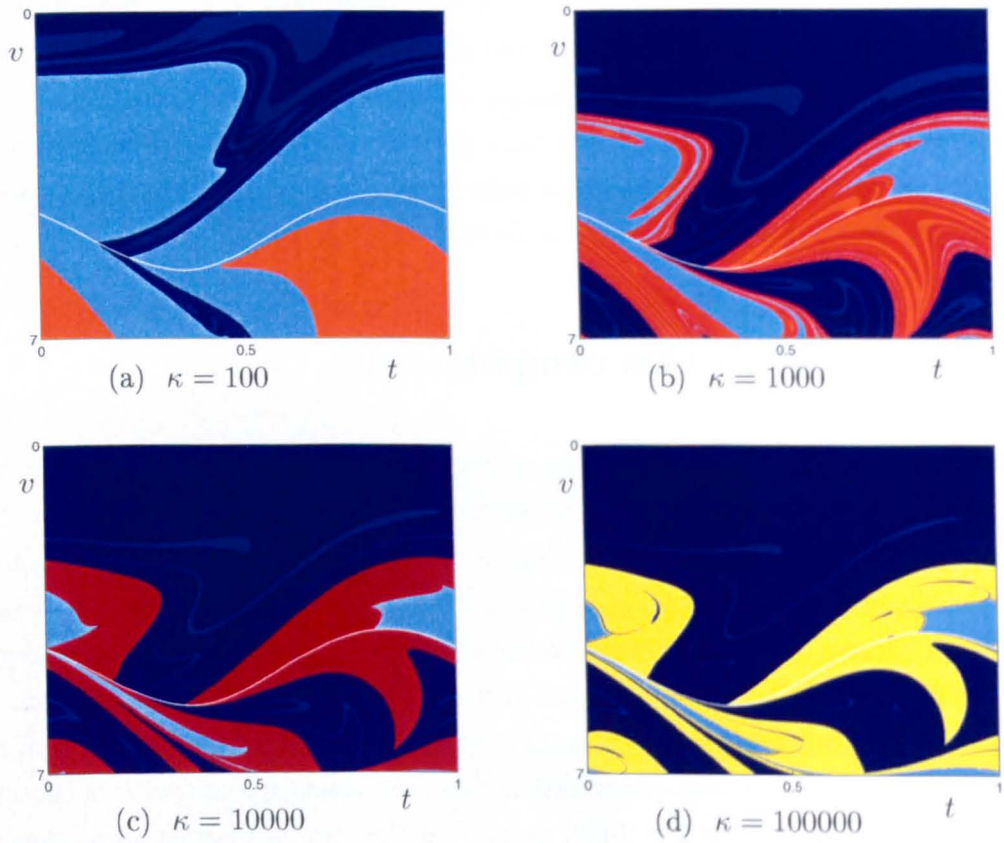

Figure 3.9. Basins of attraction for the piecewise-linear model, given by equations (2.24), (2.26), when $\delta = 0.6$, $\beta = 0.6$, $\varepsilon = 0.1$ and for varying stiffness κ (indicated below each panel). Each plot has time on the x-axis and velocity on the y-axis. The grazing curve is overlaid in white. Computations were performed using the cell-to-cell mapping techniques described in Section 3.3.

- A chaotic region is shown in speckled dark red.
- The basin of the $P(1,1,0)$ solutions, very close to grazing, is shown in pale blue.
- The basin of the $P(1,2,0)$ solutions, which is revealed only by the PWL model, is shown in blue.

The time histories of these solutions are all labelled with arrows. The periodic attractors are overlaid on the basins of attraction in white ($\times$). To generate the chaotic attractors (since these cannot be directly identified using cell-to-cell mapping) we repeatedly iterate the Poincaré map to an initial condition in the chaotic regime, remove the transients, and plot the impact times and velocities on top of the basin of attraction in black.

We observe from Figure 3.10 that the basins of attraction for the impacting-contact model and full piecewise-linear model as $\kappa \to \infty$ are very similar, except for one small

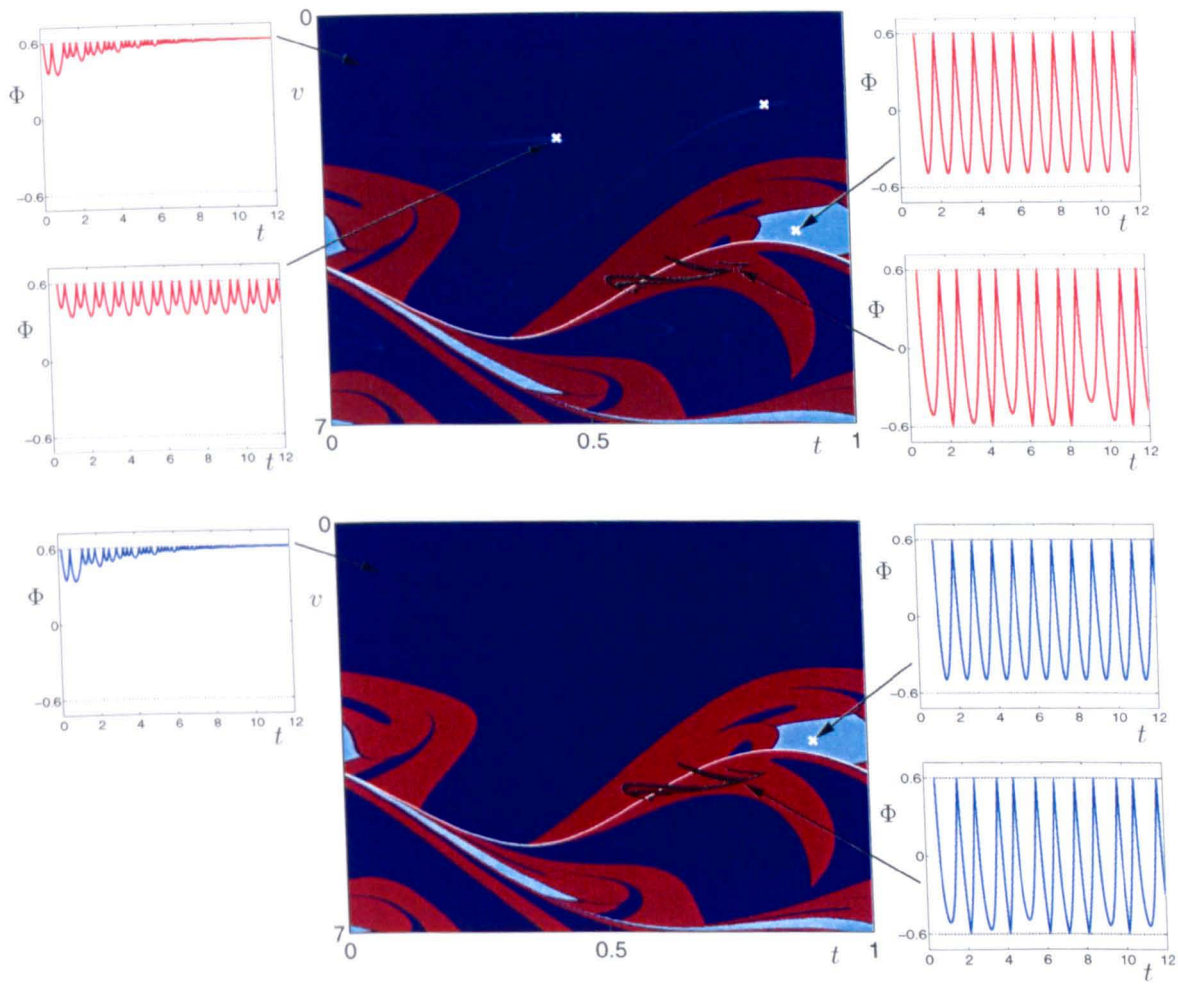

Figure 3.10. Basins of attraction for the PWL model (top) given by equations (2.24), (2.26) and impacting-contact model (bottom) given by equations (2.28), (2.38). In both models $\delta = 0.6$, $\beta = 0.6$, $\varepsilon = 0.1$, and for the PWL model $\kappa = 1 \times 10^6$. The periodic and chaotic attractors are overlaid on the basins in white ($\times$) and black, respectively. Time histories, $\Phi(t)$ versus t, of the periodic and chaotic attractors for both models are illustrated next to the corresponding basin of attraction.

basin as already noted. In the case of the impacting-contact model, the basin of PLC solutions is replaced by one where the solution has multiple, very low velocity impacts with $\Phi = +\beta$. Figure 3.9 shows that the qualitative agreement between the PWL and the impacting-contact models improves as κ increases. We shall therefore exclusively work with the impacting-contact model for the remainder of this chapter. We defer the full analysis of the differences between two models for future work.

3.4.2 Varying eccentricity

We now go on to examine the effect of varying eccentricity ε in the impacting-contact model given by equations (2.28), (2.38) with fixed damping $\delta = 0.6$ and backlash $\beta = 0.6$. The results of these computations are shown in Figure 3.11; we show the basin of attraction plots where eccentricity increases in increments of 0.0055 from 0.056 to 0.1.

We note that although the PLC bound (2.36) is satisfied, there are several coexisting solutions. As ε decreases, the dynamics decrease in complexity as expected. At $\varepsilon = 0.067$ (Figure 3.11(c)) there are only two basins, corresponding to solutions which repeatedly impact $\Phi = +\beta$ with very low velocity (akin to PLC) and solutions of type $P(1,1,0)$. As ε decreases further the basin of $P(1,1,0)$ solutions shrinks until it completely disappears and PLC takes over. This occurs at the predicted bound for the existence of the $P(m,1,0)$ solutions which is computed in Section 2.4.4 and given by

$$\varepsilon > \frac{m^2\delta^2}{6} - \frac{m^4\delta^4}{360} + O(\delta^6). \tag{3.35}$$

Substituting the values of ε and δ used in the simulation, we find the bound for the existence of $P(1,1,0)$ solutions, $\varepsilon > 0.05964$, is in good agreement with our results, see Figure 3.11. However, in practice ε and δ are of similar magnitude, and it is very difficult to eliminate rattling solutions by reducing eccentricity.

3.4.3 Varying damping

We now proceed to examine the effect of varying damping in the impacting-contact model (2.28), (2.38) with fixed eccentricity $\varepsilon = 0.1$ and backlash $\beta = 0.6$. The results of these computations are shown in Figure 3.12; we show the basin of attraction plots where damping increases in increments of 0.025 from 0.5 to 0.7.

We make several observations:

- The plots decrease in complexity as damping increases until all initial conditions result in behaviour akin to PLC, as in Figure 3.12(i).

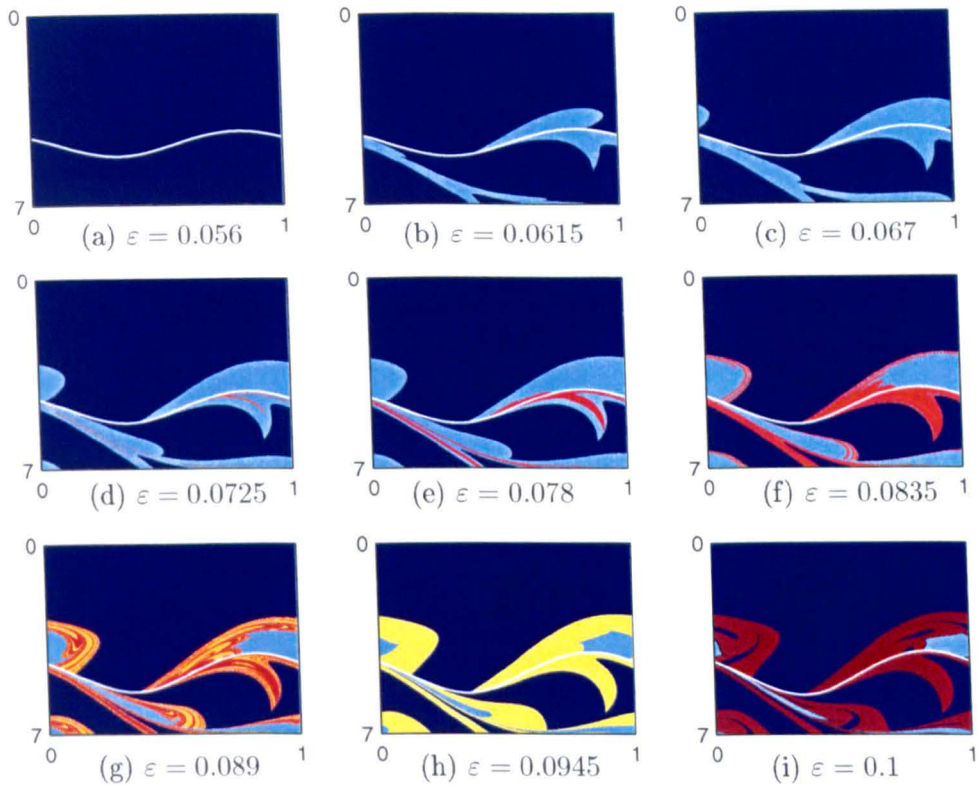

Figure 3.11. Basins of attraction for the impacting-contact model, given by equations (2.28), (2.38), for $\delta = 0.6$, $\beta = 0.6$ and varying eccentricity, between $\varepsilon = 0.056$ and $\varepsilon = 0.1$. Each plot has time, t on the x-axis and velocity, v on the y-axis. In case (a) all initial conditions result in behaviour akin to permanent linear contact.

- As damping increases, between $\delta = 0.575$ (Figure 3.12(d)) and $\delta = 0.6$ (Figure 3.12(e)), a solution of type $P(1,2,0)$ is destroyed. Similarly between $\delta = 0.5$ (Figure 3.12(a)) and $\delta = 0.525$ (Figure 3.12(b)), a $P(1,3,0)$ orbit is destroyed.

- The chaotic region in Figure 3.12(e), in speckled red, that we illustrated earlier, see Figure 3.10, is periodic for lower values of damping, e.g. in Figure 3.12(b) (orange) and Figure 3.12(d) (yellow).

To understand some of the mechanisms by which solutions are created and destroyed, we plot one-parameter bifurcation diagrams of impact velocity v as damping δ is varied, see Figures 3.13(a) and 3.14. To generate these bifurcation diagrams we take an initial condition and iterate the Poincaré map many times, and for each damping value the last twenty impact velocities are plotted. To ensure that the same orbit is followed we use 'pseudo-continuation': the last impact time and velocity for one value of δ are used

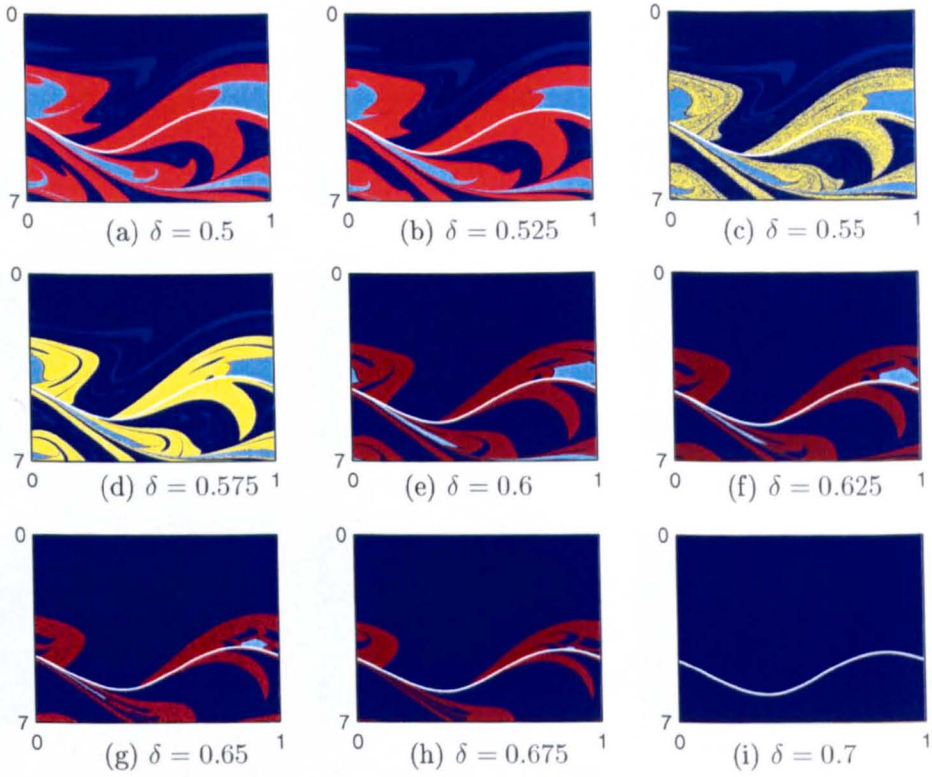

Figure 3.12. Basins of attraction for the impacting-contact model, given by equations (2.28), (2.38), for $\beta = 0.6$, $\varepsilon = 0.1$ and varying damping, between $\delta = 0.5$ and $\delta = 0.7$. Each plot has time on the x-axis and velocity on the y-axis. In case (i) all initial conditions result in behaviour akin to permanent linear contact.

as the initial conditions for the next value of δ.

Initially, we investigate the basin that disappears between $\delta = 0.575$ and $\delta = 0.6$. In Figure 3.13(a) we plot both the $P(1,2,0)$ attractor and saddle in red at $\delta = 0.575$. We apply the continuation-type method to the impact time and magnitude of velocity at the attractor. By increasing damping (until $\delta = 0.6$) we obtain two branches of solutions which we plot in solid black lines. The location of the saddle points as damping is varied are calculated using DsTool (Dynamical Systems Toolkit) [5] and the branches are plotted as dashed black lines. At $\delta = 0.5997$ we find a saddle-node bifurcation, i.e., a collision of the attractor and an unstable saddle, resulting in the destruction of this orbit and the disappearance of this basin. The basins of attraction before, at, and after the saddle-node bifurcation are also shown in Figures 3.13(b), 3.13(c) and 3.13(d), respectively, with attractors ($\times$) and saddles ($+$) overlaid.

We now examine how the $P(3,3,2)$ periodic orbit that exists at $\delta = 0.5$, with basin

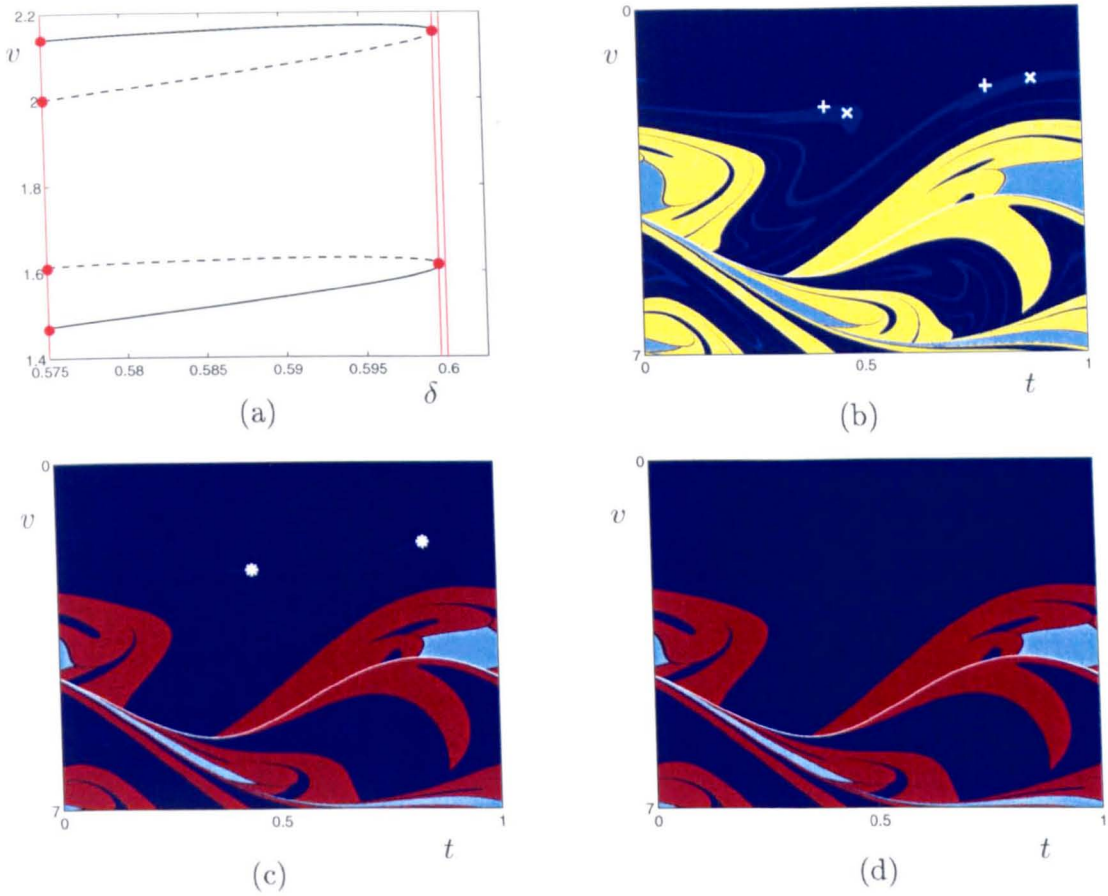

Figure 3.13. (a) Bifurcation diagram of a $P(1,2,0)$ solution, in the impacting-contact model, given by equations (2.28), (2.38), of impact velocity against damping, for fixed $\beta = 0.6$ and $\varepsilon = 0.1$. As damping increases this solution is destroyed in a saddle-node bifurcation at $\delta = 0.5997$ (the stable and unstable branches are plotted in solid and dashed lines, respectively). Basins of attraction (b) before, (c) at, and (d) after the saddle-node bifurcation. The attracting and saddle-type $P(1,2,0)$ solutions ($\times$ and $+$, respectively) are overlaid. As damping increases these move closer to each other until they collide in a saddle-node bifurcation (c) at $\delta = 0.5997$. (d) The basin is destroyed by $\delta = 0.6$.

of attraction coloured orange in Figure 3.12(a), changes as δ increases. We apply the continuation-type method described above, increasing δ until $\delta = 0.6$, and plot the magnitude of the velocity of departure from $\Phi = +\beta$ after transients have died away for successive values of δ; shown in green in Figure 3.14. We then apply the same continuation method in reverse, using the final impact time and velocity at $\delta = 0.6$, decreasing δ until $\delta = 0.5$. The magnitude of the velocity of departure is overlaid on Figure 3.14 in black. We observe coexisting solutions (e.g. at A) as well as both period-doubling (e.g. at B) and discontinuity-induced bifurcations (e.g. at C). We proceed to investigate points A, B and C in more detail.

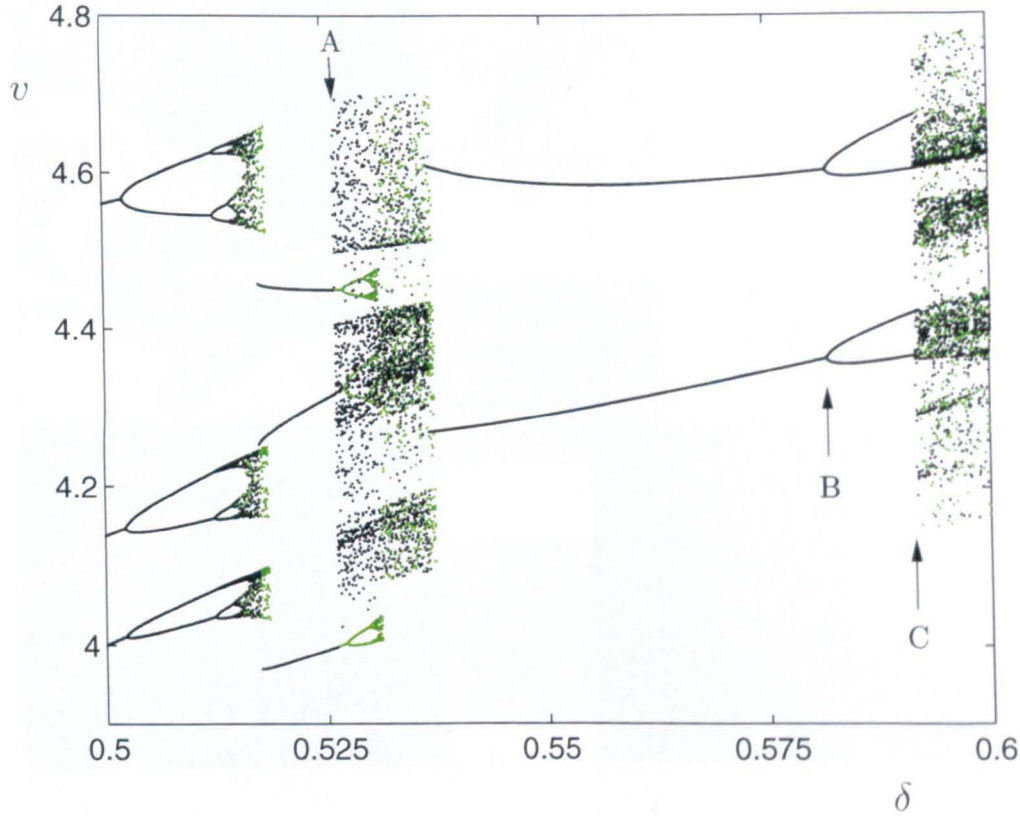

Figure 3.14. Bifurcation diagram of impact velocity against damping for the impacting-contact model, given by equations (2.28), (2.38) , for $\beta = 0.6$ and $\varepsilon = 0.1$, plotted for increasing (green) and decreasing (black) δ. An example of coexisting attractors is labelled at (A). Examples of period-doubling and a grazing bifurcation are labelled at (B) and (C), respectively.

At $\delta = 0.527$, marked as A on Figure 3.14, there is a chaotic attractor (black) which coexists with a $P(3,3,2)$ attractor (green). The basins of attraction at this value of δ are plotted in Figure 3.15(a). The coexisting attractors are depicted as intertwined dark and light orange basins, and their corresponding time histories are shown in Figures 3.15(b) and 3.15(c).

Finally, we examine the $P(2,2,1)$ periodic orbit, at $\delta = 0.575$. This orbit period-doubles at $\delta = 0.5819$ (marked as B on Figure 3.14) to become a $P(4,4,2)$ orbit. It then undergoes a discontinuity-induced bifurcation at $\delta = 0.5922$ (marked as C on Figure 3.14) where the orbit collides with the grazing curve, to be replaced by the chaotic attractor whose basin surrounds the grazing periodic orbit. Basins of attraction and the time histories (of the attractors described above) for values of δ before and at the discontinuity-induced bifurcation are shown in Figures 3.16(a) and 3.16(b), respectively.

In summary, we have found that small changes in damping can cause a plethora of

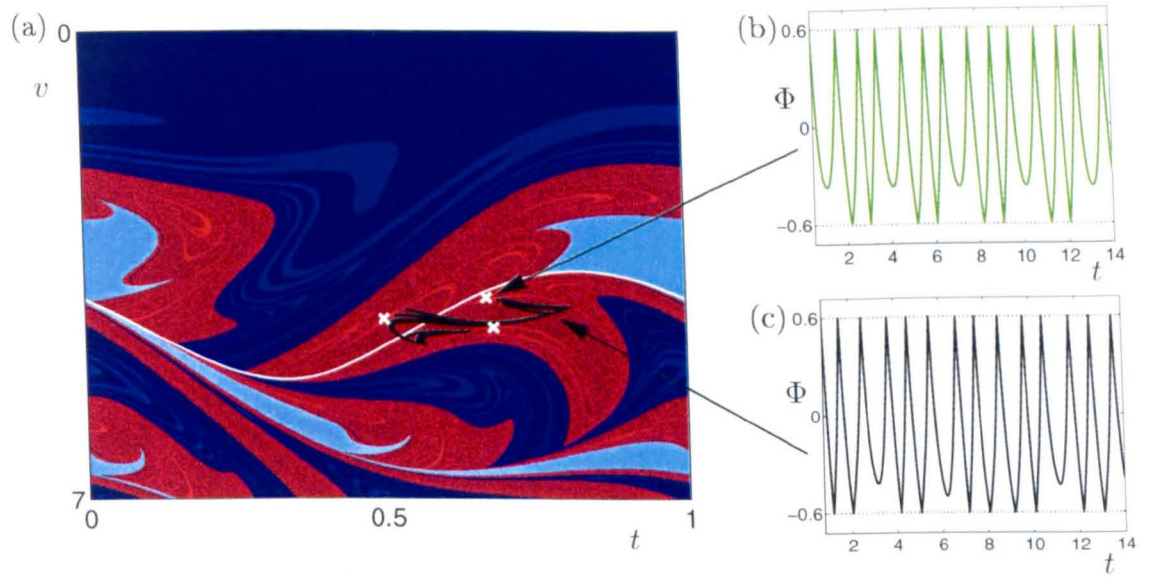

Figure 3.15. (a) Basins of attraction for the impacting-contact model, given by equations (2.28), (2.38), when $\delta = 0.527$, $\beta = 0.6$, $\varepsilon = 0.1$. A $P(3,3,3)$ and a chaotic attractor are overlaid on the basins in white ($\times$) and black, respectively. Time histories, $\Phi(t)$ versus t, of stable $P(3,3,2)$ periodic motion (light orange basin), and the coexisting chaotic motion (dark orange basin) are plotted in panels (b) and (c).

smooth and discontinuity-induced bifurcations. As damping increases enough, however, we see that all initial conditions result in behaviour akin to permanent linear contact. Despite the desirability of PLC from a machine-design point of view, significantly increased damping is not a viable engineering solution, as power consumption is directly proportional to the damping and hence increasing δ would make a machine more expensive to run. It seems inevitable, therefore, that any design solution will have to take account of the coexistence of different types of rattling solutions, and that the basins of attraction may be a useful tool to help understand their structure.

3.5 Basin boundary computations

Although we have been concerned with time-efficient computation of basins of attraction, they are still expensive to compute. We now explore two alternative methods to gain insight about the location of the basin boundaries for the impacting-contact model: calculation of the pre-images of the grazing curves, and the computation of stable manifolds.

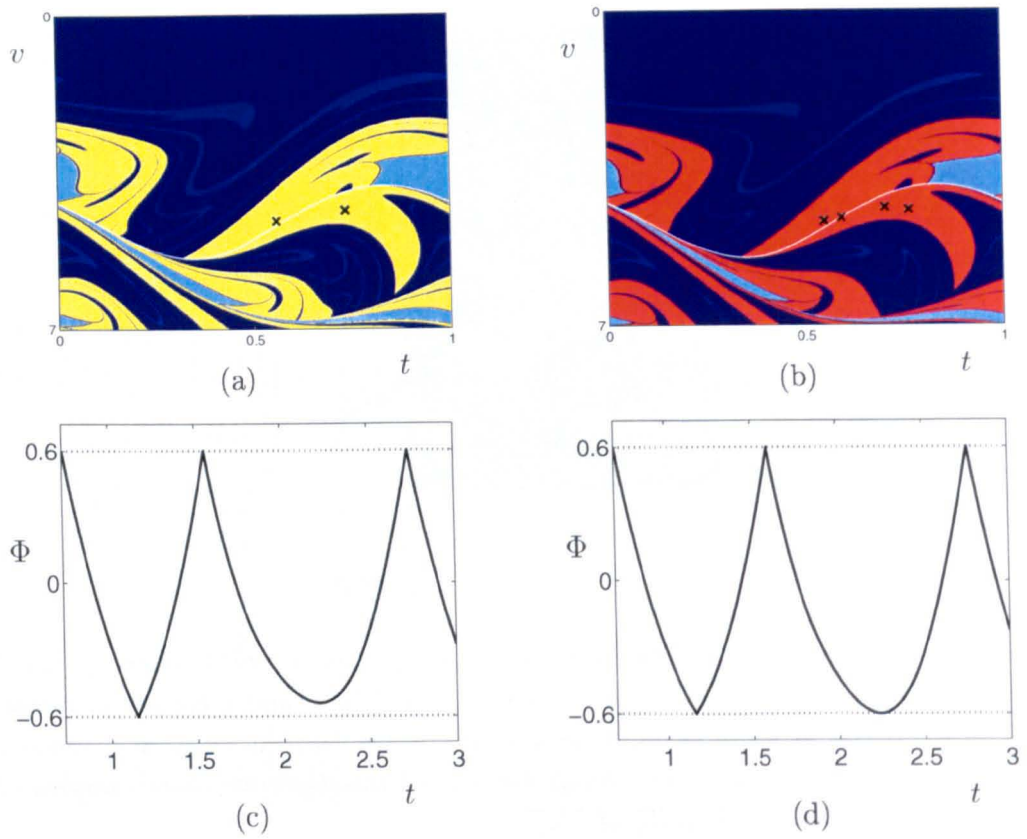

Figure 3.16. Basins of attraction of the impacting-contact model, equations (2.28), (2.38), with fixed $\beta = 0.6$ and $\varepsilon = 0.1$ and (a) $\delta = 0.575$ and (b) $\delta = 0.5922$. $P(2,2,1)$ and $P(4,4,2)$ attractors are overlaid on the basins in black ($\times$) in (a) and (b), respectively. Time histories, $\Phi(t)$ versus t, of a stable $P(2,2,1)$ solution at $\delta = 0.575$ and a grazing $P(4,4,2)$ solution at the discontinuity-induced bifurcation at $\delta = 0.5922$ are plotted in panels (c) and (d).

3.5.1 Pre-image grazing curves

Much of the intricate structure of the basins of attraction can be explained by the impact-induced discontinuities in the Poincaré map. These discontinuities can introduce a considerable sensitivity to initial conditions, i.e., a stretching of the phase space, which in particular can be observed around the grazing curve. Other authors have already studied this in detail (see, for example [6–8, 33]).

Recall that the grazing curve is defined by trajectories that depart $\Phi = +\beta$ at time t with velocity $\Phi' = -v^*$, and whose next contact with $\Phi = \pm\beta$ is a graze with $\Phi = -\beta$ (i.e., with velocity $\Phi' = 0$). We can then define pre-images of this curve in (t, v) space with respect to the Poincaré map P; namely the first pre-image are those initial conditions (t, v) that lead to a graze following one more impact with $\Phi = +\beta$ (possibly via an impact with $\Phi = -\beta$), the second pre-image are those initial conditions

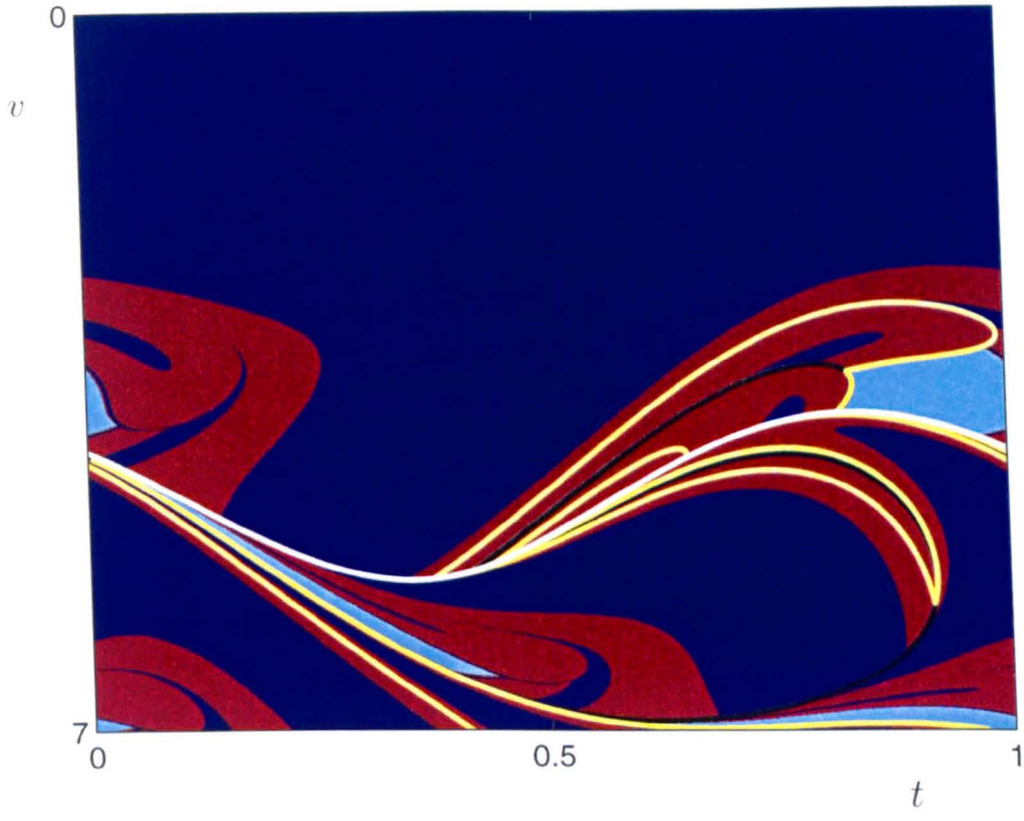

Figure 3.17. The grazing curve (white) and first and second pre-images of the grazing curve (black and yellow, respectively) overlaid on the basin of attraction for the impacting-contact model equations (2.28), (2.38) for $\delta = 0.6$, $\beta = 0.6$ and $\varepsilon = 0.1$. The pre-images were computed using the Newton solvers constructed in Section 3.1 with time reversed.

(t, v) that graze following two further impacts with $\Phi = +\beta$, and so on.

As an example, in Figure 3.17 we overlay the first and second pre-images of the grazing curve for $\delta = 0.6$, $\beta = 0.6$ and $\varepsilon = 0.1$ on the corresponding basins of attraction.

Pre-images of the grazing curve can also provide insight on which initial conditions will eventually be affected by the discontinuity and how the phase space is divided. As previously discussed, the grazing curve acts as a separatrix of trajectories whose next impact is with either $\Phi = +\beta$ or $\Phi = -\beta$. Similar conclusions can be drawn from the pre-images of the grazing curve. For example the first pre-image consists of two curves. The first piece of curve (above the grazing curve) represents trajectories that initially impact $\Phi = +\beta$, and then graze $\Phi = -\beta$. This acts as a separatrix between trajectories whose second impact is with either $\Phi = +\beta$ or $\Phi = -\beta$.

3.5.2 Manifold computations

It is well known that for smooth systems, the stable manifolds of saddle points form the basin boundaries [21]. We suspect that this will also be true for our nonsmooth system.

First, we locate saddle points using explicit construction techniques described in 2.4.2. We then calculate manifolds numerically using DsTool [5] with the extension package, Man1D, discussed in [19, 31]. As an example, we calculate the saddles and corresponding manifolds for $\delta = 0.6$, $\beta = 0.6$ and $\varepsilon = 0.1$. The unstable $P(1,1,0)$ saddle can be located analytically, whilst the unstable $P(1,1,1)$ saddle is calculated numerically.

In Figure 3.18 we overlay the $P(1,1,0)$ and $P(1,1,1)$ saddles (at A and B) and their corresponding manifolds (magenta and green, respectively) on the relevant basins of attraction. We discover that these manifolds form the basin boundaries, at least to the resolution of our computations, as expected.

We now examine the manifold and pre-image curves, and their interactions with the boundaries of the basins of attraction, more closely. In Figure 3.19 we overlay the grazing curve (white), the first and second pre-images of the grazing curve (black and yellow) and the stable manifolds (magenta and green) on a zoomed section of the basin of attraction. We observe that the stable manifolds form the basin boundaries exactly, whilst the grazing curve and its pre-images only approximate some of the locations of the basin boundaries. However, the pre-image grazing curves are cheap to compute as we can use the Newton solvers constructed in Section 3.1 with time reversed. In contrast, computing the stable manifolds requires a good deal more computation. Firstly, the saddles have to be calculated, and secondly DsTool requires the inverse of the Poincaré map as well as the Poincaré map itself.

If we plot the manifolds over a larger range of initial velocity v, (Figure 3.20) an intricate pattern of stretching and folding is revealed. Trajectories with a large v gradually lose energy through damping, until they are attracted into the region of interest, $v \in [0,7]$.

3.6 Discussion

In this chapter we have examined techniques to efficiently compute basins of attraction for the piecewise-linear model and the impacting-contact approximation of our basic gear rattle model. We used cell-to-cell mapping techniques to explore how basins change as system parameters are varied. The basins that we have computed reveal

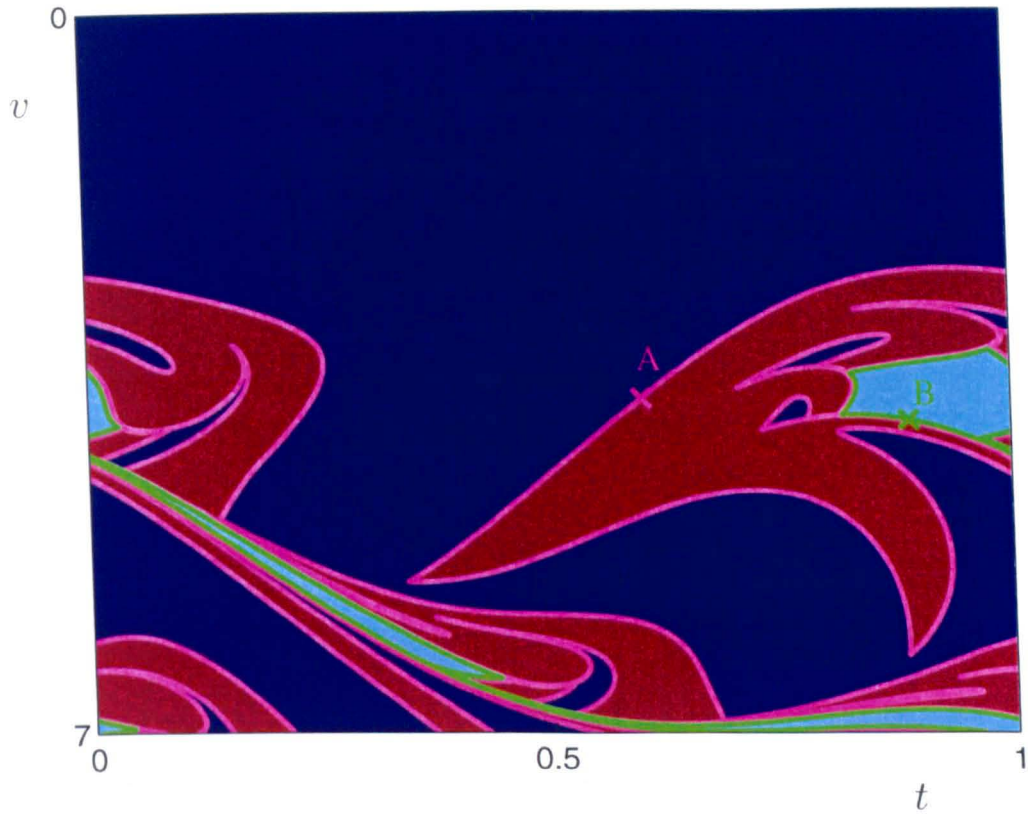

Figure 3.18. The stable manifolds of the $P(1,1,0)$ saddle at A (magenta) and the $P(1,1,1)$ saddle at B (green) overlaid on the basin of attraction for the impacting-contact model given by equations (2.28), (2.38) for $\delta = 0.6$, $\beta = 0.6$ and $\varepsilon = 0.1$. The manifolds were generated with DsTool [5, 19, 31].

complex dynamics with rich and delicate structure. We find stable periodic solutions, and in some cases chaotic regions, that correspond to rattling behaviour. Moreover, these solution types coexist with a quiet solution in which gears remain permanently in contact. The purpose of the basin computations has been to analyse the relative dominance of competing linearly stable solutions in the $t \to \infty$ dynamics.

We have compared the basins of attraction when three key parameters have been varied, namely the stiffness, eccentricity and damping. In the large stiffness limit, we have shown that the impacting-contact model is in very good agreement with the full piecewise-linear model, validating its use as a computationally efficient scheme. We have found that even small changes in the forcing and damping parameters can give rise to complex dynamics and one-parameter bifurcation diagrams have illuminated some of the key mechanisms for transitions in the system's behaviour. Finally, as eccentricity is reduced, or damping increased, the basin diagrams simplify in structure, and we

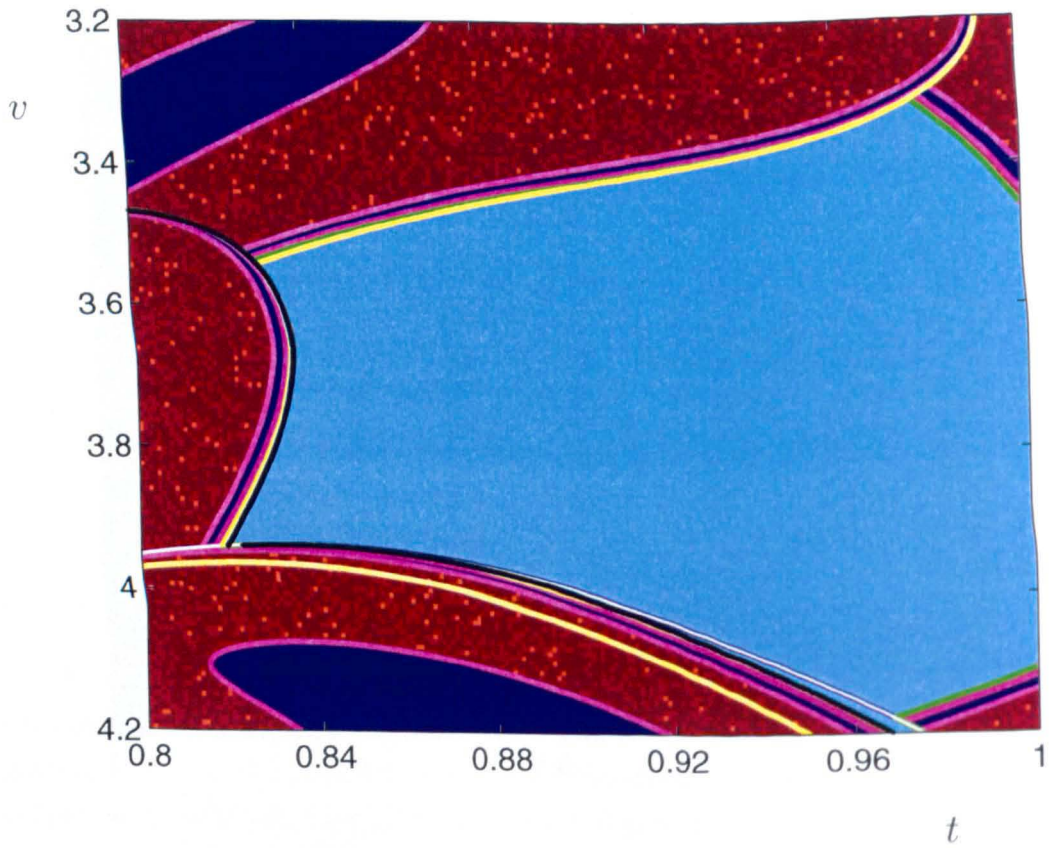

Figure 3.19. A zoomed section of the grazing curve (white), the first and second pre-images of the grazing curve (black and yellow) and the stable manifolds (magenta and green) overlaid on the basin of attraction for the impacting-contact model, given by equations (2.28), (2.38) for $\delta = 0.6$, $\beta = 0.6$ and $\varepsilon = 0.1$.

have shown how the quiet solution, for which gears remain in permanent linear contact, dominates the $t \to \infty$ dynamics.

In addition to the basin computations, we have also computed the grazing curve and its pre-images since these play an important role in the stretching and folding of phase space. In addition, we have used DsTool to compute the one-dimensional stable manifolds of saddle point periodic orbits, thus accessing basin boundaries directly. We have found that the stable manifolds and grazing curves wind round each other in interesting ways which are worthy of further investigation from a theoretical point of view. Furthermore, nonsmooth numerical bifurcation tools (e.g., the TC-HAT [55] extension to AUTO) could be applied to obtain a more detailed understanding of the bifurcations of periodic orbits themselves.

Finally, from the point of view of applications such as the Roots booster pump, we need to extend the work presented here to deal with much smaller values of damping

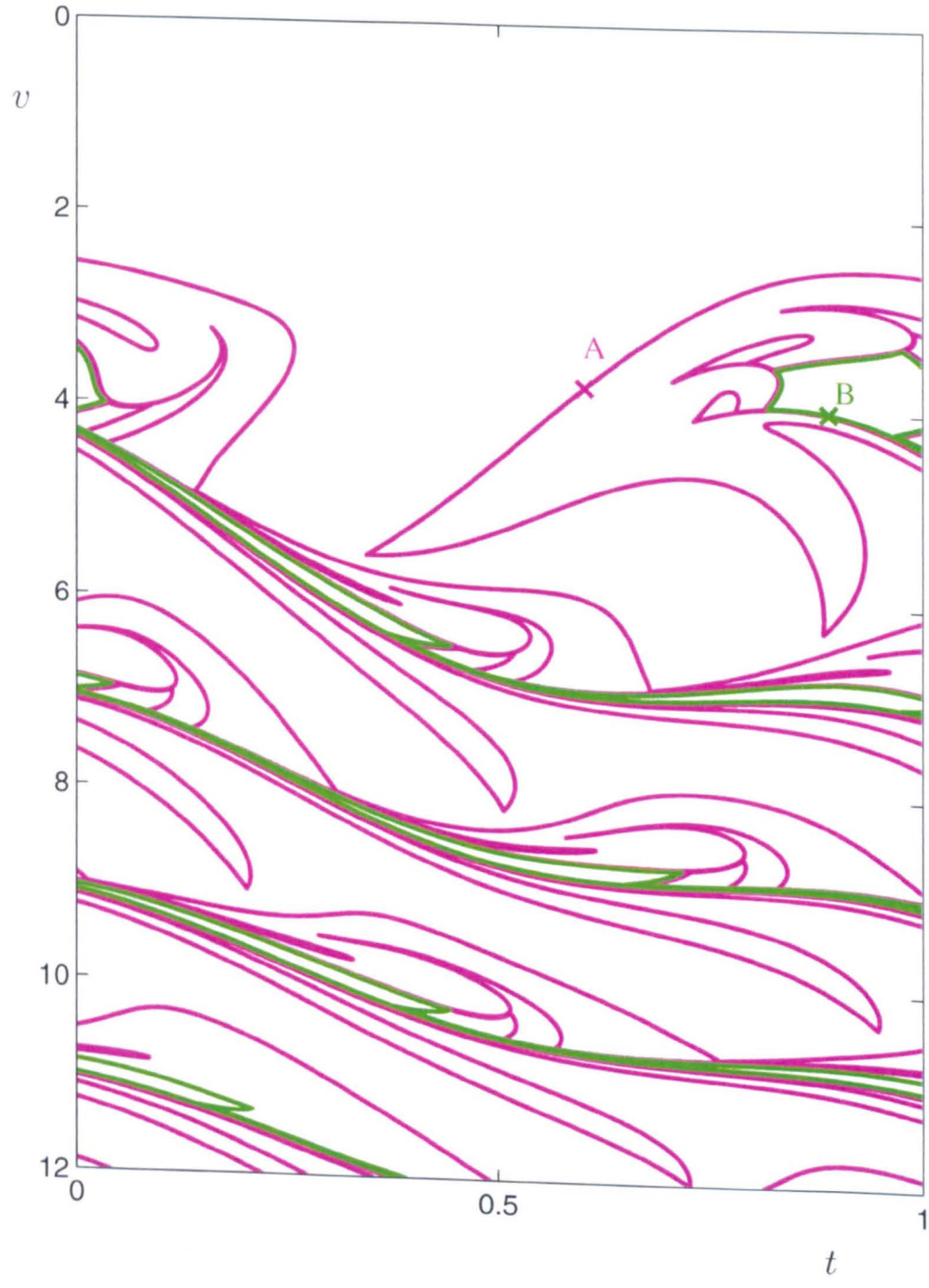

Figure 3.20. The stable manifolds of Figure 3.18 plotted over an extended velocity scale to illustrate the intricate stretching and folding.

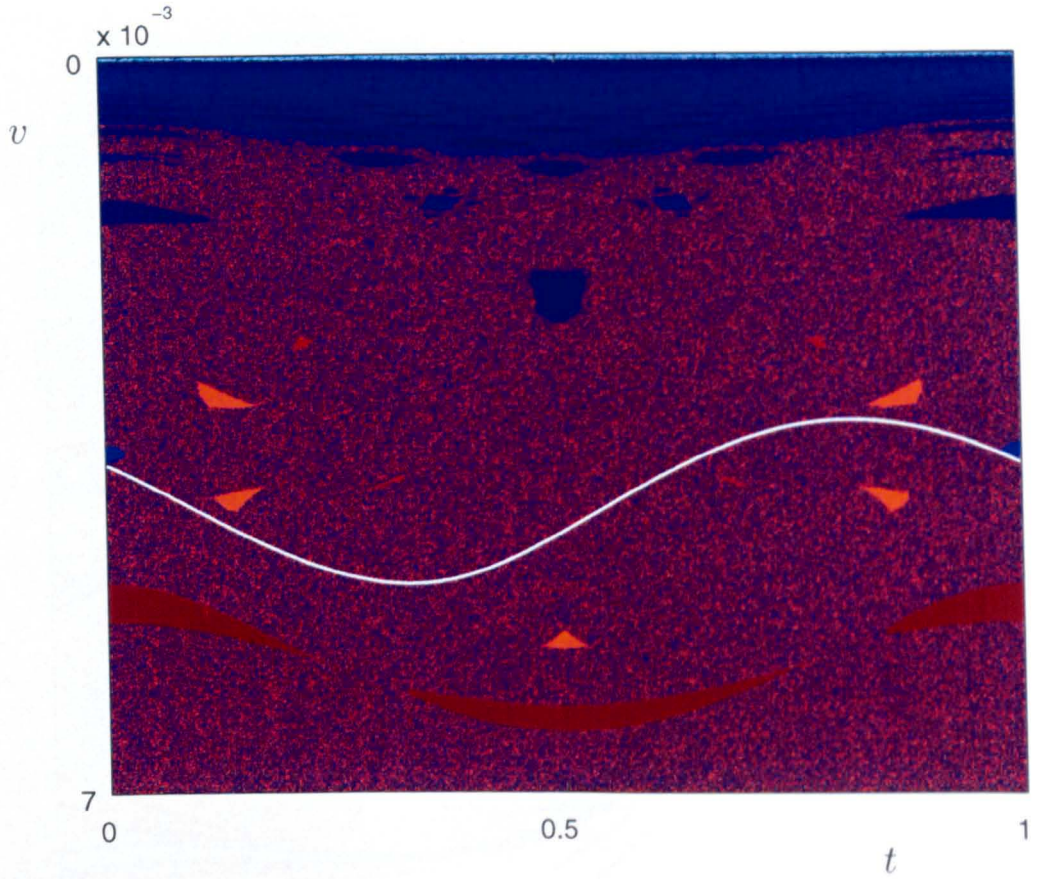

Figure 3.21. Basins of attraction for the impacting-contact model, given by equations (2.28), (2.38) for realistic machine parameters $\delta = 6 \times 10^{-4}$, $\beta = 6 \times 10^{-4}$, $\varepsilon = 1 \times 10^{-4}$.

and forcing, and this presents a significant computational challenge. Preliminary computations have indicated a much more intricate and fragmented picture: see Figure 3.21 for a basin of attraction plot for typical machine parameters. We also find that basins diminish in size and more periodic orbits are created (through saddle-node bifurcations) as parameters are decreased.

We note that Roots boosters exhibit noisy operation only intermittently. Our basin of attraction diagrams indicate that only a small change in the initial data is required to move from a basin that corresponds to quiet operation to a basin that corresponds to rattle. A sufficiently large disturbance, which could be caused by any number of external factors, provides one possible explanation for the observed intermittency.

Chapter 4

Two Proposed Design Solutions

In the previous chapter we explored some of the complex dynamics of the simple one degree-of-freedom model. We now proceed to investigate two proposed design solutions for reducing gear rattle in Roots booster pumps.

It has been suggested [20] that adding a flywheel to the X- (driven) shaft of the pump may increase the critical eccentricity, and this motivates the next model that we shall investigate. The single degree-of-freedom, second-order, model that we derived in Chapter 2 required that the ratio of the moments of inertia and damping coefficients of the X- and Y-shaft assemblies are equal. In Section 4.1 we will extend the existing model to a two degree-of-freedom model where the moments of inertia of the two shaft assemblies are allowed to differ and θ_X and θ_Y can be regarded as independent co-ordinates. In addition, we will examine the effect of adding or removing mass from the pump. We shall be particularly concerned with the effect that this has on the critical eccentricity bound (derived in Section 2.3 for the one degree-of-freedom model). This motivates a discussion in Section 4.2 of the implications that breaking the symmetry has for real machine design. However, since satisfying the critical eccentricity bound does not guarantee silent operation, we shall also investigate how the nonlinear rattling solutions are affected, using the two types of rattling solution described in Section 2.4 as illustrative examples.

The remainder of this chapter shall be devoted to another design solution for reducing gear rattle, suggested by BOCE; the so called 'sprung-gear' system (patent pending [12]). The core idea is that vibrations can be reduced by mounting the driving (X-) gear on the X-shaft by means of a torsional spring. This motivates the introduction of a three degree-of-freedom model in Section 4.4. We calculate a new critical eccentricity in Section 4.4.3 and compare this to the original system. Finally, in Section 4.5 we compare the relative merits of the two design solutions.

A first version of Sections 4.1–4.3 appeared in the Master's thesis *Mathematical Modelling of Gear Rattle in Dual-Shaft Vacuum Pumps* (2004) [37]. Material from this chapter has also been published in the Journal of Sound and Vibration (co-authors M.E. Homer and R.E. Wilson) [38].

4.1 Symmetry-broken machine

The general approach is to derive and analyse models in which the moments of inertia I_X, I_Y of the shaft assemblies are assumed to be unequal.

4.1.1 Two degree-of-freedom model

Initially, we return to the dimensional equations of motion (2.12) and (2.13) derived in Chapter 2 for the X- and Y-shaft assemblies, before the reduction to a single differential equation. By non-dimensionalising with the rotation period, such that $t = \Omega\tau$ as before, and dividing through by the average of the two moments of inertia $\overline{I}$, the system takes the form of a pair of coupled second-order ordinary differential equations,

$$\frac{I_X}{\overline{I}}\theta_X'' + \frac{c}{\Omega\overline{I}}\theta_X' + \frac{kr}{\Omega^2\overline{I}}B(\theta_X - \theta_Y + e(t)) = \frac{T(t)}{\Omega^2\overline{I}}, \tag{4.1}$$

and

$$\frac{I_Y}{\overline{I}}\theta_Y'' + \frac{c}{\Omega\overline{I}}\theta_Y' - \frac{kr}{\Omega^2\overline{I}}B(\theta_X - \theta_Y + e(t)) = 0. \tag{4.2}$$

For algebraic convenience we introduce a new non-dimensional parameter $\eta \in (-1, 1)$, to measure the broken symmetry, i.e., the ratio of mass removed from one shaft and added to the other, where

$$\frac{I_X}{\overline{I}} = 1 + \eta, \quad \text{and} \quad \frac{I_Y}{\overline{I}} = 1 - \eta, \quad \text{where } \overline{I} = \frac{I_X + I_Y}{2}, \tag{4.3}$$

so that

$$\begin{aligned} I_X &= I_Y \quad \Rightarrow \quad \eta = 0, \\ I_X &\gg I_Y \quad \Rightarrow \quad \eta \simeq 1, \\ I_X &\ll I_Y \quad \Rightarrow \quad \eta \simeq -1. \end{aligned}$$

If we substitute the expressions for η into equations (4.1) and (4.2) we have

$$(1+\eta)\theta_X'' + \delta\theta_X' + \kappa B(\theta_X - \theta_Y + e(t)) = T(t), \tag{4.4}$$

and

$$(1-\eta)\theta_Y'' + \delta\theta_Y' - \kappa B(\theta_X - \theta_Y + e(t)) = 0. \tag{4.5}$$

Here, neglecting the torque ripple as before, the motor torque T is defined by $T = \alpha = 4\pi\delta$, θ_X and θ_Y are the rotational displacements of the X- and Y-shafts, respectively, and the scaling is such that the damping δ, eccentricity ε and stiffness κ coefficients take the same values as for the one degree-of-freedom model (see equation (2.25)). It is possible to re-write equations (4.4) and (4.5) as a system of three first-order equations by introducing new co-ordinates, (Θ, χ, Z), defined by

$$\Theta = \theta_X - \theta_Y, \tag{4.6}$$

$$\chi = \Theta', \tag{4.7}$$

$$Z = \theta'_X + \theta'_Y. \tag{4.8}$$

Equations (4.4) and (4.5) are thus transformed to give

$$\begin{pmatrix} 1 & 0 & 0 \\ 0 & 1 & \eta \\ 0 & \eta & 1 \end{pmatrix} \begin{pmatrix} \Theta' \\ \chi' \\ Z' \end{pmatrix} = \begin{pmatrix} 0 & 1 & 0 \\ 0 & -\delta & 0 \\ 0 & 0 & -\delta \end{pmatrix} \begin{pmatrix} \Theta \\ \chi \\ Z \end{pmatrix} + \begin{pmatrix} 0 \\ \alpha \\ \alpha \end{pmatrix} + \begin{pmatrix} 0 \\ -2\kappa B(\Theta + e(t)) \\ 0 \end{pmatrix}. \tag{4.9}$$

In practice, we shall often work with the re-normalised relative angular displacement $\Phi = \Theta + e(t)$, with $\Psi := \Phi'$, so we can recast (4.9) in the form

$$\begin{pmatrix} 1 & 0 & 0 \\ 0 & 1 & \eta \\ 0 & \eta & 1 \end{pmatrix} \begin{pmatrix} \Phi' \\ \Psi' \\ Z' \end{pmatrix} = \begin{pmatrix} 0 & 1 & 0 \\ 0 & -\delta & 0 \\ 0 & 0 & -\delta \end{pmatrix} \begin{pmatrix} \Phi \\ \Psi \\ Z \end{pmatrix} + \begin{pmatrix} 0 \\ \alpha + e''(t) + \delta e'(t) - 2\kappa B(\Phi) \\ \alpha + \eta e''(t) \end{pmatrix}. \tag{4.10}$$

The surprise here is that equations (4.9) and (4.10) are non-autonomous third-order, whereas one might expect a fourth-order system since (4.4) and (4.5) constitute a pair of second-order equations. In fact this reduction in order is due to the elimination of the $\theta_X \mapsto \theta_X + C$, $\theta_Y \mapsto \theta_Y + C$ symmetry (where C is a constant).

4.1.2 Permanent linear contact solutions

We now turn our attention to the simplest, quietest type of solution where the X-shaft continuously drives the Y-shaft, without loss of contact. In particular, we will calculate

a new bound on the eccentricity above which silent solutions cannot exist, and examine how this bound depends on η.

To calculate the critical eccentricity for the two degree-of-freedom model we must first solve the three coupled equations of motion (4.9) in the X drives Y regime. The easiest way to solve these equations is in matrix form. In permanent linear contact (PLC), X drives Y, so we can substitute $B(\Theta + e(t)) = \Theta + e(t) - \beta$, which yields

$$\underbrace{\begin{pmatrix} 1 & 0 & 0 \\ 0 & 1 & \eta \\ 0 & \eta & 1 \end{pmatrix}}_{M} \underbrace{\begin{pmatrix} \Theta' \\ \chi' \\ Z' \end{pmatrix}}_{u'} = \underbrace{\begin{pmatrix} 0 & 1 & 0 \\ -2\kappa & -\delta & 0 \\ 0 & 0 & -\delta \end{pmatrix}}_{A} \underbrace{\begin{pmatrix} \Theta \\ \chi \\ Z \end{pmatrix}}_{u} + \underbrace{\begin{pmatrix} 0 \\ \alpha + 2\kappa\beta \\ \alpha \end{pmatrix}}_{b_1} + \begin{pmatrix} 0 \\ -2\kappa e(t) \\ 0 \end{pmatrix}. \tag{4.11}$$

The eccentricity term can be written as

$$e(t) = \Re\{\varepsilon \exp 2\pi t\mathrm{i}\}, \tag{4.12}$$

where $\Re$ denotes the real part and i the square root of -1. If we write

$$b_2 = \begin{pmatrix} 0 \\ 2\kappa\varepsilon \\ 0 \end{pmatrix}, \tag{4.13}$$

then equation (4.11) can be expressed in the form

$$Mu' = Au + b_1 - \Re\{b_2 \exp 2\pi t\mathrm{i}\}. \tag{4.14}$$

We then substitute a particular solution of the form

$$u = c_1 + \Re\{c_2 \exp 2\pi t\mathrm{i}\}, \tag{4.15}$$

and compare coefficients to obtain expressions for c_1 and c_2,

$$c_1 = -A^{-1}b_1, \tag{4.16}$$

$$c_2 = (A - 2\pi\mathrm{i}M)^{-1}b_2. \tag{4.17}$$

For consistency, we require $\Theta(t) + e(t) > \beta$ for all time. Since Θ is the first component

of u, we have that

$$\Theta(t) + e(t) = \Re\{(c_{1,1} + (c_{2,1} + \varepsilon)\exp 2\pi t\mathrm{i})\}, \tag{4.18}$$

where $c_{1,1}$ and $c_{2,1}$ are the first components of $\boldsymbol{c}_1$ and $\boldsymbol{c}_2$, respectively given by

$$c_{1,1} = \frac{\alpha}{2\kappa} + \beta, \tag{4.19}$$

$$c_{2,1} = -\frac{\kappa\varepsilon(\delta + 2\pi\mathrm{i})}{\delta(\kappa - 4\pi^2) + ((\delta^2 + 2\kappa)\pi + 4\pi^3(\eta^2 - 1))\mathrm{i}}. \tag{4.20}$$

As in the one degree-of-freedom case the minimum displacement is given by

$$c_{1,1} - |c_{2,1} + \varepsilon|. \tag{4.21}$$

Therefore, for the existence condition to be fulfilled we need the inequality

$$c_{1,1} - |c_{2,1} + \varepsilon| > \beta \tag{4.22}$$

to be satisfied. If we use (4.19) to substitute for $c_{1,1}$ this bound becomes

$$\frac{\alpha}{2\kappa} > |c_{2,1} + \varepsilon|. \tag{4.23}$$

As $c_{2,1}$ is a multiple of ε we can rearrange equation (4.23) to give the following bound

$$\varepsilon < \varepsilon_{\text{crit}}^{2\text{ d.o.f.}} = \frac{2\delta}{\kappa}\sqrt{\frac{\delta^2(\kappa - 4\pi^2)^2 + \pi^2(\delta^2 + 2\kappa + 4\pi^2(\eta^2 - 1))^2}{16\pi^2\delta^2 + (\delta^2 + 4\pi^2(\eta^2 - 1))^2}}, \tag{4.24}$$

for the existence of PLC solutions. A simple rearrangement shows that

$$\varepsilon_{\text{crit}}^{2\text{ d.o.f.}} = \frac{2\delta}{\kappa}\sqrt{\frac{((\kappa - 2\pi^2)^2 + \pi^2\delta^2) + \frac{8\pi^4\eta^2}{4\pi^2 + \delta^2}(2(\kappa - 2\pi^2) + \delta^2 + 2\pi\eta^2)}{(4\pi^2 + \delta^2) + \frac{8\pi^2\eta^2}{4\pi^2 + \delta^2}((4\pi^2 - \delta^2) - 2\pi^2\eta^2)}}, \tag{4.25}$$

and it is now clear that substituting $\eta = 0$ (i.e., assuming that the moments of inertia of the two shafts are identical) recovers the critical eccentricity bound, $\varepsilon_{\text{crit}}^{1\text{ d.o.f.}}$, for the one degree-of-freedom model (2.36). In addition, if we fix δ and κ and expand equation

(4.24) as a binomial series in small η, we find that

$$\begin{aligned}\varepsilon_{\text{crit}}^{2\text{ d.o.f.}} &= \frac{2\delta}{\kappa}\sqrt{\frac{(\kappa-2\pi^2)^2+\pi^2\delta^2}{4\pi^2+\delta^2}} \\ &\quad + 8\pi^2\delta\eta^2\sqrt{\frac{(\kappa-2\pi^2)^2+\pi^2\delta^2}{4\pi^2+\delta^2}}\left(\frac{4\pi^2(\kappa-2\pi^2)-\delta^2\kappa+6\pi^2\delta}{(4\pi^2+\delta^2)^2(\kappa-2\pi^2)^2}\right)+O(\eta^4), \\ &= \varepsilon_{\text{crit}}^{1\text{ d.o.f.}}\left(1+\frac{4\pi^2\kappa(4\pi^2(\kappa-2\pi^2)-\delta^2\kappa+6\pi^2\delta)\eta^2}{(4\pi^2+\delta^2)^2(\kappa-2\pi^2)^2}+O(\eta^4)\right), \\ &\sim \varepsilon_{\text{crit}}^{1\text{ d.o.f.}}(1+\eta^2+O(\eta^4)).\end{aligned} \tag{4.26}$$

Once again, as $\kappa \to \infty$, $\varepsilon_{\text{crit}}$ is proportional to δ, so design changes that increase damping will increase $\varepsilon_{\text{crit}}$. Unfortunately, as already discussed in Section 2.3.2 these are generally undesirable from an engineering point of view. Equation (4.26) also indicates that for small η (and large κ), breaking the symmetry by removing mass from one shaft and adding it to the other increases $\varepsilon_{\text{crit}}$: i.e., a desirable effect. It is curious to note that η only appears as a quadratic term in (4.26) indicating that it does not matter which shaft we remove mass from (to add to the other).

4.2 Practical symmetry breaking

The advantage of the η parameter is that it allows easy manipulation of the equations of motion and does not change the values of the other non-dimensional parameters, as the total inertia of the system remains unchanged. However, in practice it is more useful to quantify the effect of adding or removing mass to or from just one shaft, or equally, to or from both shafts.

We thus introduce two new non-dimensional variables μ and ν: μ measures half the ratio of mass added or removed to *either one of* the X or Y-shafts, while ν measures half the ratio of mass added or removed to *each* shaft. Note that the parameters μ and ν result in the same total change in mass. Positive values of μ and ν correspond to the addition of mass, whilst negative values correspond to the removal of mass.

Initially, we investigate the effect that the addition or subtraction of mass from one shaft only has on the critical eccentricity. Here we show how the non-dimensional parameters η, δ and κ change under variation of μ. We can then substitute these values into (4.24) to generate a new expression for the critical eccentricity. We split into two cases:

(a) Add/remove mass to/from the X-shaft.

(b) Add/remove mass to/from the Y-shaft.

For case (a), we suppose

$$I_X = \overline{I}_{old}(1+2\mu) = (1+\eta)\overline{I}_{new}, \tag{4.27}$$
$$I_Y = \overline{I}_{old} = (1-\eta)\overline{I}_{new}. \tag{4.28}$$

For case (b), we suppose

$$I_X = \overline{I}_{old} = (1+\eta)\overline{I}_{new}, \tag{4.29}$$
$$I_Y = \overline{I}_{old}(1+2\mu) = (1-\eta)\overline{I}_{new}. \tag{4.30}$$

Here $\overline{I}_{old}$ and $\overline{I}_{new}$ denote the averages of the two shafts' moments of inertia before and after the addition (or removal) of mass, respectively. For both (a) and (b):

$$\overline{I}_{new} = \frac{1}{2}(I_X + I_Y) = \overline{I}_{old}(1+\mu), \tag{4.31}$$

$$\eta = \frac{I_X}{\overline{I}_{new}} - 1, \qquad \delta = \frac{c}{\Omega \overline{I}_{new}}, \qquad \kappa = \frac{k}{\overline{I}_{new}}. \tag{4.32}$$

Hence we derive the following changes in parameters under addition or removal of mass to or from one shaft.

- Add/remove mass to X-shaft:

$$\eta \longrightarrow \frac{\mu}{1+\mu}, \qquad \delta \longrightarrow \frac{\delta}{1+\mu}, \qquad \kappa \longrightarrow \frac{\kappa}{1+\mu}. \tag{4.33}$$

- Add/remove mass to Y-shaft:

$$\eta \longrightarrow -\frac{\mu}{1+\mu}, \qquad \delta \longrightarrow \frac{\delta}{1+\mu}, \qquad \kappa \longrightarrow \frac{\kappa}{1+\mu}. \tag{4.34}$$

We can now substitute these expressions to express the broken symmetry critical eccentricity (4.24) in terms of μ. Since η only appears as a quadratic term in (4.24), it does not matter whether we use equation (4.33) or (4.34). Physically, this corresponds to the fact that adding mass to the X-shaft has the same effect as adding mass to the Y-shaft. Hence (4.24) becomes

$$\varepsilon_{crit} = \frac{2\delta}{\kappa}\sqrt{\frac{\left((\frac{\kappa}{1+\mu} - 2\pi^2)^2 + \frac{\pi^2\delta^2}{(1+\mu)^2}\right) + \frac{8\pi^4\mu^2}{(1+\mu)^2}\left(2(\frac{\kappa}{1+\mu} - 2\pi^2) + \frac{\delta^2+2\pi\mu^2}{(1+\mu)^2}\right)}{\left(\frac{\delta^2}{(1+\mu)^2} + 4\pi^2\right) + \frac{8\pi^2\mu^2}{4\pi^2(1+\mu)^2+\delta^2}\left((\frac{\delta^2}{(1+\mu)^2} - 4\pi^2) + \frac{2\pi^2\mu^2}{(1+\mu)^2}\right)}}. \tag{4.35}$$

We expand (4.35) as a binomial series in small μ, for fixed δ and κ as above, to give

$$\varepsilon_{\text{crit}} = \varepsilon_{\text{crit}}^{1 \text{ d.o.f.}}(1 - \mu + 2\mu^2 + O(\mu^3)). \tag{4.36}$$

This indicates that for small μ, the critical eccentricity decreases as μ increases. We can also conclude that decreasing μ, i.e., removing mass from one shaft, increases $\varepsilon_{\text{crit}}$: a desirable effect. However, it is important to note that whilst our original parameter η is bounded ($-1 \leq \eta \leq 1$), positive μ is not ($-\frac{1}{2} < \mu < \infty$), so for completeness we proceed to examine how removing a large amount of mass affects the critical eccentricity, i.e., how large μ values affect (4.35). Re-writing (4.35) we have

$$\varepsilon_{\text{crit}} = \frac{2\delta}{\kappa}\sqrt{g(\mu)}, \tag{4.37}$$

where

$$g(\mu) := \frac{a + b\mu + c\mu^2}{d + e\mu + f\mu^2}, \tag{4.38}$$

and

$$a = (4\pi^2 + \delta^2)((\kappa - 2\pi^2)^2 + \pi^2\delta^2)^2, \tag{4.39}$$
$$b = 4\pi^2(\kappa - 4\pi^2)(2(\kappa - 2\pi^2) - \delta^2), \tag{4.40}$$
$$c = 4\pi^2((\kappa - 4\pi^2)^2 + 4\pi^2\delta^2), \tag{4.41}$$
$$d = (\delta^2 + 4\pi^2)^2, \tag{4.42}$$
$$e = 16\pi^2(\delta^2 + 4\pi^2), \tag{4.43}$$
$$f = 16\pi^2(\delta^2 + 4\pi^2). \tag{4.44}$$

We now show that $\varepsilon_{\text{crit}}$ is strictly monotone decreasing for $-\frac{1}{2} < \mu < \infty$; namely that $g'(\mu) > 0$, g is continuous, and $g(\mu) > 0$, for all $\mu > 0$. Specifically

$$g'(\mu) = -\frac{A\mu^2 + B\mu + C}{(d + e\mu + f\mu^2)^2}, \tag{4.45}$$

where

$$A = 64\pi^4\kappa(4\pi^2 + \delta^2)(\kappa - 4\pi^2 - \delta^2), \tag{4.46}$$
$$B = 8\pi^2\kappa(4\pi^2 + \delta^2)^2(3\kappa - 8\pi^2), \tag{4.47}$$
$$C = 4\pi^2\kappa(4\pi^2 + \delta^2)^2(\delta^2 + 2(\kappa - 2\pi^2)). \tag{4.48}$$

Note that the denominator of $g'(\mu)$ has no zeros, for $\mu > 0$ because $d, e, f > 0$. Thus, it only remains to show that the numerator is negative for negative μ. By inspection this is satisfied as $A, B, C < 0$, provided that $\kappa > 4\pi^2 + \delta^2$. We conclude that removing a

large amount of mass from either shaft increases $\varepsilon_{\text{crit}}$ whilst adding a large amount of mass to either shaft decreases $\varepsilon_{\text{crit}}$.

For comparison, we now proceed to investigate how adding or subtracting mass from both shafts, i.e., increasing or decreasing ν affects the critical eccentricity. We have that

$$\overline{I}_{\text{new}} = (1+\nu)\overline{I}_{\text{old}}. \tag{4.49}$$

Note that the parameters ν and μ result in the same total change in mass of the machine. The non-dimensional parameters δ and κ change under variation of ν so that

$$\delta \longrightarrow \frac{\delta}{1+\nu}, \qquad \kappa \longrightarrow \frac{\kappa}{1+\nu}. \tag{4.50}$$

Since we consider the addition or the removal of the same amount of mass from both shafts we can then substitute the expressions for ν into the original critical eccentricity bound for the one degree-of-freedom model (2.36) to generate a new expression. We find that

$$\varepsilon_{\text{crit}} = \frac{2\delta}{\kappa}\sqrt{\frac{(\frac{\kappa}{1+\nu} - 2\pi^2)^2 + \frac{\pi^2\delta^2}{(1+\nu)^2}}{4\pi^2 + \frac{\delta^2}{(1+\nu)^2}}}. \tag{4.51}$$

We expand (4.51) as a binomial series in small ν, for fixed δ and κ as above,

$$\varepsilon_{\text{crit}} = \varepsilon_{\text{crit}}^{1\text{ d.o.f.}}(1 - \nu + \nu^2 + O(\nu^3)). \tag{4.52}$$

Similarly to before, for small ν the critical eccentricity decreases as ν increases and decreasing ν increases $\varepsilon_{\text{crit}}$. However, if we compare (4.52) with (4.36), we note that given a choice, for small μ and ν it is better to remove mass from one shaft rather than half the amount of mass from both the X- and Y-shafts, although the improvement is a second-order effect. However, in practice there is not a choice. There is a limit in how much mass can be removed from a pump without compromising its structural integrity.

From a practical perspective, breaking the symmetry does not offer a feasible design solution at the linear level, although reducing the mass does. Note that the positive effect that removing mass has on the critical eccentricity bound is also apparent from the one degree-of-freedom critical eccentricity (2.36), and the rescaling formula for damping (2.25).

Note in practice that it is possible to substantially reduce the mass of the rotors by hollowing out both the X- and Y-rotors further than is standard. We calculate new critical eccentricities for booster pumps of types A, B and C with lightened rotors. These

Booster type	Standard $\varepsilon_{\text{crit}}$	Lightened rotors $\varepsilon_{\text{crit}}$	units
A	9.2×10^{-5}	1.1×10^{-4}	rads
B	6.5×10^{-5}	7.9×10^{-5}	rads
C	4.2×10^{-5}	5.0×10^{-5}	rads

Table 4.1. Critical eccentricity values for the booster pumps of types A, B and C with standard and lightened rotors, respectively.

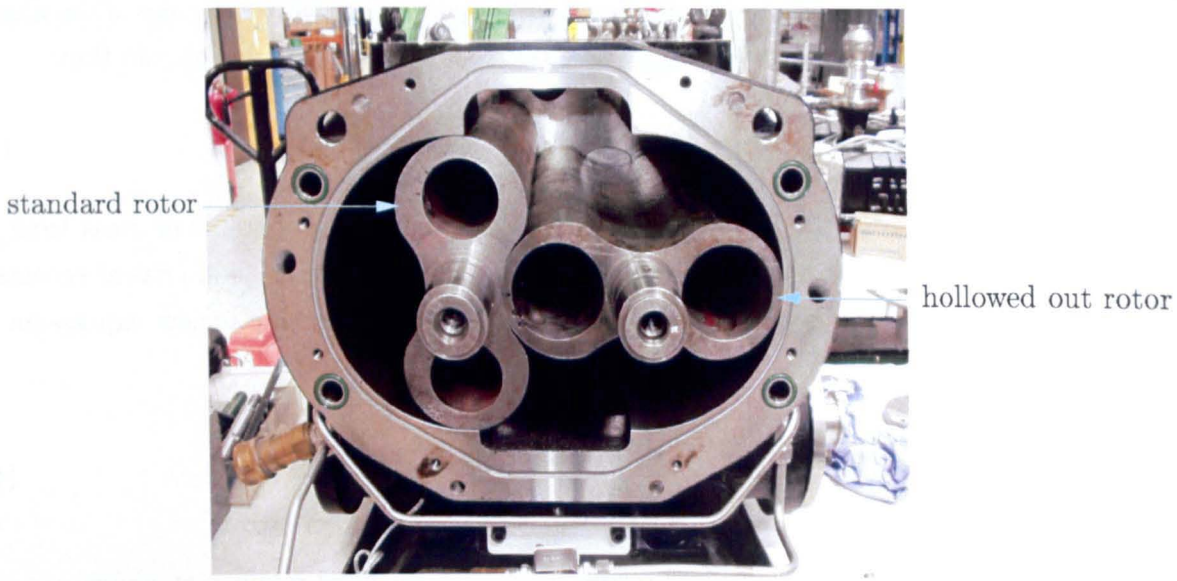

Figure 4.1. A photograph of the rotors of a Roots booster pump inside the pumping chamber. For comparison, the rotor on the left is a standard rotor, and the rotor on the right is a lightened rotor, which has been hollowed out further than usual.

values and the values for pumps with standard rotors, for comparison, are recorded in Table 4.1.

4.3 Symmetry-broken machine: rattling solutions

In the previous section we concluded that breaking the symmetry does not offer a feasible design solution in terms of the linear critical eccentricity bound. However, we are interested in whether breaking the symmetry can help fix the noise and vibration problem at the nonlinear level. Therefore, to complete our analysis of this model we now examine how the nonlinear rattling solutions are affected using simple $P(m,1,0)$ and $P(m,1,1)$ solutions as illustrative examples.

4.3.1 Freeplay solution component

Similarly to the one degree-of-freedom model, we shall only be concerned with the analysis of periodic rattling solutions in the infinite stiffness, impacting-contact model of backlash. Thus the only differential equation we need solve is equation (4.9) in the freeplay region, where $B(\Theta(t)+e(t))=0$ so that

$$\begin{pmatrix} \Theta' \\ \chi' \\ Z' \end{pmatrix} = \frac{1}{1-\eta^2}\begin{pmatrix} 0 & 1-\eta^2 & 0 \\ 0 & -\delta & \eta\delta \\ 0 & \eta\delta & -\delta \end{pmatrix}\begin{pmatrix} \Theta \\ \chi \\ Z \end{pmatrix} + \frac{\alpha}{1+\eta}\begin{pmatrix} 0 \\ 1 \\ 1 \end{pmatrix}. \tag{4.53}$$

In addition to the impact condition, governed by a simple restitution law (2.38), we also have the conservation of angular momentum at impacts which implies

$$(1+\eta)\Theta'_{\mathrm{X}}(t_{\mathrm{imp}}+)+(1-\eta)\Theta'_{\mathrm{Y}}(t_{\mathrm{imp}}+)=(1+\eta)\Theta'_{\mathrm{X}}(t_{\mathrm{imp}}-)+(1-\eta)\Theta'_{\mathrm{Y}}(t_{\mathrm{imp}}-), \tag{4.54}$$

where t_{imp} is the time of such an impact, and subscripts $(-)$ and $(+)$ denote values before and after impact, respectively. Equation (4.54) may be expressed in the form

$$Z(t_{\mathrm{imp}}+)=Z(t_{\mathrm{imp}}-)+2\eta v. \tag{4.55}$$

As a component part of our analysis, we construct the general solution of (4.53). From standard linear theory, the general solution of the linear ODE problem $\boldsymbol{x}'=\boldsymbol{A}\boldsymbol{x}$ is $\boldsymbol{x}=\sum c_i e^{\lambda_i t}\boldsymbol{e}_i$, where λ_i, $\boldsymbol{e}_i$ are the linearly independent eigenvalues and eigenvectors of $\boldsymbol{A}$ and arbitrary constants are denoted by c_i.

The eigenbasis $\{\lambda_i, \boldsymbol{e}_i\}$ of $\boldsymbol{A}$, where

$$\boldsymbol{A}=\frac{1}{1-\eta^2}\begin{pmatrix} 0 & 1-\eta^2 & 0 \\ 0 & -\delta & \eta\delta \\ 0 & \eta\delta & -\delta \end{pmatrix}, \tag{4.56}$$

can be computed as

$$\left\{0,\begin{pmatrix}1\\0\\0\end{pmatrix}\right\},\left\{-\frac{\delta}{1-\eta},\begin{pmatrix}1\\-\frac{\delta}{1-\eta}\\\frac{\delta}{1-\eta}\end{pmatrix}\right\},\left\{-\frac{\delta}{1+\eta},\begin{pmatrix}1\\-\frac{\delta}{1+\eta}\\-\frac{\delta}{1+\eta}\end{pmatrix}\right\}, \tag{4.57}$$

which we use to define a matrix $\boldsymbol{P}$,

$$\boldsymbol{P} := (e_1|e_2|e_3|) = \begin{pmatrix} 1 & 1 & 1 \\ 0 & -\frac{\delta}{1-\eta} & -\frac{\delta}{1+\eta} \\ 0 & \frac{\delta}{1-\eta} & -\frac{\delta}{1+\eta} \end{pmatrix}, \tag{4.58}$$

such that $\boldsymbol{A} = \boldsymbol{PDP}^{-1}$ where

$$\boldsymbol{D} := \mathrm{diag}\{\lambda_1, \lambda_2, \lambda_3\} = \begin{pmatrix} 0 & 0 & 0 \\ 0 & -\frac{\delta}{1-\eta} & 0 \\ 0 & 0 & -\frac{\delta}{1+\eta} \end{pmatrix}. \tag{4.59}$$

Hence equation (4.53) can be written in the form

$$\begin{pmatrix} \Theta' \\ \chi' \\ Z' \end{pmatrix} = \boldsymbol{PDP}^{-1} \begin{pmatrix} \Theta \\ \chi \\ Z \end{pmatrix} + \frac{\alpha}{1+\eta} \begin{pmatrix} 0 \\ 1 \\ 1 \end{pmatrix}. \tag{4.60}$$

We therefore write

$$\boldsymbol{u} = \boldsymbol{P}^{-1} \begin{pmatrix} \Theta \\ \chi \\ Z \end{pmatrix}, \tag{4.61}$$

which transforms equation (4.60) to

$$\boldsymbol{u}' = \boldsymbol{Du} + \frac{\alpha}{\delta} \begin{pmatrix} 1 \\ 0 \\ -1 \end{pmatrix}, \tag{4.62}$$

whose general solution is

$$\boldsymbol{u} = \underbrace{\frac{\alpha}{\delta} \begin{pmatrix} 1 \\ 0 \\ 0 \end{pmatrix} \left[e^{0t} \int_{t_0}^{t} e^{0s} \mathrm{d}s \right] + \frac{\alpha}{\delta} \begin{pmatrix} 0 \\ 0 \\ -1 \end{pmatrix} \left[e^{\frac{-\delta t}{1+\eta}} \int_{t_0}^{t} e^{\frac{\delta s}{1+\eta}} \mathrm{d}s \right]}_{\text{particular solution}}$$

$$+ \underbrace{\hat{c}_1 \begin{pmatrix} 1 \\ 0 \\ 0 \end{pmatrix} + \hat{c}_2 e^{\frac{-\delta t}{1-\eta}} \begin{pmatrix} 0 \\ 1 \\ 0 \end{pmatrix} + \hat{c}_3 e^{\frac{-\delta t}{1+\eta}} \begin{pmatrix} 0 \\ 0 \\ 1 \end{pmatrix}}_{\text{complementary function}}, \tag{4.63}$$

where $\hat{c}_1$, $\hat{c}_2$ and $\hat{c}_3$ are arbitrary constants. On calculating the integrals in the particular

solution, we obtain

$$\boldsymbol{u} = \frac{\alpha t}{\delta}\begin{pmatrix}1\\0\\0\end{pmatrix} - \frac{\alpha(1+\eta)}{\delta^2}\begin{pmatrix}0\\0\\1\end{pmatrix} + \widetilde{c}_1\begin{pmatrix}1\\0\\0\end{pmatrix} + c_2 e^{-\frac{\delta t}{1-\eta}}\begin{pmatrix}0\\1\\0\end{pmatrix} + c_3 e^{-\frac{\delta t}{1+\eta}}\begin{pmatrix}0\\0\\1\end{pmatrix}, \quad (4.64)$$

where $\widetilde{c}_1$, c_2 and c_3 are constants. We can then use (4.61) to write

$$\begin{pmatrix}\Theta\\ \chi\\ Z\end{pmatrix} = \boldsymbol{P}\boldsymbol{u}, \quad (4.65)$$

and hence read off the solutions for Θ, χ and Z,

$$\Theta = \frac{\alpha}{\delta}t + \left(\widetilde{c}_1 - \frac{\alpha(1+\eta)}{\delta^2}\right) + c_2 e^{-\frac{\delta t}{1-\eta}} + c_3 e^{-\frac{\delta t}{1+\eta}}, \quad (4.66)$$

$$\chi = \frac{\alpha}{\delta} - \frac{\delta}{1-\eta}c_2 e^{-\frac{\delta t}{1-\eta}} - \frac{\delta}{1+\eta}c_3 e^{-\frac{\delta t}{1+\eta}}, \quad (4.67)$$

$$Z = \frac{\alpha}{\delta} + \frac{\delta}{1-\eta}c_2 e^{-\frac{\delta t}{1-\eta}} - \frac{\delta}{1+\eta}c_3 e^{-\frac{\delta t}{1+\eta}}. \quad (4.68)$$

We typically work with $\Phi = \Theta + e(t)$ and $\Psi := \Phi'$ so that the solution is re-expressed in the form,

$$\Phi = \frac{\alpha}{\delta}t + \varepsilon\cos 2\pi t + c_1 + c_2 e^{-\frac{\delta t}{1-\eta}} + c_3 e^{-\frac{\delta t}{1+\eta}}, \quad (4.69)$$

$$\Psi = \frac{\alpha}{\delta} - 2\pi\varepsilon\sin 2\pi t - \frac{\delta}{1-\eta}c_2 e^{-\frac{\delta t}{1-\eta}} - \frac{\delta}{1+\eta}c_3 e^{-\frac{\delta t}{1+\eta}}, \quad (4.70)$$

$$Z = \frac{\alpha}{\delta} + \frac{\delta}{1-\eta}c_2 e^{-\frac{\delta t}{1-\eta}} - \frac{\delta}{1+\eta}c_3 e^{-\frac{\delta t}{1+\eta}}. \quad (4.71)$$

Having solved our system of differential equations in the freeplay regime, we shall now turn our attention to constructing two types of simple rattling periodic solution.

4.3.2 $P(m,1,0)$ solutions

Initially, we shall look at the simplest type of solution that oscillates between the freeplay region and the linear contact region (X drives Y). These solutions are of type $P(m,1,0)$, as they repeat every m periods of the forcing, impact the $\Phi = +\beta$ boundary once per

period and never contact the $\Phi = -\beta$ boundary, see Figure 2.11(a). This section is an extension of analysis carried out on the one degree-of-freedom model outlined in Section 2.4. The method is the same: we construct the coefficients of the general solution equations (4.69)–(4.71), found in Section 4.3.1, by enforcing periodicity and impact equations (2.38) and (4.55). For convenience we define

$$\lambda_- := \frac{\delta}{1-\eta}, \qquad \lambda_+ := \frac{\delta}{1+\eta}, \tag{4.72}$$

so that our equations (4.69)–(4.71) can be written in the neater form

$$\Phi(t) = \frac{\alpha t}{\delta} + \varepsilon\cos(2\pi t) + c_1 + c_2 e^{-\lambda_- t} + c_3 e^{-\lambda_+ t}, \tag{4.73}$$

$$\Psi(t) = \frac{\alpha}{\delta} - 2\pi\varepsilon\sin(2\pi t) - \lambda_- c_2 e^{-\lambda_- t} - \lambda_+ c_3 e^{-\lambda_+ t}, \tag{4.74}$$

$$Z(t) = \frac{\alpha}{\delta} + \lambda_- c_2 e^{-\lambda_- t} - \lambda_+ c_3 e^{-\lambda_+ t}. \tag{4.75}$$

With reference to Figure 2.11(a) our solution departs the $\Phi = +\beta$ boundary at some initial unknown time σ, with velocity $-v$. The periodicity and impact conditions then imply another impact of the $\Phi = +\beta$ boundary at some time $\sigma + m$ with velocity v. In addition to (2.42) and (2.43) (defined in Section 2.4) the conservation of angular momentum condition (4.55) implies that

$$Z(\sigma) = Z(\sigma + m) + 2\eta v. \tag{4.76}$$

Applying conditions (2.42), (2.43) and (4.76) to equations (4.73)–(4.75) we obtain a system in the form $\boldsymbol{A}\boldsymbol{c} = \boldsymbol{b}$ to solve for the five unknowns c_1, c_2, c_3, v and σ, where

$$\boldsymbol{A} = \begin{pmatrix} 1 & e^{-\lambda_-\sigma} & e^{-\lambda_+\sigma} & 0 \\ 1 & e^{-\lambda_-(\sigma+m)} & e^{-\lambda_+(\sigma+m)} & 0 \\ 0 & \lambda_- e^{-\lambda_-\sigma} & \lambda_+ e^{-\lambda_+\sigma} e_\sigma^- & 1 \\ 0 & \lambda_- e^{-\lambda_-(\sigma+m)} & \lambda_+ e^{-\lambda_+(\sigma+m)} & -1 \\ 0 & \lambda_-(e^{-\lambda_-(\sigma+m)} - e^{-\lambda_-\sigma}) & -\lambda_+(e^{-\lambda_+(\sigma+m)} - e^{-\lambda_+\sigma}) & -2\eta \end{pmatrix} \tag{4.77}$$

$$\boldsymbol{b} = \begin{pmatrix} \beta - 4\pi\sigma - \varepsilon\cos 2\pi\sigma \\ \beta - 4\pi(\sigma+m) - \varepsilon\cos 2\pi\sigma \\ -4\pi + 2\pi\varepsilon\sin 2\pi\sigma \\ -4\pi + 2\pi\varepsilon\sin 2\pi\sigma \\ 0 \end{pmatrix}, \tag{4.78}$$

$\boldsymbol{c} = [c_1\, c_2\, c_3\, v]^{\mathrm{T}}$, and $\lambda_\pm = \delta/(1 \pm \eta)$. We then find a matrix $\boldsymbol{P}$ with entries

$$P_{1,1} = \frac{1}{4}(2 - x - y), \quad P_{1,2} = \frac{1}{4}(2 + x - y), \quad P_{1,3} = -\frac{\eta}{4\delta}(x - y),$$
$$P_{1,4} = \frac{\eta}{4\delta}(x - y), \quad P_{1,5} = -\frac{1}{4\delta}(x - y), \quad P_{2,1} = \frac{e^{\lambda_- \sigma}}{2(1 - e^{-\lambda_- m})},$$
$$P_{2,2} = -\frac{e^{\lambda_- \sigma}}{2(1 - e^{-\lambda_- m})}, \quad P_{2,3} = \frac{\eta e^{\lambda_- \sigma}}{2\delta(1 - e^{-\lambda_- m})}, \quad P_{2,4} = -\frac{\eta e^{\lambda_- \sigma}}{2\delta(1 - e^{-\lambda_- m})},$$
$$P_{2,5} = \frac{e^{\lambda_- \sigma}}{2\delta(1 - e^{-\lambda_- m})}, \quad P_{3,1} = \frac{e^{\lambda_+ \sigma}}{2(1 - e^{-\lambda_+ m})}, \quad P_{3,2} = -\frac{e^{\lambda_+ \sigma}}{2(1 - e^{-\lambda_+ m})},$$
$$P_{3,3} = -\frac{\eta e^{\lambda_+ \sigma}}{2\delta(1 - e^{-\lambda_+ m})}, \quad P_{3,4} = -\frac{\eta e^{\lambda_+ \sigma}}{2\delta(1 - e^{-\lambda_+ m})}, \quad P_{3,5} = -\frac{e^{\lambda_+ \sigma}}{2\delta(1 - e^{-\lambda_+ m})},$$
$$P_{4,1} = \frac{\delta(2 - (1+\eta)x - (1-\eta)y)}{4(1-\eta^2)}, \quad P_{4,2} = \frac{-\delta(2 - (1+\eta)x - (1-\eta)y)}{4(1-\eta^2)},$$
$$P_{4,3} = \frac{-\eta(2\eta + (1+\eta)x - (1-\eta)y)}{4(1-\eta^2)}, \quad P_{4,4} = \frac{2\eta^2 - 4 + \eta(1+\eta)x - \eta(1-\eta)y}{4(1-\eta^2)},$$
$$P_{4,5} = \frac{2\eta - (1+\eta)x - \eta(1-\eta)y}{4(1-\eta^2)}, \quad P_{5,1} = \frac{\delta((1+\eta)x + (1-\eta)y)}{2},$$
$$P_{5,2} = \frac{-\delta((1+\eta)x + (1-\eta)y)}{2}, \quad P_{5,3} = \frac{2(1-\eta^2) + \eta((1+\eta)x - (1-\eta)y)}{2},$$
$$P_{5,4} = \frac{2(1-\eta^2) - \eta((1+\eta)x - (1-\eta)y)}{2}, \quad P_{5,5} = \frac{(1+\eta)x - (1-\eta)y}{2},$$

where

$$x := \coth\left(\frac{\lambda_- m}{2}\right), \qquad y := \coth\left(\frac{\lambda_+ m}{2}\right), \tag{4.79}$$

such that $\boldsymbol{PA}$ is in echelon form, which gives us expressions for c_1, c_2, c_3 and v, and generates an algebraic constraint on the impact time σ. If we premultiply b by $\boldsymbol{P}$ we can read off the solutions,

$$c_1 = \beta - \varepsilon\cos(2\pi\sigma) - \frac{\alpha\sigma}{\delta} - 2\pi m\frac{2 - e^{-\lambda_- m} - e^{-\lambda_+ m}}{(1 - e^{-\lambda_- m})(1 - e^{-\lambda_+ m})}, \tag{4.80}$$
$$c_2 = \frac{2\pi m e^{\lambda_- \sigma}}{1 - e^{-\lambda_- m}}, \tag{4.81}$$
$$c_3 = \frac{2\pi m e^{\lambda_+ \sigma}}{1 - e^{-\lambda_+ m}}, \tag{4.82}$$
$$v = \frac{2\pi\delta m}{1 - \eta^2}, \tag{4.83}$$
$$\sigma = \frac{1}{2\pi}\sin^{-1}\left[\frac{1}{\varepsilon}\left(2 - \frac{\lambda_- m}{2}\coth\left(\frac{\lambda_- m}{2}\right) - \frac{\lambda_+ m}{2}\coth\left(\frac{\lambda_+ m}{2}\right)\right)\right]. \tag{4.84}$$

4.3.3 Bounds for existence

Recall that in Section 2.4.4 we outlined two consistency checks that must be applied to $P(m,1,0)$ solutions for the one degree-of-freedom model. These must also be applied to the two degree-of-freedom model. We must therefore check that (i) the constructed solution never impacts the $\Phi = +\beta$ boundary, and (ii) the arcsin function in (4.84) lies between ± 1. To begin, we expand the two admissible solutions to (4.84) in terms of the small parameter δ to give:

$$\sigma = \begin{cases} \dfrac{-\delta^2 m^2(1+\eta^2)}{12\pi\varepsilon(1-\eta^2)^2} + O(\delta^4): & \text{in-phase solution,} \\ \dfrac{1}{2} + \dfrac{\delta^2 m^2(1+\eta^2)}{12\pi\varepsilon(1-\eta^2)^2} + O(\delta^4): & \text{out-of-phase solution.} \end{cases} \tag{4.85}$$

As before, numerical evidence indicates that the in-phase solution is stable, and the out-of-phase solution is unstable. We must also make two consistency checks on the $P(m,1,0)$ solutions: that the arcsin function of (4.84) does not exceed one in modulus; and that the solution never crosses the $\Phi = -\beta$ boundary.

If we expand the argument of the arcsin function in (4.84) in terms of the small parameter δ we find that

$$\begin{aligned} &\frac{1}{\varepsilon}\left(2 - \frac{\delta m}{2(1-\eta)}\coth\left(\frac{\delta m}{2(1-\eta)}\right) - \frac{\delta m}{2(1+\eta)}\coth\left(\frac{\delta m}{2(1+\eta)}\right)\right) \\ &= -\frac{\delta^2 m^2(1+\eta^2)}{6\varepsilon(1-\eta^2)} + O(\delta^3). \end{aligned} \tag{4.86}$$

Therefore for the existence of simple $P(m,1,0)$ solutions we require to leading order that

$$\varepsilon > \frac{\delta^2 m^2(1+\eta^2)}{6(1-\eta^2)} + O(\delta^4), \tag{4.87}$$

$$\sim \frac{\delta^2 m^2}{6}\left(1 + 2\eta^2 + O(\eta^4)\right), \tag{4.88}$$

is satisfied. We now consider whether our trajectory has the correct itinerary, i.e., that it will not impact the boundary at $\Phi = -\beta$. To determine this we must first find the minimum displacement. Our complete solution for Φ is

$$\begin{aligned} \Phi(t) = \frac{\alpha}{\delta}(t-\sigma) + \beta + \varepsilon[\cos(2\pi t) - \cos(2\pi\sigma)] \\ + 2\pi m\left(\frac{\exp\left(\dfrac{-\delta(t-\sigma)}{1-\eta}\right) - 1}{1 - \exp\left(\dfrac{-\delta m}{1-\eta}\right)} + \frac{\exp\left(\dfrac{-\delta(t-\sigma)}{1+\eta}\right) - 1}{1 - \exp\left(\dfrac{-\delta m}{1+\eta}\right)}\right), \end{aligned} \tag{4.89}$$

where we assume $\sigma = O(\delta, \varepsilon)$. If we take $\alpha = 4\pi\delta$, then after differentiation we have

$$\Psi(t) = 4\pi - 2\pi\varepsilon\sin(2\pi t) - 2\pi\delta m\left(\frac{\exp\left(\frac{-\delta(t-\sigma)}{1-\eta}\right)}{(1-\eta)\left(1-\exp\left(\frac{-\delta m}{1-\eta}\right)\right)} + \frac{\exp\left(\frac{-\delta(t-\sigma)}{1+\eta}\right)}{(1+\eta)\left(1-\exp\left(\frac{-\delta m}{1+\eta}\right)\right)}\right). \quad (4.90)$$

To find the minimum displacement we first find the point at which the velocity is zero, i.e., $\hat{t}$ such that $\Psi(\hat{t}) = 0$. We try a power series approximation to this time

$$\hat{t} = \sigma + \frac{m}{2} + \hat{t}_0 + \hat{t}_1\delta + O(\delta^2). \quad (4.91)$$

We have four cases corresponding to in-phase/out-of-phase and m odd/even. We solve for the coefficients t_i in each case. For all cases $\hat{t}_0 = 0$. For the in-phase solution ($\sigma \approx 0$) we find

$$\hat{t}_1 = \begin{cases} \dfrac{m^2\delta(1+\eta^2)}{24(\pi\varepsilon\eta^4 - \delta\eta^2 - 2\pi\varepsilon\eta^2 + \delta + \pi\varepsilon)} & : \quad m \text{ even}, \\ \dfrac{m^2\delta(1+\eta^2)}{8(\pi\varepsilon\eta^4 + \delta\eta^2 - 2\pi\varepsilon\eta^2 - \delta + \pi\varepsilon)} & : \quad m \text{ odd}, \end{cases} \quad (4.92)$$

and for the out-of-phase solution ($\sigma \approx \frac{1}{2}$) we find

$$\hat{t}_1 = \begin{cases} -\dfrac{m^2\delta(1+\eta^2)}{24(\pi\varepsilon\eta^4 + \delta\eta^2 - 2\pi\varepsilon\eta^2 - \delta + \pi\varepsilon)} & : \quad m \text{ even}, \\ -\dfrac{m^2\delta(1+\eta^2)}{8(\pi\varepsilon\eta^4 - \delta\eta^2 - 2\pi\varepsilon\eta^2 + \delta + \pi\varepsilon)} & : \quad m \text{ odd}. \end{cases} \quad (4.93)$$

We then substitute these series expressions for $\hat{t}$ into our ODE solution for Φ, equation (4.89), and expand this as a series also. For the in-phase solution ($\sigma \approx 0$) not to contact the lower boundary we require $\Phi > -\beta$, which gives

$$\beta > \begin{cases} \dfrac{\pi m^2\delta}{4(1-\eta^2)} + \varepsilon + O(\delta^2) & : \quad m \text{ even}, \\ \dfrac{\pi m^2\delta}{4(1-\eta^2)} + O(\delta^2) & : \quad m \text{ odd}, \end{cases} \quad (4.94)$$

and for the out-of-phase solution ($\sigma \approx 1/2$) not to contact the lower boundary we require

$$\beta > \begin{cases} \dfrac{\pi m^2\delta}{4(1-\eta^2)} - \varepsilon + O(\delta^2) & : \quad m \text{ even}, \\ \dfrac{\pi m^2\delta}{4(1-\eta^2)} + O(\delta^2) & : \quad m \text{ odd}. \end{cases} \quad (4.95)$$

Note that when $\eta = 0$ (symmetric machine), we recover the bounds for the one degree-

of-freedom model illustrated in Figure 2.13. We observe that the bounds for both the in-phase and out-of-phase solution to graze $\Phi = -\beta$ are increased when η is varied. This implies that the region in parameter space where less noisy $P(m,1,0)$ solutions exist is increased, possibly at the expense of noisy solutions. However, this is only a higher-order improvement.

The most important bound to increase, in terms of quiet pump operation, is the bound on ε for existence of $P(m,1,0)$ solutions (4.88). If we move below this bound we can destroy this type of solution. We observe that breaking the symmetry does increase this bound, but the $\varepsilon \sim O(\delta^2)$ scaling remains unchanged. Unfortunately we find that this is also true for removing mass from one shaft, or from both shafts, i.e., varying μ or ν. With reference to Section 4.2 we substitute for μ using (4.33). Hence (4.88) becomes

$$\varepsilon > \frac{\delta^2 m^2}{6(1+2\mu)}\left(1+\frac{\mu^2}{(1+\mu)^2}\right), \tag{4.96}$$

$$\sim \frac{\delta^2 m^2}{6}\left(1-2\mu+O(\mu^2)\right). \tag{4.97}$$

Similarly, we can substitute for ν using (4.50). Hence (2.54) becomes

$$\varepsilon > \frac{\delta^2 m^2}{6}\left(\frac{1}{(1+\nu)^2}\right), \tag{4.98}$$

$$\sim \frac{\delta^2 m^2}{6}\left(1-2\nu+O(\nu^2)\right). \tag{4.99}$$

We conclude that breaking the symmetry of the pump or removing mass increases the upper bound on ε, below which $P(m,1,0)$ solutions are destroyed. However in practical machines ε and δ are of similar magnitude so the improvement in the dynamics of the symmetry-broken machine is only a marginal effect. In particular, the birth of $P(m,1,0)$ solutions is still $\varepsilon \sim O(\delta^2)$, and so these cannot be removed in practice.

4.3.4 $P(m,1,1)$ solutions

Finally, we show how to construct the noisier, less desirable, $P(1,1,1)$ solutions that correspond to solutions that visit all three regimes, thus impacting both $\Phi = \pm\beta$ boundaries. These solutions correspond to the gears leaving contact, entering freeplay, then re-establishing contact in torque reversal. The broad approach is to use the general solution found in Section 4.3.1, given by equations (4.69)–(4.71), and then apply impact and periodicity conditions, as well as the conservation of momentum. With reference

to Figure 2.11(b) our solution is made up of two segments where

$$\Phi^{\mathrm{A,B}}(t) = \frac{\alpha t}{\delta} + \varepsilon\cos(2\pi t) + c_1^{\mathrm{A,B}} + c_2^{\mathrm{A,B}} e^{-\lambda_- t} + c_3^{\mathrm{A,B}} e^{-\lambda_+ t}, \tag{4.100}$$

$$\Psi^{\mathrm{A,B}}(t) = \frac{\alpha}{\delta} - 2\pi\varepsilon\sin(2\pi t) - \lambda_- c_2^{\mathrm{A,B}} e^{-\lambda_- t} - \lambda_+ c_3^{\mathrm{A,B}} e^{-\lambda_+ t}, \tag{4.101}$$

$$z^{\mathrm{A,B}}(t) = \frac{\alpha}{\delta} + \lambda_- c_2^{\mathrm{A,B}} e^{-\lambda_- t} - \lambda_+ c_3^{\mathrm{A,B}} e^{-\lambda_+ t}. \tag{4.102}$$

The solution departs the $\Phi = +\beta$ boundary at some initial unknown time σ_{A}, with velocity $-v_{\mathrm{A}}$. This is followed by an impact with the $\Phi = -\beta$ boundary at σ_{B} with velocity $-v_{\mathrm{B}}$ before the solution re-impacts the $\Phi = \beta$ boundary with velocity $-v_{\mathrm{B}}$. In addition to equations (2.48)–(2.51) (defined in Section 2.4.2) the conservation of angular momentum (see (4.55)) then implies that the conditions

$$Z^{\mathrm{A}}(\sigma_{\mathrm{A}}) + \eta\Psi^{\mathrm{A}}(\sigma_{\mathrm{A}}) = Z^{\mathrm{B}}(\sigma_{\mathrm{A}+1}) + \eta\Psi^{\mathrm{B}}(\sigma_{\mathrm{A}+1}), \tag{4.103}$$

$$Z^{\mathrm{A}}(\sigma_{\mathrm{B}}) + \eta\Psi^{\mathrm{A}}(\sigma_{\mathrm{B}}) = Z^{\mathrm{B}}(\sigma_{\mathrm{B}}) + \eta\Psi^{\mathrm{B}}(\sigma_{\mathrm{B}}), \tag{4.104}$$

must be met. Applying conditions (2.48)–(2.51), (4.103) and (4.104) to equations (4.100)–(4.102) we obtain a system in the form $\boldsymbol{A}\boldsymbol{c} = \boldsymbol{b}$ to solve for the ten unknowns c_1^{A}, c_1^{B}, c_2^{A}, c_2^{B}, c_3^{A}, c_3^{B}, v_{A}, v_{B}, σ_{A}, σ_{B}. We find that the expressions for $\sigma_{\mathrm{A,B}}$ are not solvable in closed form, it is necessary to resort to a numerical root-finding procedure to find the impact times. Once the solutions have been found, as for the $P(m,1,0)$ solutions, a retrospective check has to be made to ensure that the constructed solution is always in the correct regime. The aim would then be to find conditions on the symmetry-breaking parameter η, to determine how this noisy type of solution can be destroyed and replaced by quieter single-contact solutions. However, there is no evidence to suggest at this point that a symmetry-broken machine will be superior in this respect.

4.4 Sprung-gear system

The remainder of this chapter is devoted to a sketch calculation for the 'sprung-gear' design solution proposed by BOCE [10], for which a patent has been applied [12].

The idea behind the sprung-gear system is to isolate the driving gear (X) from the X-shaft. The proposed design solution is to mount the driving gear (X) on the X-shaft by means of a torsional spring, of a much lower stiffness to that of the shaft assembly. As before, the only interaction between the X- and Y-shaft assemblies is through the gears, but now the X ('sprung') gear and the X-shaft are treated as separate entities. Figure 4.2 is a diagram of the proposed set-up: torsional springs are sandwiched between the

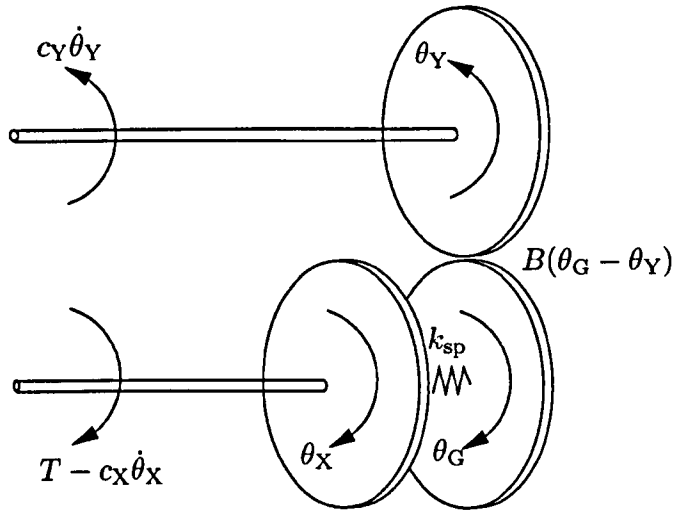

Figure 4.2. Diagram of the proposed sprung-gear assembly. The driving gear is mounted on the X-shaft by means of a torsional spring, of stiffness k_{sp}, attached to a mounting assembly, which is mounted on the shaft. Note that the interaction force is now measured between θ_Y and θ_G. For the purposes of visualisation we have not shown the rotors.

driving gear and a mounting assembly, and the mounting assembly is attached rigidly to the X-shaft. For the purposes of visualisation, only one torsional spring has been illustrated. In practice, the proposed design solution incorporates six springs, as shown in the photograph in Figure 4.3.

4.4.1 Equations of motion

We apply Newton's second law of motion in angular co-ordinates to derive the equations of motion for the sprung-gear system. For the X-shaft assembly we have

$$I_X\ddot{\theta}_X = T(\tau) - c_X\dot{\theta}_x - k_{sp}(\theta_X - \theta_G) - c_{sp}(\dot{\theta}_X - \dot{\theta_G}), \tag{4.105}$$

for the sprung-gear assembly we have

$$I_G\ddot{\theta}_G = -k_{sp}(\theta_G - \theta_X) - kB(\theta_G - \theta_Y + e(\tau)) - c_{sp}(\dot{\theta}_G - \dot{\theta_X}), \tag{4.106}$$

and for the Y-shaft assembly, we have

$$I_Y\ddot{\theta}_Y = -c_Y\dot{\theta}_y + kB(\theta_G - \theta_Y + e(\tau)), \tag{4.107}$$

where dots denote differentiation with respect to time τ. In addition to the terms that we had for the one degree-of-freedom model, we have θ_G, which measures the angular

Figure 4.3. A photograph of the proposed sprung-gear set-up. The X-gear and mounting assembly is shown on the left, and the springs are overlaid in cyan.

displacement of the X-gear, I_{G} the inertia of the X-gear, k_{sp} the torsional spring stiffness and c_{sp} the spring damping. Parameter values for I_{G}, k_{sp} and c_{sp} have been provided by BOCE [10]. We note that the gear interaction force kB is now measured between the X-gear θ_{G} and the Y-shaft assembly θ_{Y}. $\theta_{\mathrm{G}} - \theta_{\mathrm{Y}} + e(\tau)$ is therefore the new relative rotational displacement of the gears, where $e(\tau)$ represents the oscillatory correction term for eccentricity, derived in Section 2.1.

4.4.2 Non-dimensionalisation

As for the one degree-of-freedom model, we assume that the moments of inertia and the damping coefficients of the two shaft assemblies are equal, namely that $I_{\mathrm{X}} = I_{\mathrm{Y}} =: I$ and $c_{\mathrm{X}} = c_{\mathrm{Y}} =: c$. In addition, we neglect the spring damping terms since we expect the difference in velocities of the driving gear and the X-shaft will be negligible. If we incorporate these assumptions, and non-dimensionalise, we are are able to recast equations (4.105)–(4.107) in the form

$$\theta''_{\mathrm{X}} = \alpha - \delta_{\mathrm{X}}\theta'_{\mathrm{X}} - \kappa_{\mathrm{sp}}(\theta_{\mathrm{X}} - \theta_{\mathrm{G}}), \tag{4.108}$$

$$\eta_{\mathrm{G}}\theta''_{\mathrm{G}} = -\kappa_{\mathrm{sp}}(\theta_{\mathrm{G}} - \theta_{\mathrm{X}}) - \kappa B(\theta_{\mathrm{G}} - \theta_{\mathrm{Y}} + e(t)), \tag{4.109}$$

$$\theta''_{\mathrm{Y}} = -\delta_{\mathrm{Y}}\theta'_{\mathrm{Y}} + \kappa B(\theta_{\mathrm{G}} - \theta_{\mathrm{Y}} + e(t)). \tag{4.110}$$

Quantity	symbol	value
Gear wheel spring torsional stiffness	κ_{sp}	3.33
Gear wheel to shaft assembly inertia ratio	η_{G}	0.06

Table 4.2. New non-dimensional parameters for the sprung-gear model. See Table 2.1 for the other non-dimensional parameters.

Here dashes denote differentiation with respect to non-dimensional time t, and

$$t = \Omega\tau, \quad \delta = \frac{c}{\Omega I}, \quad \kappa = \frac{rk}{\Omega^2 I}, \quad \kappa_{\text{sp}} = \frac{k_{\text{sp}}}{\Omega^2 I}, \quad \eta_{\text{G}} = \frac{I_{\text{G}}}{I}, \quad \varepsilon = \frac{E}{r}, \quad \alpha = \frac{\overline{T}}{\Omega^2 I} = 4\pi\delta. \tag{4.111}$$

All the terms are defined as for the one degree-of-freedom model (see Table 2.1) apart from the extra non-dimensional parameters κ_{sp} (the non-dimensional torsional spring stiffness) and η_{G} (the ratio of the sprung-gear inertia to either the X- or Y-shaft assembly inertia), see Table 4.2.

It is possible to re-write equations (4.108)–(4.110) as a system of five first-order equations by introducing new co-ordinates, ($\theta_{\text{X,G}}$, $\theta_{\text{G,Y}}$, $\chi_{\text{X,G}}$, $\chi_{\text{G,Y}}$, Z), defined by

$$\theta_{\text{X,G}} = \theta_{\text{X}} - \theta_{\text{G}}, \tag{4.112}$$

$$\theta_{\text{G,Y}} = \theta_{\text{G}} - \theta_{\text{Y}}, \tag{4.113}$$

$$\chi_{\text{X,G}} = \theta'_{\text{X}} - \theta'_{\text{G}}, \tag{4.114}$$

$$\chi_{\text{G,Y}} = \theta'_{\text{G}} - \theta'_{\text{Y}}, \tag{4.115}$$

$$Z = \theta'_{\text{X}} + \theta'_{\text{Y}}, \tag{4.116}$$

where $\theta_{\text{G,Y}}$ is the relative rotational displacement, $\theta_{\text{X,G}}$ measures how far the spring is deflected and Z is approximately the total angular momentum (since in practice the inertia of the gear is small).

4.4.3 Permanent linear contact solutions

We now focus on calculating the critical eccentricity. Our aim is to determine how this bound is affected by the addition of the sprung-gear. We must first calculate the explicit solutions of the equations of motion (4.108)–(4.109) in the linear contact regime. The simplest method of solving these equations is in matrix form in terms of the new co-ordinates defined in equations (4.112)–(4.116). In permanent linear contact (PLC), X

drives Y, so we can substitute $B(\theta_G - \theta_Y + e(t)) = \theta_G - \theta_Y + e(t) - \beta$, which yields

$$\underbrace{\begin{pmatrix} \frac{1}{2} & \frac{1}{2} & \frac{1}{2} & 0 & 0 \\ -\frac{\eta_G}{2} & \frac{\eta_G}{2} & \frac{\eta_G}{2} & 0 & 0 \\ -\frac{1}{2} & -\frac{1}{2} & \frac{1}{2} & 0 & 0 \\ 0 & 0 & 0 & 1 & 0 \\ 0 & 0 & 0 & 0 & 1 \end{pmatrix}}_{M} \frac{\mathrm{d}}{\mathrm{d}t} \begin{pmatrix} \chi_{X,G} \\ \chi_{G,Y} \\ Z \\ \theta_{X,G} \\ \theta_{G,Y} \end{pmatrix}$$

$$= \underbrace{\begin{pmatrix} -\frac{\delta}{2} & -\frac{\delta}{2} & -\frac{\delta}{2} & -\kappa_{sp} & 0 \\ 0 & 0 & 0 & \kappa_{sp} & -\kappa \\ \frac{\delta}{2} & \frac{\delta}{2} & -\frac{\delta}{2} & 0 & \kappa \\ 1 & 0 & 0 & 0 & 0 \\ 0 & 1 & 0 & 0 & 0 \end{pmatrix}}_{A} \begin{pmatrix} \chi_{X,G} \\ \chi_{G,Y} \\ Z \\ \theta_{X,G} \\ \theta_{G,Y} \end{pmatrix} + \underbrace{\begin{pmatrix} \alpha \\ \kappa\beta \\ -\kappa\beta \\ 0 \\ 0 \end{pmatrix}}_{b_1} + \begin{pmatrix} 0 \\ -\kappa e(t) \\ \kappa e(t) \\ 0 \\ 0 \end{pmatrix}. \quad (4.117)$$

Note for ease of calculation, we have made $\theta_{G,Y}$ the fifth component of $\boldsymbol{u}$, since this is the term that represents the relative rotational displacement. Similarly to the one degree-of-freedom model, the eccentricity term can be written as

$$e(t) = \Re\{\varepsilon \exp 2\pi t\mathrm{i}\}, \quad (4.118)$$

where $\Re$ denotes the real part, and i is the square root of -1. If we write

$$b_2 = \begin{pmatrix} 0 \\ \kappa\varepsilon \\ -\kappa\varepsilon \\ 0 \\ 0 \end{pmatrix}, \quad (4.119)$$

then equation (4.117) can be expressed in matrix form:

$$\boldsymbol{M}\boldsymbol{u}' = \boldsymbol{A}\boldsymbol{u} + b_1 - \Re\{b_2 \exp 2\pi t\mathrm{i}\}. \quad (4.120)$$

Using standard techniques, we can substitute a particular solution of the form

$$\boldsymbol{u} = \boldsymbol{c}_1 + \Re\{\boldsymbol{c}_2 \exp 2\pi t\mathrm{i}\}, \quad (4.121)$$

and compare coefficients to obtain expressions for $\boldsymbol{c_1}$ and $\boldsymbol{c_2}$,

$$\boldsymbol{c}_1 = -\boldsymbol{A}^{-1}\boldsymbol{b}_1, \tag{4.122}$$

$$\boldsymbol{c}_2 = (\boldsymbol{A} - 2\pi i\boldsymbol{M})^{-1}\boldsymbol{b}_2. \tag{4.123}$$

For existence, we require that the relative rotational displacement must satisfy

$$(\theta_{\mathrm{G}}(t) - \theta_{\mathrm{Y}}(t) + e(t)) > \beta \quad \text{for all } t. \tag{4.124}$$

Since $\theta_{\mathrm{G,Y}}$ is the fifth component of $\boldsymbol{u}$, we have

$$\theta_{\mathrm{G,Y}} + e(t) = \Re\{(c_{1,5} + (c_{2,5} + \varepsilon)\exp 2\pi t i)\}, \tag{4.125}$$

where $c_{1,5}$ and $c_{2,5}$ are the fifth components of $\mathbf{c_1}$ and $\mathbf{c_2}$, respectively given by

$$c_{1,5} = \frac{\alpha}{2\kappa} + \beta, \tag{4.126}$$

$$c_{2,5} = \frac{\kappa\varepsilon\left(1 + \frac{\eta_{\mathrm{G}}\pi i}{\delta+2\pi\mathrm{i}} + \frac{1}{\kappa_{\mathrm{sp}}+2\pi\mathrm{i}(\delta+2\pi\mathrm{i})}\left(\kappa_{\mathrm{sp}} - 2\eta_{\mathrm{g}}\pi^2 + \frac{\kappa_{\mathrm{sp}}\eta_{\mathrm{G}}\pi\mathrm{i}}{\delta+2\pi\mathrm{i}}\right)\right)}{-\kappa + 2\eta_{\mathrm{G}}\pi^2 - \frac{\kappa\eta_{\mathrm{G}}\pi\mathrm{i}}{\delta+2\pi\mathrm{i}} - \frac{\kappa+2\pi\mathrm{i}(\delta+2\pi\mathrm{i})}{\kappa_{\mathrm{sp}}+2\pi\mathrm{i}(\delta+2\pi\mathrm{i})}\left(\kappa_{\mathrm{sp}} - 2\eta_{\mathrm{G}}\pi^2 + \frac{\kappa_{\mathrm{sp}}\eta_{\mathrm{G}}\pi\mathrm{i}}{\delta+2\pi\mathrm{i}}\right)}. \tag{4.127}$$

The minimum displacement of $\theta_{\mathrm{G,Y}}$ is given by

$$c_{1,5} - |c_{2,5} + \varepsilon|. \tag{4.128}$$

For condition (4.124) to be fulfilled we require

$$c_{1,5} - |c_{2,5} + \varepsilon| > \beta. \tag{4.129}$$

If we use (4.126) to substitute for $c_{2,5}$ we obtain

$$\frac{\alpha}{2\kappa} > |c_{2,5} + \varepsilon|. \tag{4.130}$$

Noting that $c_{2,5}$ is a multiple of ε, we have

$$\varepsilon\left(\frac{c_{2,5}}{\varepsilon} + 1\right) = \frac{\varepsilon\left(\frac{2\eta_{\mathrm{G}}\pi^2}{\kappa} - \frac{2\pi i(\delta + 2\pi i)}{\kappa(\kappa_{\mathrm{sp}} + 2\pi i(\delta + 2\pi i))}\left(\kappa_{\mathrm{sp}} - 2\eta_{\mathrm{G}}\pi^2 + \frac{\kappa_{\mathrm{sp}}\eta_{\mathrm{G}}\pi i}{\delta + 2\pi i}\right)\right)}{-1 + \frac{2\eta_{\mathrm{G}}\pi^2}{\kappa} - \frac{\eta_{\mathrm{G}}\pi i}{\delta + 2\pi i} - \frac{\kappa + 2\pi i(\delta + 2\pi i)}{\kappa(\kappa_{\mathrm{sp}} + 2\pi i(\delta + 2\pi i))}\left(\kappa_{\mathrm{sp}} - 2\eta_{\mathrm{G}}\pi^2 + \frac{\kappa_{\mathrm{sp}}\eta_{\mathrm{G}}\pi i}{\delta + 2\pi i}\right)}. \tag{4.131}$$

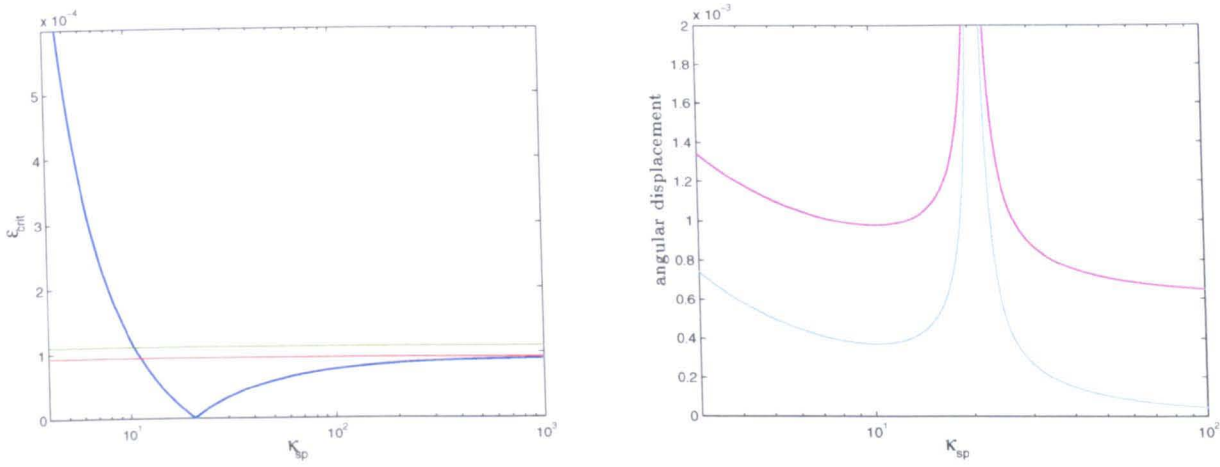

Figure 4.4. (a) The critical eccentricity bounds for the one degree-of-freedom model (for standard and lightened rotors) and the three degree-of-freedom model, shown in red, green and blue, respectively. (b) The angular displacements $\theta_{\mathrm{X,G}}$ (cyan) and $\theta_{\mathrm{X,Y}}$ (magenta) as a function of the torsional spring stiffness κ_{sp}. Note that the range of spring stiffnesses κ_{sp} that we wish to examine is very large, therefore, in both graphs, for the purposes of visualisation we have taken the log of values on the x-axis.

The bound on ε is thus

$$\varepsilon \;<\; \frac{\alpha}{2\kappa\left|\frac{c_{2,5}}{\varepsilon}+1\right|}. \tag{4.132}$$

We can use (4.132) to find $\varepsilon_{\mathrm{crit}}^{3\ \mathrm{d.o.f.}}$ such that $\varepsilon < \varepsilon_{\mathrm{crit}}^{3\ \mathrm{d.o.f.}}$ is a necessary and sufficient condition for the existence of PLC solutions in the sprung-gear system. If we expand (4.132) in small δ and η_{G}, we find

$$\varepsilon_{\mathrm{crit}}^{3\ \mathrm{d.o.f.}} = \frac{\delta}{\pi\kappa\sqrt{\kappa_{\mathrm{sp}}^2}}\sqrt{(-2\kappa_{\mathrm{sp}}\pi^2+\kappa\kappa_{\mathrm{sp}}-2\kappa\pi^2)^2}\left(1-\frac{\eta_{\mathrm{G}}\kappa(\kappa_{\mathrm{sp}}^2-8\kappa_{\mathrm{sp}}\pi^2+16\pi^4)}{2\kappa_{\mathrm{sp}}(-2\kappa_{\mathrm{sp}}\pi^2+\kappa\kappa_{\mathrm{sp}}-2\kappa\pi^2)}\right) + O(\delta^3)+O(\eta_{\mathrm{G}}^3). \tag{4.133}$$

4.4.4 Commentary on the critical eccentricity

If we use the parameter values from Tables 2.1 and 4.2 in formula (4.133) we find that $\varepsilon_{\mathrm{crit}}^{3\ \mathrm{d.o.f.}} = 1.44\times10^{-3}$ (an improvement of approximately 1500% on the un-sprung system). More generally, we can plot (4.133) for different torsional spring stiffness κ_{sp} values, see Figure 4.4(a). For comparison we have overlaid the critical eccentricity of the one degree-of-freedom model for standard and lightened rotors. As $\kappa_{\mathrm{sp}}\to\infty$, $\varepsilon_{\mathrm{crit}}^{3\ \mathrm{d.o.f.}}$ tends towards $\varepsilon_{\mathrm{crit}}^{1\ \mathrm{d.o.f.}}$, as if the sprung-gear were absent. This can also be observed if

we let $\kappa_{\rm sp} \to \infty$ in (4.133),

$$\lim_{\kappa_{\rm sp}\to\infty} \varepsilon_{\rm crit} = \frac{2\delta}{\kappa}\sqrt{\frac{(\kappa-2\pi^2)^2+\pi^2\delta^2}{4\pi^2+\delta^2}} + O(\eta_{\rm G}), \tag{4.134}$$

to recover equation (2.36). Alternatively, if we let $\kappa \to \infty$ and choose the sign of the root in (4.133) so that the critical eccentricity is positive for $\kappa_{\rm sp} < 2\pi^2$, (4.133) becomes

$$\varepsilon_{\rm crit} \sim \frac{\delta}{\pi}\frac{(2\pi^2-\kappa_{\rm sp})}{\kappa_{\rm sp}}\left(1-\frac{(\kappa_{\rm sp}-4\pi^2)^2\eta_{\rm G}}{2\kappa_{\rm sp}(\kappa_{\rm sp}-2\pi^2)}\right) + O(\delta^2) + O(\eta_{\rm G}^2). \tag{4.135}$$

We note that if $\kappa_{\rm sp} = 2\pi^2$, then the $O(\eta_G)$ term becomes singular. This is also a feature of Figure 4.4(a), where there is a minimum at $\kappa_{\rm sp} = 2\pi^2$, and corresponds to resonance with the gross rotation (recall we have neglected the spring damping). We observe that for values of $\kappa_{\rm sp} <\approx 12$, the addition of the sprung-gear offers an improvement in the critical eccentricity over the one degree-of-freedom model, as predicted by (4.135). In addition, we plot the maximum angular displacement $\theta_{\rm X,G}$ as a function of the torsional spring stiffness $\kappa_{\rm sp}$ in Figure 4.4(b). This is to check how far the spring in the mounting assembly slot is deflected. We have also plotted the relative angular displacement $(\theta_{\rm X,Y} + e(t))$ against the torsional spring stiffness (in magenta) to ensure that the gears do not clash. The minimum/maxima at $\kappa_{\rm sp} \approx 20$ in all the figures corresponds to resonance with the gross rotation.

4.5 Discussion

In this chapter we have considered two proposed design solutions for reducing gear rattle in Roots booster pumps. We have extended the work carried out by Halse *et al.* [23, 24], by constructing full two and three degree-of-freedom models to investigate the effects of breaking the symmetry between the two shafts and the addition of a sprung-gear.

The results have been mixed. In the case of the two degree-of-freedom model, we discovered that removing mass from the machine increases (improves) the critical value of eccentricity (below which silent solutions exist), whilst adding mass reduces this existence bound. In addition, removing mass also increases the bound below which simple $P(m,1,0)$ rattling solutions are destroyed, but unfortunately does not break the $\varepsilon \sim O(\delta^2)$ scaling. We also compared the relative merits of

(a) removing mass from one shaft and adding it to the other,

(b) removing mass from both shafts,

(c) removing mass from just one shaft.

We found that reducing the mass of the pump (cases (b) and (c)) is preferable to keeping the mass of the pump constant (case (a)). In addition, removing mass from one shaft, in comparison to removing the same amount of mass from both shafts, offers the largest increase of both the critical eccentricity and $P(m, 1, 0)$ solution bounds. However, one is very limited in how much mass can be removed from a pump, without compromising its structural integrity, and in practice it is best to remove as much mass as is possible from both shaft assemblies. This design change has been implemented by BOCE by hollowing out the centres of the rotors further than they did previously.

In the case of the sprung-gear, our results are inconclusive. Linear calculations indicate that the addition of the sprung-gear has a marked increase on the critical eccentricity. However, to complete the analysis, we would wish to investigate the full nonlinear problem. Since the nonlinear solutions will be difficult to solve analytically, it will be necessary to solve the initial value problem numerically, and we defer this to future work.

Chapter 5

Centrifugal Pendulum Vibration Absorbers

5.1 Background

Centrifugal pendulum vibration absorbers (CPVAs) are a type of passive tuned vibration absorber, which can reduce torsional vibrations in rotating machines [54]. CPVAs are designed to suppress *order vibrations* whose frequency is proportional to the rotation speed, unlike vibration dampers which are tuned to a specific frequency. The absorbers employed in CPVAs are effectively masses mounted on pendulums, and are tuned by specifying the length of the pendulum (r_2) compared to the distance between the system's axis of rotation and the pivot of the pendulum (r_1), see Figure 5.1(a). An alternative configuration involves mounting absorbers on a disc, where spherical masses are constrained to move along (typically circular) grooves cut into the disc, see Figure 5.1(b).

Traditionally, the absorbers are designed according to linear theory, which is satisfactory provided that the amplitudes of motion are small. For a perfect vibration absorber mounted on a concentric disc, it can be shown that $n^2 = r_1/r_2$, for small angular displacements of the absorber ϕ_0, where n is the order of the applied torque. For this tuning with an absorber of mass m, the maximum angular displacement is given by

$$\phi_0 = \frac{T_{\text{osc}}}{n^2 r_1 (r_1 + r_2) m}, \tag{5.1}$$

and m must be designed sufficiently large so that this angle is small. Here T_{osc} is the oscillatory forcing amplitude. (See [54] for a derivation.)

As the machine rotates, the absorber moves in a centrifugal field and its oscillations compensate the vibration of the system to which it is attached. In practice, the radial balance of the machine is important so that at least two or three separate races and absorbers are used. See Figure 5.1(b). In the desirable setting where the motions of the absorbers are synchronised (and hence the machine is balanced), the equations for the rotating motion may be derived assuming one absorber only.

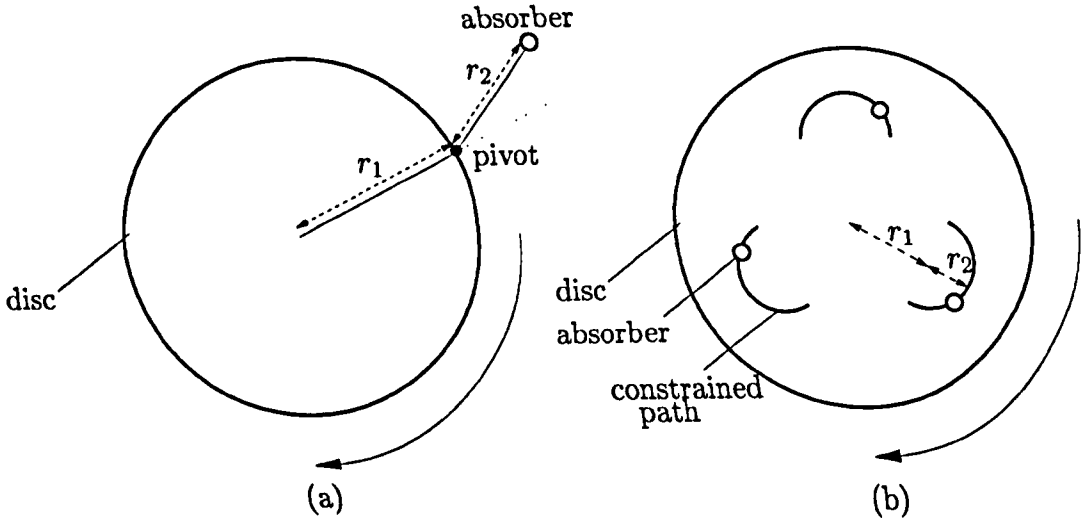

Figure 5.1. (a) Classical centrifugal pendulum vibration absorber attached to the rim of a disc, (b) an alternative configuration where the absorbers are mounted on the disc and move along constrained paths cut into the disc (illustrated for three absorbers).

The most common form of CPVA is the so-called 'bifilar' construction, where each pendulum consists of two parts (see Figures 5.2–5.4). Current applications of CPVAs in industry include helicopter rotors [51] (see Figure 5.2), light aircraft engines [42] and crankshafts in internal combustion engines [41] (see Figure 5.3).

As we have discussed, the absorbers are designed according to linear theory, which is sufficient provided the amplitudes of motion of the absorbers are small. If the absorbers swing through large amplitudes, it is possible for undesirable nonlinear behaviour to occur where the absorbers become detuned. There are currently several different approaches for minimising this nonlinear behaviour. Previous work has examined the optimum path for the absorber to take, including cycloidal [36] (see Figure 5.4) and epicycloidal [52] instead of the classical circular path, which is the simplest to manufacture. Constraints to limit the maximum amplitude of oscillations of the absorber have also been investigated [50].

The aim of this chapter is to determine whether CPVAs are a viable design solution for reducing the unwanted noise and vibration problem in Roots booster pumps. In comparison to the examples mentioned so far we have the added complexity that there are two rotating devices, both eccentrically mounted. To simplify matters and examine the principles of this approach, we shall model only one absorber which is constrained to move along a circular path and which is mounted on only one of the gears.

The chapter is organised as follows. We begin in Section 5.2 by deriving the equations of motion for adding a centrifugal pendulum vibration absorber to the pump. For simplicity we assume that a single CPVA is attached to the X- (driven) gear. In Section

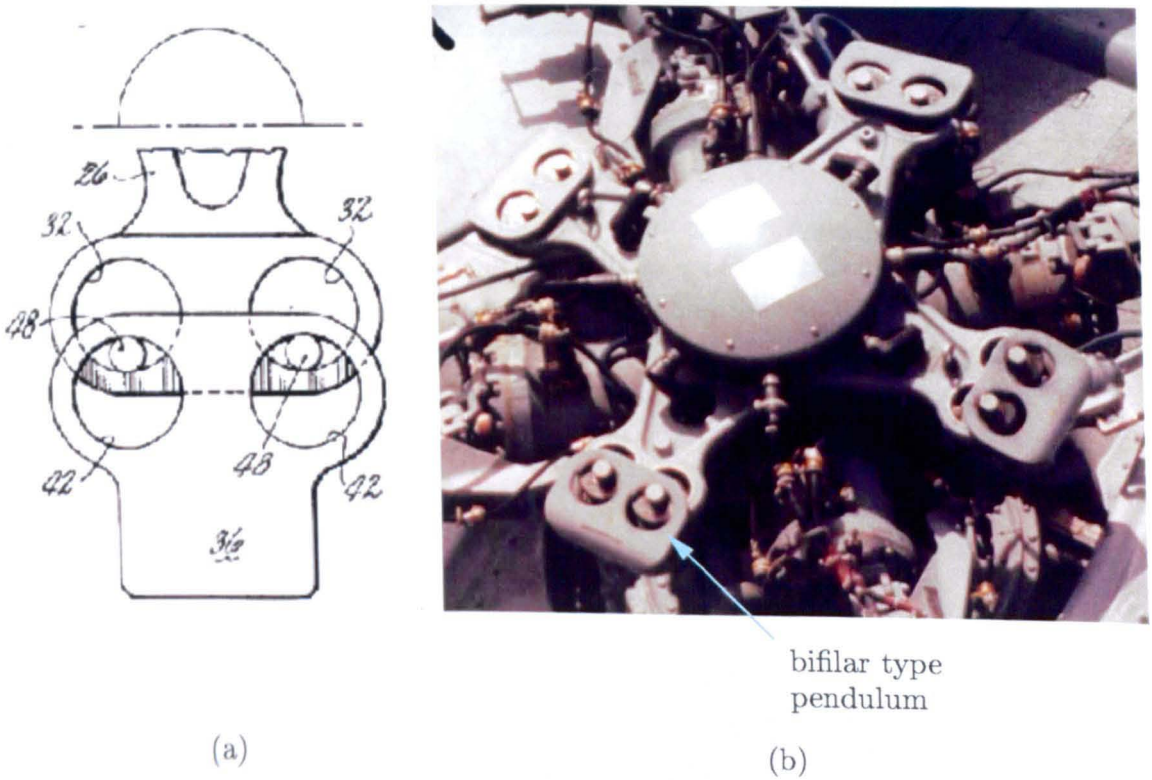

(a) (b)

Figure 5.2. (a) A centrifugal pendulum vibration absorber of bifilar construction. Bifilar pendulums consist of two parts with holes of the same diameter d_1. These parts are joined together by two pins of diameter d_2, where d_2 is smaller than d_1. Thus the radius of the circular path that the pendulum follows has radius $r_2 = d_1 - d_2$. This construction allows for a short effective pendulum that can suppress disturbing torques that are several multiples of the rotation speed (recall that $n^2 = r_1/r_2$) for example due to an internal combustion engine. Reproduced from *Constant Frequency Bifilar Vibration Absorber*, by J.F. Madden (US Patent 4218187 1980). (b) Bifilar centrifugal pendulum vibration absorbers used to reduce torsional vibrations on helicopter rotors. Reproduced with permission from a photograph taken by Steve Shaw [51].

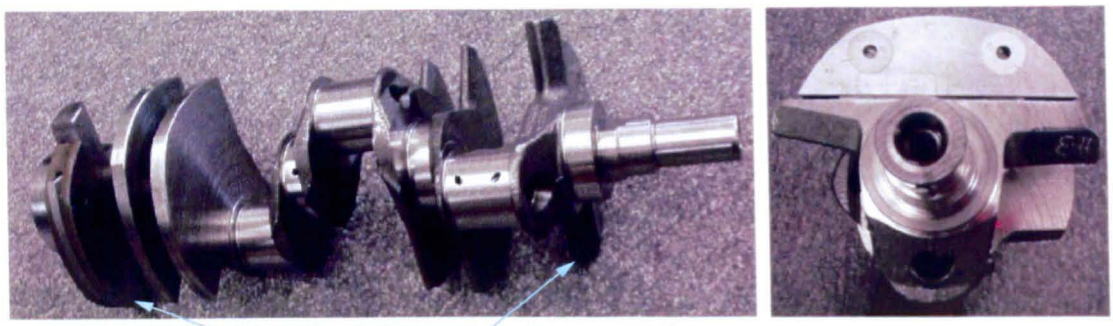

Figure 5.3. (a) A crankshaft used in an experimental engine, with two centrifugal pendulum vibration absorbers attached. (b) one of the pendulum absorbers used on the crankshaft in (a). Reproduced with permission from *Vibration Reduction in Variable Displacement Engines Using Pendulum Absorbers*, by T.M. Nester, A.G. Haddow, S.W. Shaw, J.E. Brevick and V.J Borowski (Proceedings of the SAE Noise and Vibration Conference and Exhibition 2003) [41].

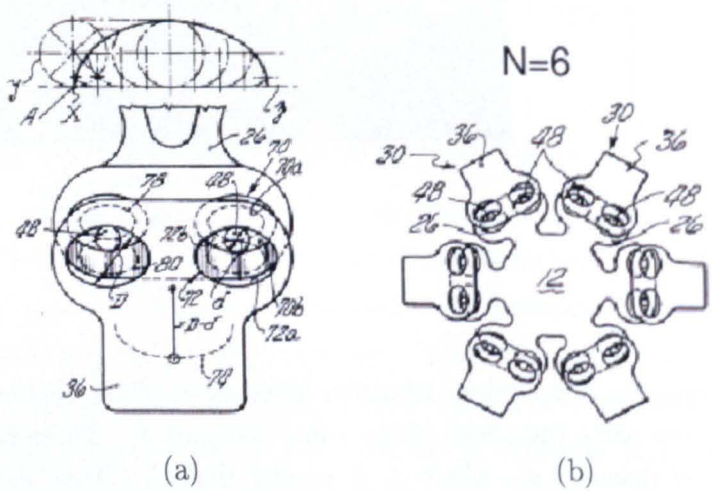

Figure 5.4. A bifilar centrifugal pendulum vibration designed to move on (a) a cycloidal path. (b) Six of these pendulum vibration absorbers used to reduce vibrations in helicopter rotors. Reproduced from *Constant Frequency Bifilar Vibration Absorber*, by J.F. Madden (US Patent 4218187 1980) [36].

5.3 we study quiet linear contact solutions. Since the equations are still nonlinear in this regime (because of rotating frames), we simplify the analysis by assuming that there is no eccentricity on the X-gear, to which the CPVA is attached. We linearize these equations and calculate first-order estimates for CPVA design parameters. This is followed by first-order estimates for the critical eccentricity in Section 5.4. Finally in Section 5.5 we provide some concluding remarks and outline areas for further work.

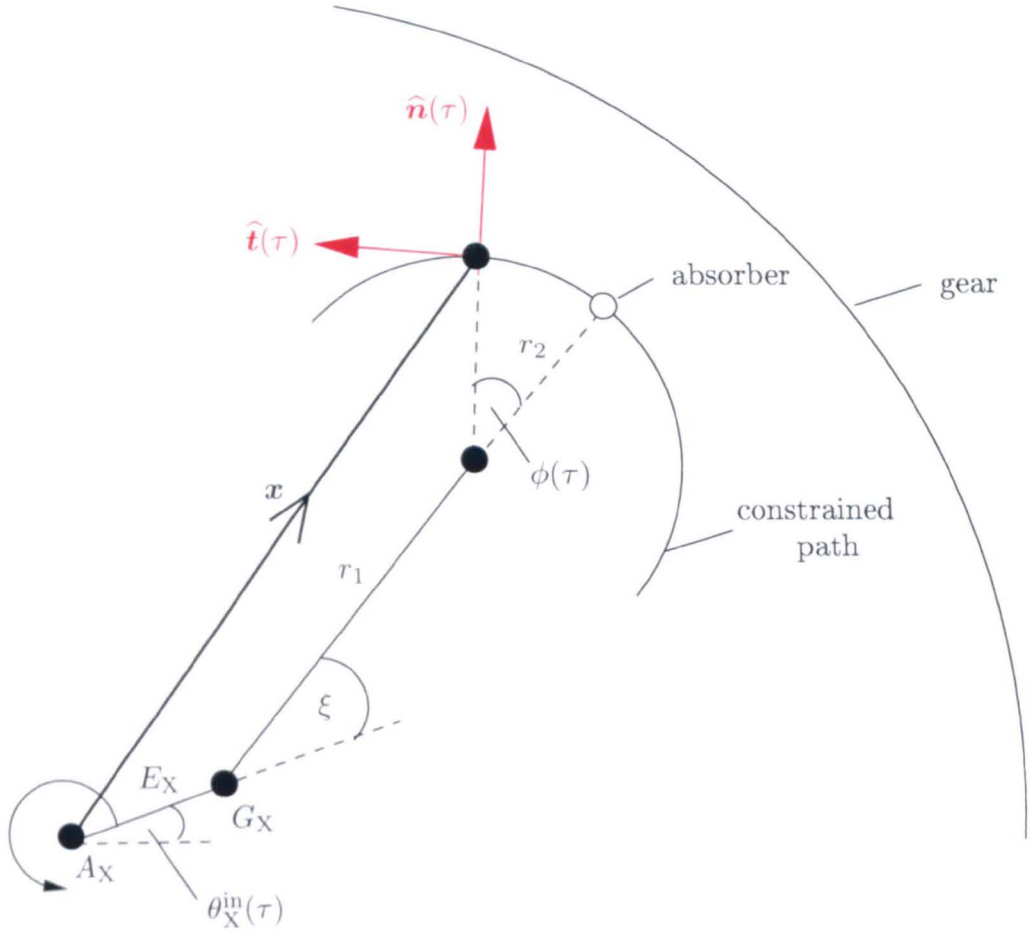

Figure 5.5. A schematic diagram of a centrifugal pendulum vibration absorber attached to an eccentrically mounted gear. The absorber can move on a constrained circular path. For the purposes of visualisation the eccentricity E_X between the axis of rotation A_X and the geometric centre G_X has been greatly exaggerated.

5.2 Incorporation of centrifugal pendulum vibration absorbers

In Figure 5.5 we illustrate a schematic diagram of the proposed design solution that we shall investigate: the CPVA is attached to the X-gear, which is eccentrically mounted with eccentricity E_X. We model the absorber as a point mass of mass m. The distance between the geometric centre of the gear and the centre of the path of the absorber is denoted by r_1. The angle of rotation of the gear measured from the axis of rotation is $\theta_X^{in}(\tau)$. The absorber has angular displacement $\phi(\tau)$, and the radius of its path of rotation is r_2. Finally ξ is the (constant) mounting angle (the offset angle between the eccentricity axis and the neutral position of the absorber). The co-ordinates of the

absorber measured from the axis of rotation of the gear are

$$x(\tau)=E_{\rm X}\begin{pmatrix}\cos\theta_{\rm X}^{\rm in}(\tau)\\ \sin\theta_{\rm X}^{\rm in}(\tau)\end{pmatrix}+r_1\begin{pmatrix}\cos(\theta_{\rm X}^{\rm in}(\tau)+\xi)\\ \sin(\theta_{\rm X}^{\rm in}(\tau)+\xi)\end{pmatrix}+r_2\begin{pmatrix}\cos(\theta_{\rm X}^{\rm in}(\tau)+\phi(\tau)+\xi)\\ \sin(\theta_{\rm X}^{\rm in}(\tau)+\phi(\tau)+\xi)\end{pmatrix}. \tag{5.2}$$

With reference to Figure 5.5, the unit vectors normal and tangential to the absorber are

$$\widehat{n}(\tau)=\begin{pmatrix}\cos(\theta_{\rm X}^{\rm in}(\tau)+\phi(\tau)+\xi)\\ \sin(\theta_{\rm X}^{\rm in}(\tau)+\phi(\tau)+\xi)\end{pmatrix},\qquad \widehat{t}(\tau)=\begin{pmatrix}-\sin(\theta_{\rm X}^{\rm in}(\tau)+\phi(\tau)+\xi)\\ \cos(\theta_{\rm X}^{\rm in}(\tau)+\phi(\tau)+\xi)\end{pmatrix}. \tag{5.3}$$

The radial and transverse components of acceleration of the absorber, $a^{\rm r}$ and $a^{\rm t}$ respectively, are found to be

$$a^{\rm r}=\ddot{x}.\widehat{n}=E_{\rm X}\ddot{\theta}_{\rm X}^{\rm in}\sin(\phi+\xi)+r_1\ddot{\theta}_{\rm X}^{\rm in}\sin\phi-E_{\rm X}(\dot{\theta}_{\rm X}^{\rm in})^2\cos(\phi+\xi)-r_1(\dot{\theta}_{\rm X}^{\rm in})^2\cos\phi - r_2(\dot{\theta}_{\rm X}^{\rm in}+\dot{\phi})^2, \tag{5.4}$$

$$a^{\rm t}=\ddot{x}.\widehat{t}=E_{\rm X}\ddot{\theta}_{\rm X}^{\rm in}\cos(\phi+\xi)+r_1\ddot{\theta}_{\rm X}^{\rm in}\cos\phi+E_{\rm X}(\dot{\theta}_{\rm X}^{\rm in})^2\sin(\phi+\xi)+r_1(\dot{\theta}_{\rm X}^{\rm in})^2\sin\phi + r_2(\ddot{\theta}_{\rm X}^{\rm in}+\ddot{\phi}). \tag{5.5}$$

Resolving forces radially and tangentially to the absorber we have

$$ma^{\rm r} = m\ddot{x}.\widehat{n}=N_{\rm A}, \tag{5.6}$$

$$ma^{\rm t} = m\ddot{x}.\widehat{t}=-c_{\rm A}\dot{\phi}, \tag{5.7}$$

where m and $c_{\rm A}$ are the mass and the damping coefficient of the absorber respectively, and $N_{\rm A}$ is the normal reaction from the absorber on the gear. To calculate the moment on the gear we compute

$$|x\wedge(-N_{\rm A}\widehat{n}+c_{\rm A}\dot{\phi}\widehat{t})|=-N_{\rm A}|x\wedge\widehat{n}|+c_{\rm A}\dot{\phi}|x\wedge\widehat{t}|, \tag{5.8}$$

where

$$|x\wedge\widehat{n}| = E_{\rm X}\sin(\phi+\xi)+r_1\sin\phi, \tag{5.9}$$

$$|x\wedge\widehat{t}| = r_2+E_{\rm X}\cos(\phi+\xi)+r_1\cos\phi. \tag{5.10}$$

To this end, we label ϕ as $\phi_{\rm A}$, to allow for the addition of more absorbers, that would be equally spaced around the gear. Here, however, we leave this refinement to future work and we consider the simplest case of only one absorber.

The equations of motion (derived in Appendix A) for the X-rotor $\theta_{\mathrm{X}}^{\mathrm{mass}}$, Y-rotor $\theta_{\mathrm{Y}}^{\mathrm{mass}}$ and Y-gear $\theta_{\mathrm{Y}}^{\mathrm{in}}$ remain unchanged when we add the CPVA to the X-gear. Recall that these are

$$I_{\mathrm{X}}\ddot{\theta}_{\mathrm{X}}^{\mathrm{mass}} = -c_{\mathrm{X}}\dot{\theta}_{\mathrm{X}}^{\mathrm{mass}} + k_{\mathrm{X}}\left(\theta_{\mathrm{X}}^{\mathrm{in}} - \theta_{\mathrm{X}}^{\mathrm{mass}}\right), \tag{5.11}$$

$$I_{\mathrm{Y}}\ddot{\theta}_{\mathrm{Y}}^{\mathrm{mass}} = -c_{\mathrm{Y}}\dot{\theta}_{\mathrm{Y}}^{\mathrm{mass}} + k_{\mathrm{Y}}\left(\theta_{\mathrm{Y}}^{\mathrm{in}} - \theta_{\mathrm{Y}}^{\mathrm{mass}}\right), \tag{5.12}$$

$$0 = k_{\mathrm{Y}}\left(\theta_{\mathrm{Y}}^{\mathrm{in}} - \theta_{\mathrm{Y}}^{\mathrm{mass}}\right) - N, \tag{5.13}$$

where $I_{\mathrm{X,Y}}$ and $c_{\mathrm{X,Y}}$ are the moments of inertia and damping coefficients of the X- and Y-rotors, $k_{\mathrm{X,Y}}$ are the torsional stiffnesses acting on the X- and Y-shafts and N is the interaction torque between the gears. However, we need to add extra terms, representing the moments generated by the absorbers, to the equation of motion of the X-gear. This yields

$$0 = k\left(\theta_{\mathrm{X}}^{\mathrm{in}} - \theta_{\mathrm{X}}^{\mathrm{mass}}\right) - T + N_{\mathrm{A}}|\boldsymbol{x} \wedge \widehat{\boldsymbol{n}}| - c_{\mathrm{A}}\dot{\phi}_{\mathrm{A}}|\boldsymbol{x} \wedge \widehat{\boldsymbol{t}}| + N. \tag{5.14}$$

If we substitute for N_{A} using equations (5.4) and (5.6), and then substitute for $|\boldsymbol{x} \wedge \widehat{\boldsymbol{n}}|$ and $|\boldsymbol{x} \wedge \widehat{\boldsymbol{t}}|$ using equations (5.9) and (5.10) respectively, we have

$$\begin{aligned} 0 = k\left(\theta_{\mathrm{X}}^{\mathrm{in}} - \theta_{\mathrm{X}}^{\mathrm{mass}}\right) - T + f(\phi)\ddot{\theta}_{\mathrm{X}}^{\mathrm{in}} - g(\theta_{\mathrm{X}}^{\mathrm{in}}, \phi_{\mathrm{A}}, \dot{\phi}_{\mathrm{A}}) \\ - c_{\mathrm{A}}\dot{\phi}_{\mathrm{A}}\left(r_2 + E_{\mathrm{X}}\cos(\phi_{\mathrm{A}} + \xi + r_1\cos\phi_A)\right) + N, \end{aligned} \tag{5.15}$$

where for algebraic convenience we define

$$f(\phi_{\mathrm{A}}) = m(E_{\mathrm{X}}\sin(\phi + \xi) + r_1\sin\phi_{\mathrm{A}})^2, \tag{5.16}$$

and

$$\begin{aligned} &g(\dot{\theta}_{\mathrm{X}}^{\mathrm{in}}, \phi_{\mathrm{A}}, \dot{\phi}_{\mathrm{A}}) \\ &\quad = m[E_{\mathrm{X}}(\dot{\theta}_{\mathrm{X}}^{\mathrm{in}})^2 + r_1(\dot{\theta}_{\mathrm{X}}^{\mathrm{in}})^2\cos\phi + r_2(\dot{\theta}_{\mathrm{X}}^{\mathrm{in}} + \dot{\phi})^2](E_{\mathrm{X}}\sin(\phi + \xi) + r_1\sin\phi). \end{aligned} \tag{5.17}$$

In addition to our system of equations (5.11), (5.12), (5.13) and (5.15) we also have an extra equation of motion for the CPVA displacement ϕ_{A} which is found from resolving the forces tangential to the absorber. From equations (5.5) and (5.7) we have

$$\begin{aligned} mr_2\ddot{\phi}_{\mathrm{A}} + m[r_2 + E_{\mathrm{X}}\cos(\phi_{\mathrm{A}} + \xi) + r_1\cos\phi_{\mathrm{A}}]\ddot{\theta}_{\mathrm{X}}^{\mathrm{in}} \\ = -c_{\mathrm{A}}\dot{\phi}_{\mathrm{A}} - m[E_{\mathrm{X}}\sin(\phi_{\mathrm{A}} + \xi) + r_1\sin\phi_{\mathrm{A}}](\dot{\theta}_{\mathrm{X}}^{\mathrm{in}})^2. \end{aligned} \tag{5.18}$$

We therefore have a system of five equations (5.11), (5.12), (5.13) (5.15) and (5.18) for

six unknowns θ_X^{mass}, θ_Y^{mass}, θ_X^{in}, θ_Y^{in}, ϕ_A and N. However, we can eliminate N by adding (5.13) and (5.15) to give

$$f(\phi)\ddot{\theta}_X^{in} = T - k\left(\theta_X^{in} - \theta_X^{mass}\right) + g(\theta_X^{in}, \phi_A, \dot{\phi}_A) + c_A\dot{\phi}_A\left(r_2 + E_X\cos(\phi_A + \xi) + r_1\cos\phi_A\right), \quad (5.19)$$

so that we have a system of four equations in five unknowns. Note that (5.18) and (5.19) are now ordinary differential equations for θ_X^{in}, whereas for the one degree-of-freedom model θ_X^{in} only appeared as an algebraic constraint (see Appendix A). Equations (5.11), (5.12), (5.18) and (5.19) are closed by prescribing the freeplay or contact conditions. Recall that in freeplay there is no interaction torque between the gears ($N = 0$), thus from (5.13) we can deduce

$$\theta_Y^{in} = \theta_Y^{mass}. \quad (5.20)$$

In linear contact we have

$$\theta_X^{in} - \theta_Y^{in} + \varepsilon\cos(2\pi\Omega\tau + p) = \beta, \quad (5.21)$$

and in torque reversal we have

$$\theta_X^{in} - \theta_Y^{in} + \varepsilon\cos(2\pi\Omega\tau + p) = -\beta. \quad (5.22)$$

Conditions (5.20)–(5.22) allow algebraic elimination of θ_Y^{in}, in each of the regimes. Therefore, we have a system of four equations

$$I_X\ddot{\theta}_X^{mass} = -c_X\dot{\theta}_X^{mass} + k_X\left(\theta_X^{in} - \theta_X^{mass}\right), \quad (5.23)$$

$$I_Y\ddot{\theta}_Y^{mass} = -c_Y\dot{\theta}_Y^{mass} + b_1(\theta_X^{in}, \theta_Y^{mass}), \quad (5.24)$$

$$f(\phi)\ddot{\theta}_X^{in} = T - k\left(\theta_X^{in} - \theta_X^{mass}\right) + g(\theta_X^{in}, \phi_A, \dot{\phi}_A) + c_A\dot{\phi}_A\left(r_2 + E_X\cos(\phi_A + \xi) + r_1\cos\phi_A\right) - b_1(\theta_X^{in}, \theta_Y^{mass}), \quad (5.25)$$

$$mr_2\ddot{\phi}_A + m[r_2 + E_X\cos(\phi_A + \xi) + r_1\cos\phi_A]\ddot{\theta}_X^{in} = -c_A\dot{\phi}_A - m[E_X\sin(\phi_A + \xi) + r_1\sin\phi_A](\dot{\theta}_X^{in})^2, \quad (5.26)$$

in four unknowns $\theta_{\mathrm{X}}^{\mathrm{mass}}$, $\theta_{\mathrm{Y}}^{\mathrm{mass}}$, $\theta_{\mathrm{X}}^{\mathrm{in}}$ and ϕ_{A} where

$$b_1(\theta_{\mathrm{X}}^{\mathrm{in}}, \theta_{\mathrm{Y}}^{\mathrm{mass}}) = \begin{cases} k_{\mathrm{Y}}\left(\theta_{\mathrm{X}}^{\mathrm{in}} - \theta_{\mathrm{Y}}^{\mathrm{mass}} + \varepsilon\cos(2\pi\Omega\tau + p) - \beta\right), & \text{(X drives Y)} \\ 0, & \textit{(freeplay)} \\ k_{\mathrm{Y}}\left(\theta_{\mathrm{X}}^{\mathrm{in}} - \theta_{\mathrm{Y}}^{\mathrm{mass}} + \varepsilon\cos(2\pi\Omega\tau + p) + \beta\right). & \text{(Y drives X)} \end{cases} \tag{5.27}$$

Note that the condition for loss or re-establishment of contact of the gear teeth can be written in the form

$$\theta_{\mathrm{X}}^{\mathrm{in}} - \theta_{\mathrm{Y}}^{\mathrm{mass}} + \varepsilon\cos(2\pi\Omega\tau + p) = \pm\beta, \tag{5.28}$$

see Appendix A.

5.3 First-order estimates for CPVA design parameters

Initially, we are concerned with permanent linear contact solutions where the X-shaft continuously drives the Y-shaft, without any loss of contact between the gears. We are particularly interested in calculating a new critical eccentricity, above which silent solutions cannot exist, and observing the effect that the addition of a centrifugal pendulum vibration absorber has on this bound.

In PLC we can substitute the expression for $\theta_{\mathrm{Y}}^{\mathrm{in}}$ using equation (5.22) into our system of equations (5.23)–(5.26). If we assume that $k_{\mathrm{X}} = k_{\mathrm{Y}} := k$, then in matrix form we have

$$\begin{pmatrix} I_{\mathrm{X}} & 0 & 0 & 0 \\ 0 & I_{\mathrm{Y}} & 0 & 0 \\ 0 & 0 & m\left(E_{\mathrm{X}}\sin(\phi_{\mathrm{A}} + \xi) + r_1\sin\phi_{\mathrm{A}}\right)^2 & 0 \\ 0 & 0 & m(E_{\mathrm{X}}\cos(\phi_{\mathrm{A}} + \xi) + r_1\cos\phi_{\mathrm{A}} + r_2) & mr_2 \end{pmatrix} \begin{pmatrix} \ddot{\theta}_{\mathrm{X}}^{\mathrm{mass}} \\ \ddot{\theta}_{\mathrm{Y}}^{\mathrm{mass}} \\ \ddot{\theta}_{\mathrm{X}}^{\mathrm{in}} \\ \ddot{\phi}_{\mathrm{A}} \end{pmatrix} = \begin{pmatrix} h_1 \\ h_2 \\ h_3 \\ h_4 \end{pmatrix}, \tag{5.29}$$

where

$$h_1 = -c_{\mathrm{X}}\dot{\theta}_{\mathrm{X}}^{\mathrm{mass}} + k(\theta_{\mathrm{X}}^{\mathrm{in}} - \theta_{\mathrm{X}}^{\mathrm{mass}}), \tag{5.30}$$

$$h_2 = -c_{\mathrm{Y}}\dot{\theta}_{\mathrm{Y}}^{\mathrm{mass}} + k(\theta_{\mathrm{X}}^{\mathrm{in}} - \theta_{\mathrm{Y}}^{\mathrm{mass}} + \varepsilon\cos(2\pi\Omega\tau + p) - \beta), \tag{5.31}$$

$$h_3 = k\left(\theta_{\mathrm{Y}}^{\mathrm{mass}} + \theta_{\mathrm{X}}^{\mathrm{mass}} - 2\theta_{\mathrm{X}}^{\mathrm{in}} - \varepsilon\cos(2\pi\Omega\tau + p) + \beta\right) + T + g(\theta_{\mathrm{X}}^{\mathrm{in}}, \phi_{\mathrm{A}}, \dot{\phi}_{\mathrm{A}}), \tag{5.32}$$

$$h_4 = -c_{\mathrm{A}}\dot{\phi}_{\mathrm{A}} - m\left[E_{\mathrm{X}}(\dot{\theta}_{\mathrm{X}}^{\mathrm{in}})^2\sin(\phi_{\mathrm{A}} + \xi) + r_1(\dot{\theta}_{\mathrm{X}}^{\mathrm{in}})^2\sin\phi_{\mathrm{A}}\right]. \tag{5.33}$$

To simplify the analysis and to make analytical progress we assume that the X-gear (which has the CPVA mounted on it) is concentrically mounted on the X-shaft, but that there remains eccentricity on the Y-gear. We therefore proceed by setting $E_{\mathrm{X}} = 0$.

Note that the total effective eccentricity, ε, is now given by ε_Y, the non-dimensional eccentricity on the Y-gear. We have

$$\begin{pmatrix} I_X & 0 & 0 & 0 \\ 0 & I_Y & 0 & 0 \\ 0 & 0 & mr_1^2 \sin^2\phi_A & 0 \\ 0 & 0 & m(r_1\cos\phi_A + r_2) & mr_2 \end{pmatrix} \begin{pmatrix} \ddot{\theta}_X^{\text{mass}} \\ \ddot{\theta}_Y^{\text{mass}} \\ \ddot{\theta}_X^{\text{in}} \\ \ddot{\phi}_A \end{pmatrix} = \begin{pmatrix} h_1 \\ h_2 \\ h_3 \\ h_4 \end{pmatrix}, \tag{5.34}$$

where

$$h_1 = -c_X\dot{\theta}_X^{\text{mass}} + k(\theta_X^{\text{in}} - \theta_X^{\text{mass}}), \tag{5.35}$$

$$h_2 = -c_Y\dot{\theta}_Y^{\text{mass}} + k(\theta_X^{\text{in}} - \theta_Y^{\text{mass}} + \varepsilon\cos(2\pi\Omega\tau + p) - \beta), \tag{5.36}$$

$$\begin{aligned} h_3 = {} & k\left(\theta_Y^{\text{mass}} + \theta_X^{\text{mass}} - 2\theta_X^{\text{in}} - \varepsilon\cos(2\pi\Omega\tau + p) + \beta\right) + T \\ & + mr_1\left[r_1(\dot{\theta}_X^{\text{in}})^2\cos\phi_A\sin\phi_A + r_2(\dot{\theta}_X^{\text{in}} + \dot{\phi}_A)^2\sin\phi_A\right] + c_A\dot{\phi}_A\left(r_2 + r_1\cos\phi\right), \end{aligned} \tag{5.37}$$

$$h_4 = -c_A\dot{\phi}_A - mr_1(\dot{\theta}_X^{\text{in}})^2\sin\phi_A. \tag{5.38}$$

If we assume that the shafts and the gears rotate steadily at speed $2\pi\Omega$, on which is superimposed a small sinusoidal oscillation $\widehat{\theta}$, we can write

$$\theta = 2\pi\Omega\tau + \widehat{\theta}. \tag{5.39}$$

By non-dimensionalising time such that

$$t = \Omega\tau, \tag{5.40}$$

as before, we have

$$\dot{\theta} = \Omega\theta' = \Omega(2\pi + \widehat{\theta}'), \tag{5.41}$$

$$\ddot{\theta} = \Omega^2\theta'' = \Omega^2\widehat{\theta}'', \tag{5.42}$$

for θ_X^{in}, θ_X^{mass} and θ_Y^{mass}. In addition we assume that the motion of the absorber relative to the gear is a small sinusoidal oscillation, such that

$$\dot{\phi} = \Omega\phi', \tag{5.43}$$

$$\ddot{\phi} = \Omega^2\phi'', \tag{5.44}$$

where dots denote differentiation with respect to time τ, and dashes denote differentiation with respect to non-dimensional time, t. Note that $\widehat{\theta}_X^{\text{in}}$, $\widehat{\theta}_X^{\text{mass}}$ and $\widehat{\theta}_Y^{\text{mass}}$ are not

necessarily small, but that $(\widehat{\theta}_{\mathrm{X}}^{\mathrm{in}})'$, $(\widehat{\theta}_{\mathrm{X}}^{\mathrm{mass}})'$ and $(\widehat{\theta}_{\mathrm{Y}}^{\mathrm{mass}})'$ are small. *By substituting the* above non-dimensionalising transformations (5.39)–(5.44) and linearizing, we are able to recast the equations of motion (5.34)–(5.38) in the form

$$\begin{pmatrix} \Omega^2 I_{\mathrm{X}} & 0 & 0 & 0 \\ 0 & \Omega^2 I_{\mathrm{Y}} & 0 & 0 \\ 0 & 0 & 0 & 0 \\ 0 & 0 & m\Omega^2(r_1+r_2) & m\Omega^2 r_2 \end{pmatrix} \begin{pmatrix} \widehat{\theta}_{\mathrm{X}}^{\mathrm{mass}} \\ \widehat{\theta}_{\mathrm{Y}}^{\mathrm{mass}} \\ \widehat{\theta}_{\mathrm{X}}^{\mathrm{in}} \\ \phi_{\mathrm{A}} \end{pmatrix}'' = \begin{pmatrix} h_1 \\ h_2 \\ h_3 \\ h_4 \end{pmatrix}, \tag{5.45}$$

where

$$h_1 = -2\pi c_{\mathrm{X}}\Omega - c_{\mathrm{X}}\Omega(\widehat{\theta}_{\mathrm{X}}^{\mathrm{mass}})' + k(\widehat{\theta}_{\mathrm{X}}^{\mathrm{in}} - \widehat{\theta}_{\mathrm{X}}^{\mathrm{mass}}), \tag{5.46}$$

$$h_2 = -2\pi c_{\mathrm{Y}}\Omega - c_{\mathrm{Y}}\Omega(\widehat{\theta}_{\mathrm{Y}}^{\mathrm{mass}})' + k(\widehat{\theta}_{\mathrm{X}}^{\mathrm{in}} - \widehat{\theta}_{\mathrm{Y}}^{\mathrm{mass}} + \varepsilon\cos(2\pi t + p) - \beta), \tag{5.47}$$

$$\begin{aligned} h_3 = {} & k\left(\widehat{\theta}_{\mathrm{Y}}^{\mathrm{mass}} + \widehat{\theta}_{\mathrm{X}}^{\mathrm{mass}} - 2\widehat{\theta}_{\mathrm{X}}^{\mathrm{in}} - \varepsilon\cos(2\pi t + p) + \beta\right) + T \\ & + 4\pi^2 m r_1 \Omega^2 \phi_{\mathrm{A}}(r_1 + r_2) + c_{\mathrm{A}}\Omega\phi_{\mathrm{A}}'(r_1 + r_2), \end{aligned} \tag{5.48}$$

$$h_4 = -c_{\mathrm{A}}\Omega\phi_{\mathrm{A}}' - 4\pi^2 m r_1 \phi_{\mathrm{A}}\Omega^2. \tag{5.49}$$

We observe that since we have modelled both gears to be massless, the mass matrix is now singular. To remove the singularity we proceed by setting $h_3 = 0$. If we equate terms of similar magnitude in h_3 we can find an approximate algebraic constraint on $\widehat{\theta}_{\mathrm{X}}^{\mathrm{in}}$,

$$\widehat{\theta}_{\mathrm{X}}^{\mathrm{in}} = \frac{1}{2}\left(\widehat{\theta}_{\mathrm{Y}}^{\mathrm{mass}} + \widehat{\theta}_{\mathrm{X}}^{\mathrm{mass}} + \frac{T}{k} + \beta - \varepsilon\cos(2\pi t + p)\right), \tag{5.50}$$

which we can substitute into the equations of motion (5.45) to obtain

$$\begin{aligned} & \underbrace{\begin{pmatrix} I_{\mathrm{X}}\Omega^2 & 0 & 0 \\ 0 & I_{\mathrm{Y}}\Omega^2 & 0 \\ \frac{(r_1+r_2)}{2}m\Omega^2 & \frac{(r_1+r_2)}{2}m\Omega^2 & r_2 m\Omega^2 \end{pmatrix}}_{M} \underbrace{\begin{pmatrix} \widehat{\theta}_{\mathrm{X}}^{\mathrm{mass}} \\ \widehat{\theta}_{\mathrm{Y}}^{\mathrm{mass}} \\ \phi_{\mathrm{A}} \end{pmatrix}''}_{u''} \\ = {} & \underbrace{\begin{pmatrix} -c_{\mathrm{X}}\Omega & 0 & 0 \\ 0 & -c_{\mathrm{Y}}\Omega & 0 \\ 0 & 0 & -c_{\mathrm{A}}\Omega \end{pmatrix}}_{B} \underbrace{\begin{pmatrix} \widehat{\theta}_{\mathrm{X}}^{\mathrm{mass}} \\ \widehat{\theta}_{\mathrm{Y}}^{\mathrm{mass}} \\ \phi_{\mathrm{A}} \end{pmatrix}'}_{u'} + \underbrace{\begin{pmatrix} -\frac{k}{2} & \frac{k}{2} & 0 \\ \frac{k}{2} & -\frac{k}{2} & 0 \\ 0 & 0 & -4\pi^2 m r_1 \Omega^2 \end{pmatrix}}_{A} \underbrace{\begin{pmatrix} \widehat{\theta}_{\mathrm{X}}^{\mathrm{mass}} \\ \widehat{\theta}_{\mathrm{Y}}^{\mathrm{mass}} \\ \phi_{\mathrm{A}} \end{pmatrix}}_{u} \\ & + \underbrace{\begin{pmatrix} \frac{T}{2} + \frac{k\beta}{2} - 2\pi c_{\mathrm{X}}\Omega \\ \frac{T}{2} - \frac{k\beta}{2} - 2\pi c_{\mathrm{Y}}\Omega \\ 0 \end{pmatrix}}_{f} + \begin{pmatrix} -\frac{k\varepsilon}{2}\cos(2\pi t + p) \\ \frac{k\varepsilon}{2}\cos(2\pi t + p) \\ -2m(r_1 + r_2)\Omega^2\pi^2\varepsilon\cos(2\pi t + p) \end{pmatrix}. \end{aligned} \tag{5.51}$$

Note that under approximation (5.50) for $\theta_{\mathrm{X}}^{\mathrm{in}}$, the equations of motion for the two rotors $\theta_{\mathrm{X}}^{\mathrm{mass}}$ and $\theta_{\mathrm{Y}}^{\mathrm{mass}}$ become decoupled from the equation of motion that describes the absorber ϕ_{A}. However we proceed with the calculation and we shall return to this approximation in Section 5.4.

The eccentricity term can be written in the form

$$e(t) = \Re\{\varepsilon \exp(2\pi t + p)\mathrm{i}\}, \tag{5.52}$$

where $\Re$ denotes the real part and i the square root of -1. If we write

$$g = \begin{pmatrix} -k\varepsilon/2 \\ k\varepsilon/2 \\ -2m(r_1 + r_2)\Omega^2\pi^2\varepsilon \end{pmatrix}, \tag{5.53}$$

then equation (5.51) can be expressed in the form

$$\boldsymbol{M}\boldsymbol{u}'' = \boldsymbol{B}\boldsymbol{u}' + \boldsymbol{A}\boldsymbol{u} + \boldsymbol{f} + \Re\{\boldsymbol{g}\exp(2\pi t + p)\mathrm{i}\}. \tag{5.54}$$

Using standard techniques we substitute a particular solution of the form

$$\boldsymbol{u} = \boldsymbol{c_1} + \Re\{\boldsymbol{c_2}\exp(2\pi t + p)\mathrm{i}\} \tag{5.55}$$

and compare coefficients to obtain expressions for $\boldsymbol{c_1}$ and $\boldsymbol{c_2}$:

$$\boldsymbol{A}\boldsymbol{c_1} = -\boldsymbol{f}, \tag{5.56}$$

$$(\boldsymbol{A} + 2\pi\mathrm{i}\boldsymbol{B} + 4\pi^2\boldsymbol{M})\boldsymbol{c_2} = -\boldsymbol{g}. \tag{5.57}$$

The matrix $\boldsymbol{A}$ is singular, which implies that $c_{1,1}$ and $c_{1,2}$ are only defined up to adding the same constant to each. Gaussian elimination provides the necessary condition

$$T = 2\pi(c_{\mathrm{X}} + c_{\mathrm{Y}})\Omega \tag{5.58}$$

to solve (5.56). (Note that (5.58) is the natural balance for the mean motor torque T.) If we assume that the damping coefficients of the two shafts are equal ($c_{\mathrm{X}} = c_{\mathrm{Y}} := c$), and neglect the damping on the absorber ($c_{\mathrm{A}} = 0$), then

$$\boldsymbol{c_1} = \begin{pmatrix} 0 \\ -\beta \\ 0 \end{pmatrix}. \tag{5.59}$$

If we also assume that the moments of inertia of the two rotors are equal ($I_{\mathrm{X}} = I_{\mathrm{Y}} := I$),

we have

$$c_2 = \begin{pmatrix} \dfrac{k\varepsilon(2\pi I\Omega - ci)}{4\pi\Omega(I(-k+4\pi^2 I\Omega^2)-c^2)+2c(k-8\pi^2\Omega^2 I)i} \\ -\dfrac{k\varepsilon(2\pi I\Omega - ci)}{4\pi\Omega(I(-k+4\pi^2 I\Omega^2)-c^2)+2c(k-8\pi^2\Omega^2 I)i} \\ \dfrac{\varepsilon(r_1+r_2)}{2(r_2-r_1)} \end{pmatrix}. \tag{5.60}$$

If we return to the equation of motion for the X-gear (5.15), and neglect damping on the absorber ($c_A = 0$), then take terms up to first order in $\widehat{\theta}_X^{in}$, $\widehat{\theta}_X^{mass}$ and ϕ_A, we obtain

$$0 = k\left(\widehat{\theta}_X^{in} - \widehat{\theta}_X^{mass}\right) - T - 4\pi^2 m r_1 \Omega^2 \phi_A (r_1 + r_2) + N. \tag{5.61}$$

If we substitute for $\widehat{\theta}_X^{in}$ using equation (5.50) and rearrange, we obtain an expression for the interaction torque between the gears,

$$N = \frac{k}{2}\left(\widehat{\theta}_X^{mass} - \widehat{\theta}_Y^{mass} + \varepsilon\cos(2\pi t + p)\right) + \frac{T}{2} - \frac{k\beta}{2} + 4\pi^2 m r_1 \Omega^2 \phi_A (r_1 + r_2). \tag{5.62}$$

If we use (5.55), (5.59) and (5.60) to calculate linearized approximations for $\widehat{\theta}_X^{mass}$, $\widehat{\theta}_Y^{mass}$ and ϕ_A, and substitute into (5.62) we have

$$N = \frac{T}{2} + \varepsilon(a\cos(2\pi t + p) + b\sin(2\pi t + p)), \tag{5.63}$$

where

$$a = \frac{k}{2}\left(\frac{k(-k+4\pi^2\Omega^2 I)}{(k-4\pi^2\Omega^2 I)^2 + 4\pi^2\Omega^2 c^2} + 1\right) + 2m\pi^2 \frac{r_1\Omega^2 (r_1+r_2)^2}{r_2 - r_1}, \tag{5.64}$$

$$b = -\frac{k}{2}\left(\frac{2\pi c\Omega k}{(k-4\pi^2\Omega^2 I)^2 + 4\pi^2\Omega^2 c^2}\right). \tag{5.65}$$

For permanent linear contact solutions, we require the gears to always be in contact, i.e., that the interaction torque between the gears $N > 0$. Rearranging for a bound on the eccentricity ε we have

$$\varepsilon < \frac{T}{2\sqrt{a^2 + b^2}}. \tag{5.66}$$

If we expand (5.66) in small m we have

$$\varepsilon_{crit}^{CPVA} = \varepsilon_{crit}^{1\text{ d.o.f.}}\left(1 - \frac{4\pi^2\Omega^2 r_1 (r_1+r_2)^2 (kI - 4\pi^2\Omega^2 I^2 - c^2)}{k(r_2 - r_1)(c^2 + 4\pi^2\Omega^2 I^2)} m\right) + O(m^2). \tag{5.67}$$

Observe that this bound dictates that for a critical eccentricity that is infinite (within this framework of approximations) we should design $r_1 = r_2$. This is not entirely unexpected as we are trying to suppress vibrations that are order one, i.e., at the same order as the rotation rate. Although this calculation provides us with the ratio of r_1 to

r_2, for realism we need to repeat this calculation when the equations of motion of the rotors do not become decoupled from the equation of motion of the absorber.

5.4 First-order estimates for the critical eccentricity

Recall that in Section 5.3 when constructing permanent linear contact solutions we calculated an approximate algebraic constraint (5.50) on $\widehat{\theta}_{\mathrm{X}}^{\mathrm{in}}$. We now return to this point and repeat the same calculation when we do not approximate this constraint. The new algebraic constraint on $\widehat{\theta}_{\mathrm{X}}^{\mathrm{in}}$ is

$$\widehat{\theta}_{\mathrm{X}}^{\mathrm{in}} = \frac{1}{2}\left(\widehat{\theta}_{\mathrm{Y}}^{\mathrm{mass}} + \widehat{\theta}_{\mathrm{X}}^{\mathrm{mass}} + \frac{T}{k} + \beta - \varepsilon\cos(2\pi t + p) + \frac{4\pi^2 m r_1 \Omega^2 \phi_{\mathrm{A}}(r_1 + r_2)}{k} + \frac{c_{\mathrm{A}}\Omega\phi'_{\mathrm{A}}(r_1 + r_2)}{k}\right). \quad (5.68)$$

If we substitute this expression into the equations of motion (5.45) we obtain a third-order system in the form

$$M_3 u''' + M_2 u'' + M_1 u' + M_0 u = f + g\cos(2\pi t + p), \quad (5.69)$$

where

$$M_3 = \begin{pmatrix} 0 & 0 & 0 \\ 0 & 0 & 0 \\ 0 & 0 & mc\Omega^3(r_1 + r_2)^2/2k \end{pmatrix}, \quad (5.70)$$

$$M_2 = \begin{pmatrix} I_{\mathrm{X}}\Omega^2 & 0 & 0 \\ 0 & I_{\mathrm{Y}}\Omega^2 & 0 \\ (r_1 + r_2)m\Omega^2/2 & (r_1 + r_2)m\Omega^2/2 & r_2 m\Omega^2 + 2m\Omega^2 r_1 \pi^2 (r_1 + r_2)^2/k \end{pmatrix}, \quad (5.71)$$

$$M_1 = \begin{pmatrix} c_{\mathrm{X}}\Omega & 0 & -c_{\mathrm{A}}\Omega(r_1 + r_2)/2 \\ 0 & c_{\mathrm{Y}}\Omega & -c_{\mathrm{A}}\Omega(r_1 + r_2)/2 \\ 0 & 0 & c_{\mathrm{A}}\Omega \end{pmatrix}, \quad (5.72)$$

$$M_0 = \begin{pmatrix} k/2 & -k/2 & -2mr_1\Omega^2\pi^2(r_1 + r_2) \\ -k/2 & k/2 & -2mr_1\Omega^2\pi^2(r_1 + r_2) \\ 0 & 0 & 4\pi^2 m r_1 \Omega^2 \end{pmatrix}, \quad (5.73)$$

$$\boldsymbol{f} = \begin{pmatrix} T/2 + k\beta/2 - 2\pi c_X \Omega \\ T/2 - k\beta/2 - 2\pi c_Y \Omega \\ 0 \end{pmatrix}, \tag{5.74}$$

$$\boldsymbol{g} = \begin{pmatrix} -k\varepsilon/2 \\ k\varepsilon/2 \\ -2m(r_1 + r_2)\Omega^2\pi^2\varepsilon \end{pmatrix}. \tag{5.75}$$

If we follow the same procedure outlined in Section 5.3 we can substitute a particular solution of the form

$$\boldsymbol{u} = \boldsymbol{c_1} + \Re\{\boldsymbol{c_2}\exp(2\pi t + p)\mathrm{i}\} \tag{5.76}$$

and compare coefficients to obtain expressions for $\boldsymbol{c_1}$ and $\boldsymbol{c_2}$. Once we have solved for $\boldsymbol{u}$ we can calculate new expressions for both the maximum amplitude of oscillations ϕ_0 and the critical eccentricity $\varepsilon_{\text{crit}}^{\text{CPVA}}$. These expressions are lengthy, hence here we only report their series expansions in small m. We have

$$\phi_0 = \frac{\varepsilon\pi\Omega(r_1 + r_2)}{c_A} m + O(m^2), \tag{5.77}$$

and (on substituting $r_1 = r_2$),

$$\varepsilon_{\text{crit}}^{\text{CPVA}} = \varepsilon_{\text{crit}}^{1\text{ d.o.f.}} \left(1 - \frac{8\pi^2\Omega^2 r_1^2(kI - 4\pi^2\Omega^2 I^2 - c^2)}{k(c^2 + 4\pi^2\Omega^2 I^2)} m\right) + O(m^2). \tag{5.78}$$

(See (2.36) for the one degree-of-freedom critical eccentricity $\varepsilon_{\text{crit}}^{1\text{ d.o.f.}}$.)

Observe that since $kI > 4\pi^2\Omega^2 I^2 + c^2$ for all realistic parameters, the $O(m)$ term will always be positive. Therefore, this calculation implies that the addition of one CPVA to a concentric driven (X-) gear actually decreases the critical eccentricity. To investigate this further we perform three sets of numerical experiments for standard machine parameters (for a booster of type A). We plot the exact first-order expressions (not expanded in small m) of the critical eccentricity and maximum amplitude of oscillations, against (i) the radius of the path of the absorber r_2, (ii) the mass of the absorber m, and finally (iii) the damping on the absorber c_A.

From the scale of the y-axis in Figure 5.6(a) we observe that for fixed m, c_A and r_1, varying r_2 has little effect on the critical eccentricity. However, the amplitude of oscillations of the absorber is found to be at its maximum when $r_1 = r_2$, see Figure 5.6(b). In Figure 5.7 we find that for fixed c_A, r_1 and r_2, increasing the mass of the absorber worsens both the critical eccentricity and the maximum amplitude of oscillations of the absorber. As mass increases the critical eccentricity decreases and at the same time the maximum amplitude of oscillations of the absorber increase. In Figure 5.8 we observe that for fixed m, r_1 and r_2, increasing the damping on the absorber

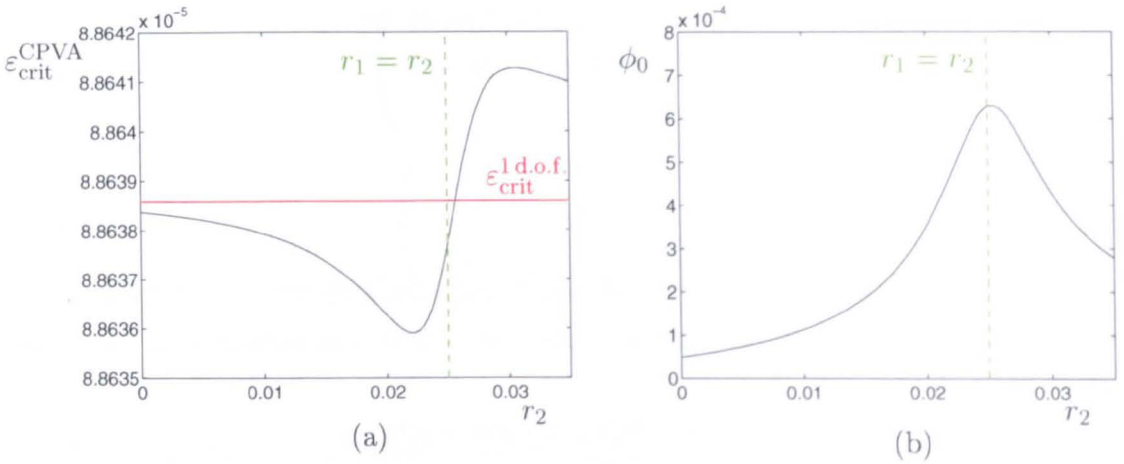

Figure 5.6. Critical eccentricity and maximum amplitude of oscillations of the absorber as a function of the radius of the path of the absorber r_2. For comparison the critical eccentricity bound for the one degree-of-freedom model (2.36) is also shown. In addition, the line where the radius of the path of the absorber is equal to the distance between the geometric centre of the gear and the centre of the path of the absorber is overlaid.

increases the critical eccentricity and decreases the maximum amplitude of oscillations.

5.5 Discussion

To summarise, we have investigated the feasibility of using CPVAs to reduce unwanted vibrations in Roots booster pumps. We have derived a four degree-of-freedom system to describe the simplest scenario when one absorber is mounted on the driven (X-) gear and is constrained to move along a circular groove cut into the gear. To make analytical progress we assumed that the X-gear was concentrically mounted, but that there remains eccentricity on the Y-gear.

The surprising result we have found, at the linear level, is that the introduction of a CPVA accentuates the gear rattle problem by reducing the critical eccentricity. Additionally, in contrast to other CPVA systems, the maximum displacement of the CPVA actually *increases* as the mass of the absorber increases. This seems entirely counter-intuitive. However, we should bear in mind that in quiet operation, the X-gear on which the CPVA is mounted must suffer a small amplitude oscillation due to the Y-gear eccentricity. It is not clear how to modify/improve the CPVA idea to tolerate this small amplitude motion, yet damp out larger motions associated with disconnection.

Moreover, satisfying the critical eccentricity is only one factor in silent operation of a pump. A more complete analysis would require basins of attraction computations

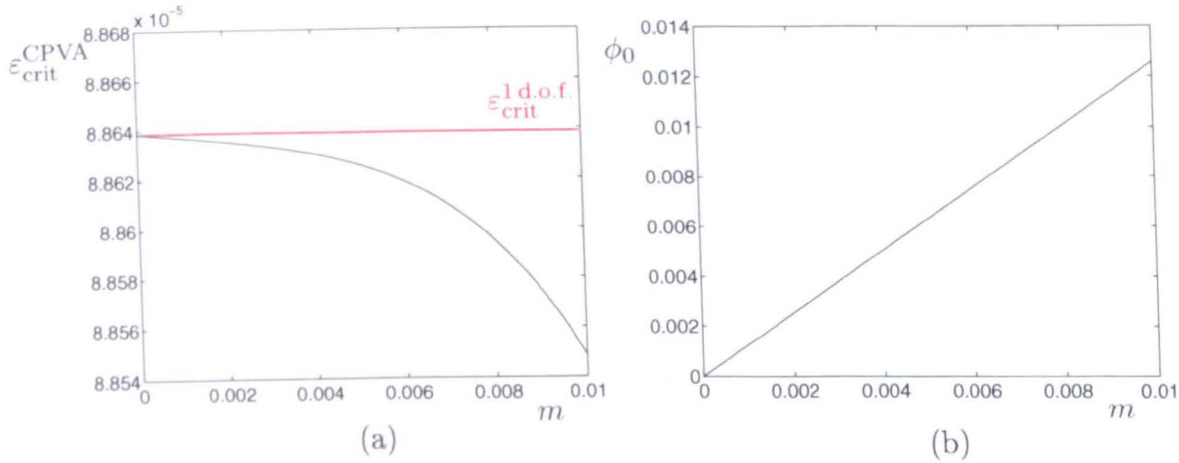

Figure 5.7. Critical eccentricity and maximum amplitude of oscillations of the absorber as a function of the mass of the absorber m. For comparison the critical eccentricity bound for the one degree-of-freedom model (2.36) is also shown.

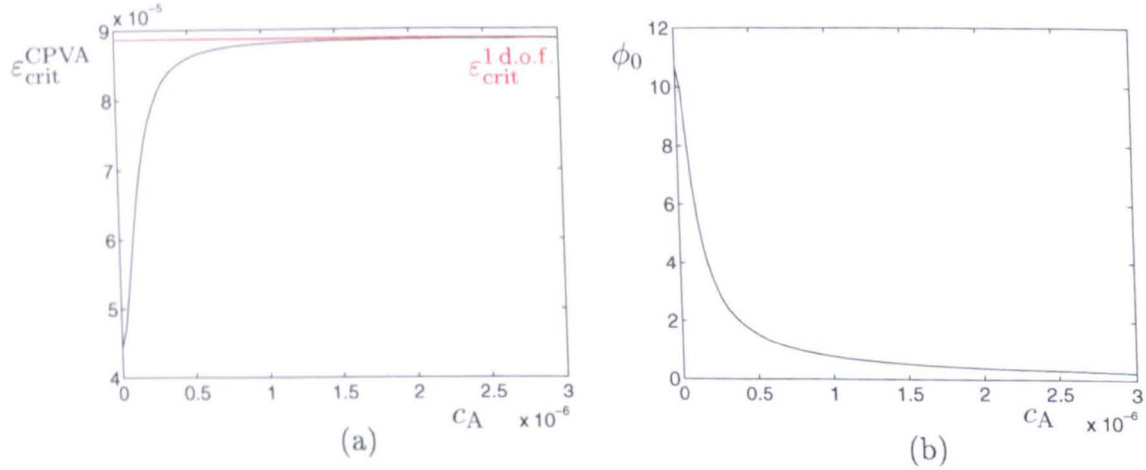

Figure 5.8. Critical eccentricity and maximum amplitude of oscillations of the absorber as a function of the damping on the absorber c_{A}. For comparison the critical eccentricity bound for the one degree-of-freedom model (2.36) is also shown.

(as seen in Chapter 3) to determine if the addition of a CPVA increases the size of the basin corresponding to PLC solutions. We defer this to future work. Furthermore, we have only considered the simplest (and most likely the cheapest and easiest) design solution of adding only one absorber to one gear. We believe that examining the effect of adding (one or more) CPVAs to both gears provides an interesting area worthy of further investigation.

Chapter 6

Conclusions

In this thesis we have investigated gear rattle in Roots booster pumps, a problem which is generic to lightly-loaded systems. We have been concerned with gaining an understanding of the underlying dynamics, as well as developing practical design solutions. We now summarise the main results of the thesis and outline some potential areas for future work.

6.1 Retrospective view of the thesis

In Chapter 2 we described how eccentric mounting of the gears can introduce an oscillatory forcing effect, which operates at the gross rotation rate of the pump. Whilst in practice the eccentricity is only a few tens of microns, it is sufficiently large to drive noisy operation, and it has therefore been one of the key parameters that we have investigated. We derived a one degree-of-freedom second-order nonsmooth ordinary differential equation to describe the dynamics of the pump, where we model each shaft assembly as a rigid body.

The nonlinearity in our models arises from the backlash between the gear teeth, which we model as a piecewise-smooth continuous function. Due to the large stiffness in the system we were able to introduce a simpler impacting limit of backlash, although the model is still nonlinear due to impacts. Many assumptions were made in the modelling process and it would be interesting to see how the model would be affected by incorporating, for example, lubrication between the gear teeth or contact ratio effects.

We outlined the techniques employed to calculate both linear 'silent' solutions and illustrative examples of nonlinear rattling solutions. In addition we calculated a bound on the eccentricity (the *critical eccentricity*), above which silent solutions cannot exist, and this bound correlates with experimental observation. Unfortunately satisfying the critical eccentricity does not guarantee silent operation and there is the potential

for rattling solutions to coexist, providing a possible explanation for intermittency or unreliability.

To gain a better understanding of the coexisting dynamics, in Chapter 3 we extended the Chapter 2 study by carrying out a comprehensive numerical investigation of initial condition space. As we wished to calculate basins of attraction for a very large number of initial conditions and for a range of different parameter values, we were particularly concerned with carrying out these computations efficiently. By exploiting the linearity between impacts we were able to avoid numerical integration, and instead construct maps and use root-finding methods to locate impacts or crossings of the two backlash boundaries.

To extract the global properties of the mappings we employed the method of cell-to-cell mapping [27, 28]. Due to the small damping in the system we refined the method to minimise the effect of long transients. We believe that this refinement may be useful for future investigations of other systems that suffer from long transients.

Basins of attraction were found to be very small and fragmented for realistic machine parameters, thus for the purpose of illustration we computed and compared basins of attraction for scaled-up parameter values. One-parameter bifurcation diagrams illuminated several smooth and discontinuity-induced bifurcations, which provided insight into some of the mechanisms by which solutions can be created or destroyed. In addition, we explored the intricate stretching and folding of phase space by calculating the grazing curve and its pre-images, as well as the stable manifolds. We think that the interactions of the pre-image grazing curves and manifolds are worthy of further investigation. We also believe that we have only scratched the surface of the rich dynamics that this model can exhibit. We outline a few potential areas for future work in Section 6.2.

From a practical perspective it is unrealistic to expect the pump controller systems to have precise control of initial conditions in an industrial environment. Consequently, the remainder of the thesis was dedicated to the development of practical design solutions.

In Chapter 4 we extended the existing one degree-of-freedom model to a two degree-of-freedom model where we did not assume that the moments of inertia of the two shaft assemblies were equal. The aim was to determine if adding a flywheel to the driven shaft of the pump would increase the critical eccentricity. Using the methodologies outlined in Chapter 2, we calculated a new bound on the critical eccentricity and also on the simplest type of rattling solution. Our results indicated that adding mass to the pump actually worsens both these bounds. In contrast, we found that removing mass offered an improvement.

In summary, given a choice of removing (for example) 5% of mass from each shaft or 10% of mass from one, it is actually better to build an asymmetrical machine. However, in the current configuration this is infeasible and it is best to remove as much mass from the pump as is possible, without compromising its structural integrity. This design change has since been implemented by BOCE and they now hollow out the centres of the rotors further than they did previously. However, removing mass really only offers a temporary design solution as the next generation of pumps will be bigger and/or faster.

The rest of Chapter 4 was dedicated to examining another design solution suggested by BOCE, namely the 'sprung-gear' system. We constructed a three degree-of-freedom model to describe mounting the driving (X-) gear on the Y-shaft by means of a torsional spring. Linear calculations indicated a marked increase in critical eccentricity, although we believe experiments should be carried out to determine the robustness of this design solution. In addition, we would also wish to determine the effect that the sprung-gear has on nonlinear rattling solutions, and we return to this in Section 6.3.

In Chapter 5 we presented the idea of incorporating centrifugal pendulum vibration absorbers (CPVAs), a type of passive tuned absorbers, into our pump. For simplicity we investigated mounting one absorber, which is free to move in a circular path, on the driven (X-) gear. Preliminary calculations indicate that, for small angular displacements of the absorber, the bound on critical eccentricity is actually worsened. However, to develop the analysis presented here the basins of attraction should be computed; the effect of mounting several absorbers on both gears should be investigated; and also the nonlinear behaviour that occurs when the absorber moves through large amplitudes examined.

6.2 Rich dynamics

The numerical study of the simple one degree-of-freedom model of gear rattle in Chapter 3 revealed a very rich dynamical structure. Here we discuss a few related ideas that may be taken further.

In Figure 3.10 we plotted the basins of attraction diagrams for the piecewise-linear and impacting-contact model for the same parameters. Although in very good agreement, we only compared these plots visually, and we suggest that a more detailed comparison is worthy of future work.

In Section 2.4.2 in Chapter 2 we described the procedure for constructing periodic solutions of type $P(1,1,0)$ and $P(1,1,1)$ that are in-phase and out-of-phase with the forcing. In Section 3.5.2 in Chapter 3 we used these techniques to construct two saddles

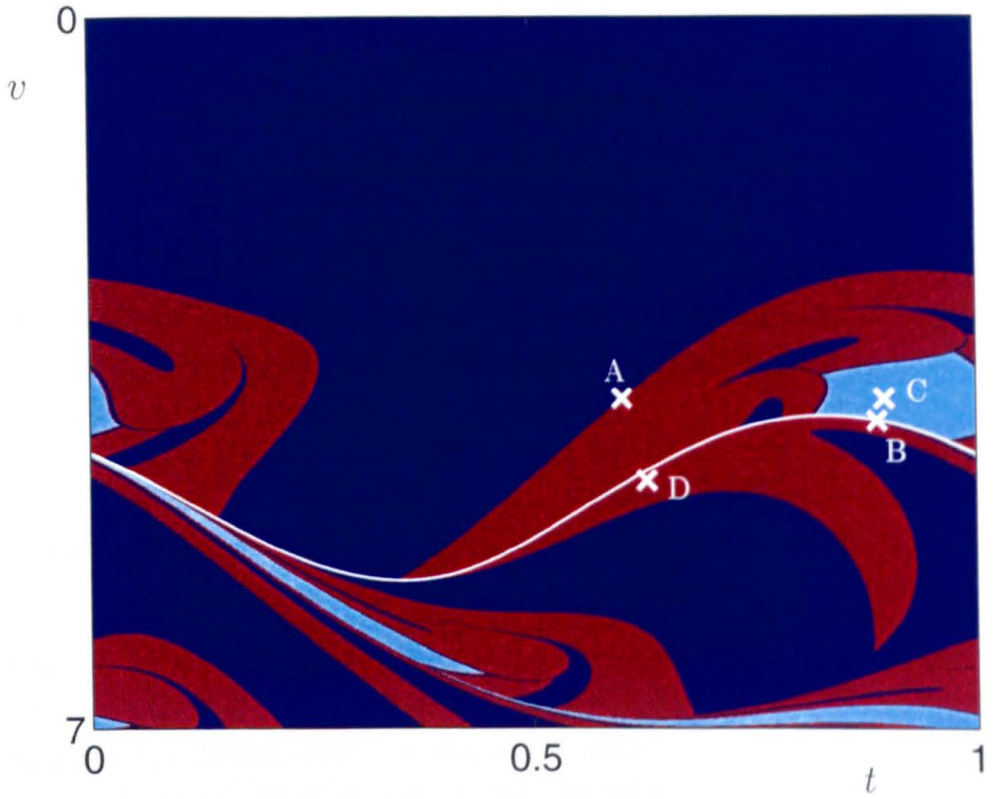

Figure 6.1. The location of the $P(1,1,0)$ out-of-phase and in-phase solutions (A and C) and the $P(1,1,1)$ in-phase and out-of-phase solutions (B and D) overlaid on the basin of attraction for the impacting-contact model given by equations (2.28), (2.38) for $\delta = 0.6$, $\beta = 0.6$ and $\varepsilon = 0.1$.

so that we could calculate manifolds of the basin boundaries. These saddles were the out-of-phase solution of type $P(1,1,0)$, and the in-phase solution of type $P(1,1,1)$, which we denoted A and B.

To complete the analysis we now construct the in-phase solution of type $P(1,1,0)$ and the out-of-phase solution of type $P(1,1,1)$. We label these as C and D, and plot all these points on the corresponding basin of attraction in Figure 6.1. As described in Section 2.4.4 in Chapter 2, we can calculate bounds on the existence of these types of solution. These boundaries may be identified as bifurcations [23, 24], and we can plot a two-parameter bifurcation diagram in the δ-ε plane. This is shown in Figure 6.2, and can help provide some further insight into the dynamics observed in Section 3.4 in Chapter 3. Note that where all these curves meet we have a codimension-two point, namely a grazing fold (GF).

Recall that we plotted basins of attraction for when eccentricity is varied (Figure

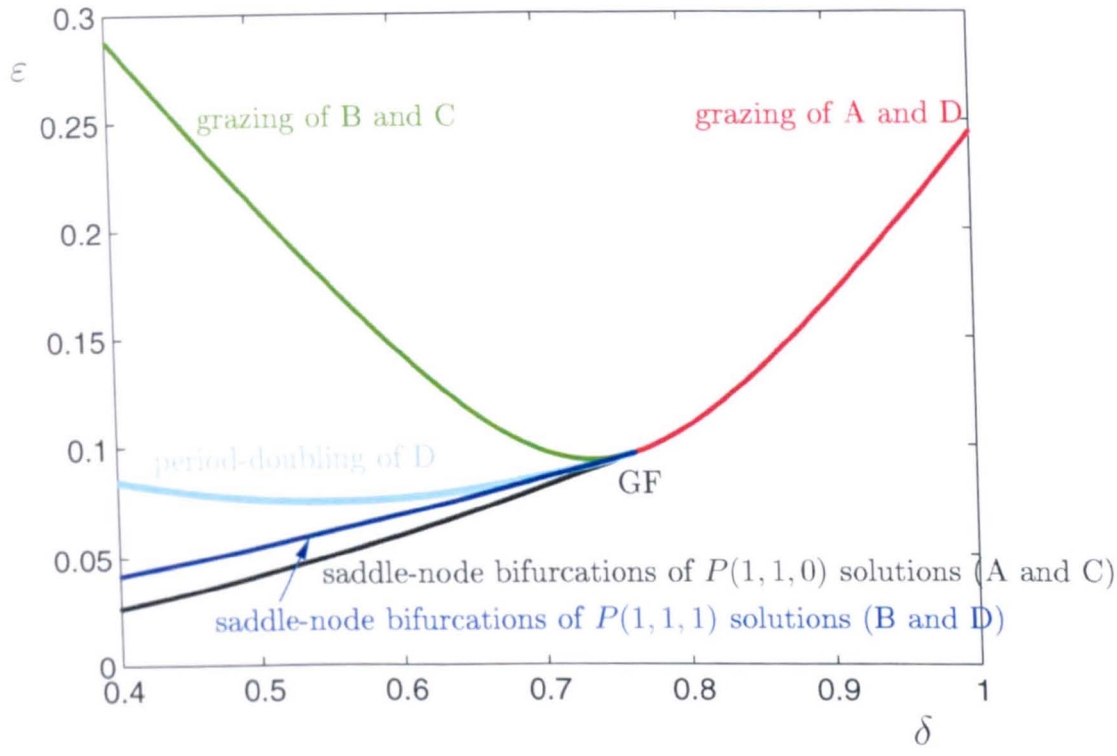

Figure 6.2. The existence bounds for the $P(1,1,0)$ and $P(1,1,1)$ solutions. The curves all meet in a grazing fold (GF) codimension-two point.

3.11) and also for when damping is varied (Figure 3.12). If we take a slice through the two-parameter diagram Figure 6.2 when $\delta = 0.6$ we can follow some of the observed transitions in Figure 3.11. In Figure 3.11(a) all initial conditions result in PLC and there are no $P(1,1,0)$ or $P(1,1,1)$ solutions. As the eccentricity increases the $P(1,1,0)$ solutions (A and C) are born in a saddle-node (at $\varepsilon = 0.0596$), and by (b) the basin corresponding to C, the out-of-phase (stable) solution is observable in light blue. At $\varepsilon = 0.0687$ the $P(1,1,1)$ solutions (B and D) are born in a saddle-node, and by (d) a very small basin corresponding to D, the out-of-phase (stable) solution emerges in light orange. D period doubles at $\varepsilon = 0.076$ and by (e) the light orange basin has turned dark orange (and now corresponds to a $P(1,2,2)$ solution).

Similarly, we can take a slice through Figure 6.2 when $\varepsilon = 0.1$. In Figure 3.12(e) the in-phase $P(1,1,0)$ solution (corresponding to C on Figure 6.1) is stable, and its basin is represented by the light blue region. As damping increases C grazes at $\delta = 0.6905$ and by (i) this basin is destroyed.

In summary, although the one degree-of-freedom model is the simplest model that we consider in this thesis, from a theoretical point of view there is still much work to be done to unfold and understand all of its dynamics.

6.3 Sprung-gear rattling solutions

In the second half of Chapter 4 we calculated a critical eccentricity for the sprung-gear system. We are also interested in how the sprung-gear affects the nonlinear rattling solutions. Since the explicit solutions of equations (4.108)–(4.110) are lengthy, we have not attempted to use the solution construction techniques, employed for the one and two degree-of-freedom models in Sections 2.4.2 and 4.3.1 respectively. Instead, our approach is entirely numerical.

As an illustrative example we solve the sprung-gear initial value problem (4.108)–(4.110), for machine parameters for a range of initial conditions. For comparison, we also solve the one degree-of-freedom model initial value problem (2.26) for identical parameters and initial conditions. The parameters have been chosen so that silent PLC solutions exist in both models. Each simulation has been run for 2000 non-dimensional units of time, and only the last 20 periods of forcing have been plotted, to reduce the effect of long transients. The two backlash boundaries $\Phi = \pm\beta$ are overlaid in red. The results of the numerics for both models are shown in Figures 6.3 and 6.4. The panels have been labelled (a)-(y) such that the same letter corresponds to the same initial condition. An indication of the noise level of each solution has been calculated as the sum of the squares of the impact velocities, re-normalised by time. All values are recorded in Table 6.1 and are given to three significant figures.

We observe that only one panel displays a permanent linear contact solution, see Figure 6.4(y). It appears that the addition of the sprung-gear, for all of the initial conditions tested here, makes the calculated noise levels worse. However, it is also interesting to note that for some initial conditions (c), (r) and (x), in particular, impacts with both backlash boundaries in the one degree-of-freedom model have been replaced with multiple, low impact velocities with just the top backlash boundary in the sprung-gear model. In practice, this corresponds to the addition of the sprung-gear preventing the pump from visiting torque reversal. For these cases the calculated noise values are unintuitively larger than for the one degree-of-freedom model, due to the high number of impacts. However, it would be interesting to see how these low-impact velocity solutions are affected if we modelled the lubrication between the gear teeth. Would the addition of oil be sufficient to force these solutions to stay in permanent linear contact? Another criticism of the current model is the 'lumped' approach. It would be interesting to see how the model changes if we employed a more refined modelling approach (as described in Appendix A) where the rotors and gears are modelled separately.

We also return to comment on the marked increase in critical eccentricity, that lower torsional stiffnesses appear to offer, as seen in Figure 4.4(a). It is debatable whether

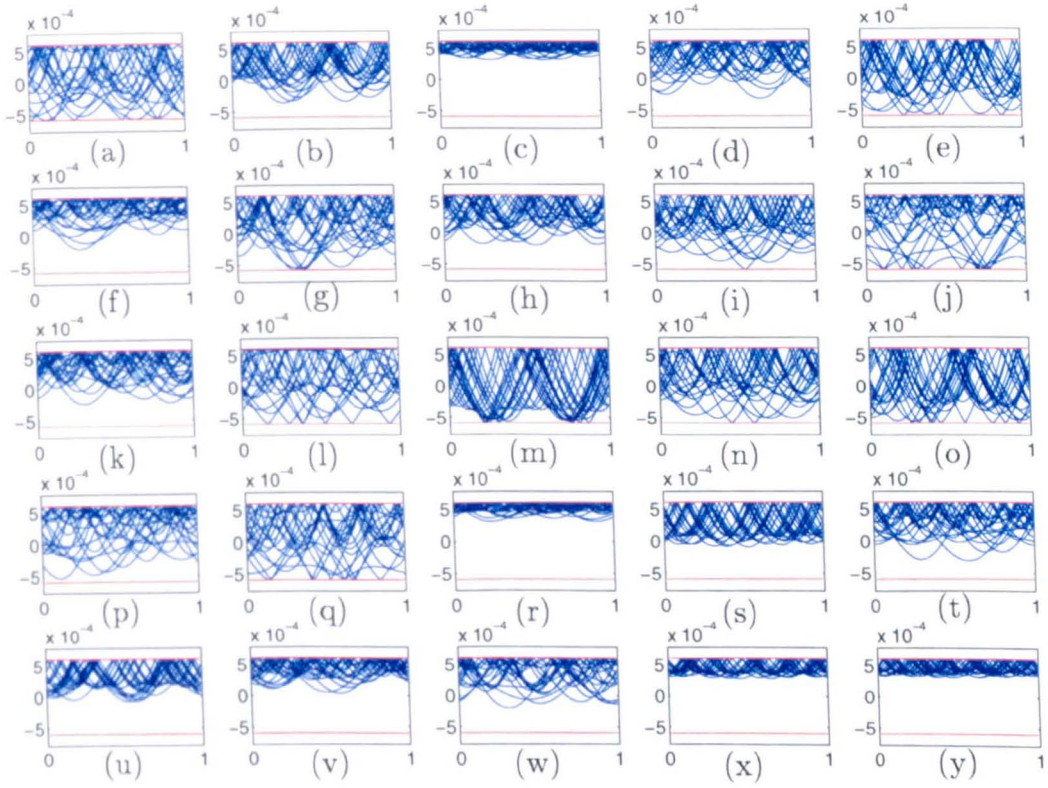

Figure 6.3. Numerical simulations of the initial value problem for the sprung-gear system (4.108)–(4.110) in the impacting-limit for identical machine parameters (for which silent PLC solutions exist), and a variety of different initial conditions. Each graph is a plot of relative rotational displacement ($\Phi(t) = \theta_g(t) - \theta_Y(t) + e(t)$) against time t, plotted over the last 20 periods of forcing, with $\Phi = \pm\beta$ overlaid in red. See Table 6.1 for the calculated noise level for each plot.

our existing model is still valid for such small stiffnesses. Currently, we do not attempt to model the stiffness of the gear teeth themselves, and it is possible that incorporating a term for the gear teeth stiffness would modify the results presented here.

Finally, the models of gear rattle and design solutions presented in this thesis require a detailed and extensive programme of experimental validation following, for example the approach of Ottewill *et al* [47]. However, to test our results for the specific application investigated here it would be necessary to obtain the gearing mechanism from an actual Roots booster pump and run it with appropriate lubrication at realistic operating speeds. This would probably require high-speed cameras to determine the relative tooth configurations and would constitute a substantial new project in its own right.

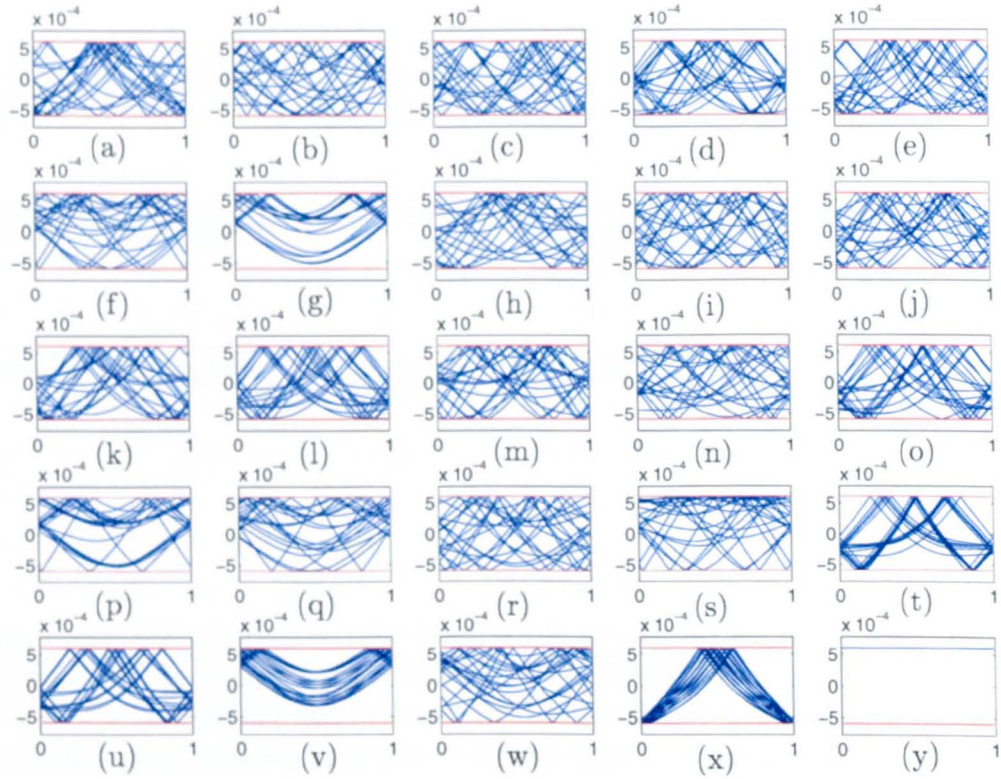

Figure 6.4. Numerical simulations of the initial value problem for the one degree-of-freedom model (2.28), (2.38) in the impacting-limit for identical machine parameters (for which silent PLC solutions exist), and a variety of different initial conditions. Each graph is a plot of relative rotational displacement ($\Phi(t) = \theta_X(t) - \theta_Y(t) + e(t)$) against time t, plotted over the last 20 periods of forcing, with $\Phi = \pm\beta$ overlaid in red. See Table 6.1 for the calculated noise level for each plot.

Panel	Sprung-gear system	One degree-of-freedom model
(a)	1.26×10^{-4}	1.54×10^{-5}
(b)	1.11×10^{-4}	1.41×10^{-5}
(c)	5.43×10^{-5}	1.69×10^{-5}
(d)	9.84×10^{-5}	1.82×10^{-5}
(e)	1.29×10^{-4}	1.96×10^{-5}
(f)	7.47×10^{-5}	9.60×10^{-6}
(g)	1.14×10^{-4}	3.56×10^{-6}
(h)	9.98×10^{-5}	1.26×10^{-5}
(i)	1.23×10^{-4}	1.64×10^{-5}
(j)	1.25×10^{-4}	1.71×10^{-5}
(k)	9.67×10^{-5}	1.75×10^{-5}
(l)	1.16×10^{-4}	1.89×10^{-5}
(m)	1.45×10^{-4}	1.67×10^{-5}
(n)	1.31×10^{-4}	1.22×10^{-5}
(o)	1.51×10^{-4}	1.85×10^{-5}
(p)	9.24×10^{-5}	6.61×10^{-6}
(q)	1.39×10^{-4}	7.39×10^{-6}
(r)	4.85×10^{-5}	1.40×10^{-5}
(s)	9.51×10^{-5}	1.20×10^{-5}
(t)	1.02×10^{-4}	1.87×10^{-5}
(u)	9.61×10^{-5}	1.93×10^{-5}
(v)	7.14×10^{-5}	3.53×10^{-6}
(w)	8.40×10^{-5}	8.81×10^{-6}
(x)	6.80×10^{-5}	1.80×10^{-5}
(y)	6.40×10^{-5}	0

Table 6.1. Table of calculated noise levels for the sprung-gear and one degree-of-freedom models. Each letter corresponds to the same initial condition.

Appendix A

Refined Modelling Approach

In Chapters 1–4, we have modelled each shaft with its attached gear and rotor as a single rigid body with lumped moments of inertia, torsional stiffness and damping parameters. Here we justify the lumped modelling approach by decomposing the machine into components and by showing that the resulting sets of equations are equivalent.

In practice, the inertias of the assembled shafts are much larger than the inertia of the gears. We therefore approximate the gears as massless (and undamped) and assume that the inertia of the system is entirely due to the two rotors. We also model the shafts as a light elastic connection between the rotors and the gears. We assume that the rotors are mounted concentrically on the shafts, i.e., that their centres of rotation and geometric centres coincide, but that the gears are mounted eccentrically.

We introduce six new variables $\theta^{\text{mass}}_{\text{X,Y}}$, $\theta^{\text{in}}_{\text{X,Y}}$ and $\theta^{\text{out}}_{\text{X,Y}}$ to measure the angular displacements of individual components. Here, $\theta^{\text{mass}}_{\text{X,Y}}$ are measured at the rotors, $\theta^{\text{in}}_{\text{X,Y}}$ are measured from the axis of rotation of the gears and $\theta^{\text{out}}_{\text{X,Y}}$ are measured at the pitch circle of the gears where meshing occurs. These are all labelled on a schematic diagram of the pump in Figure A.1.

As before, we apply Newton's second law of motion to derive the equations of motion for the pump. For the two rotors we have

$$I_{\text{X}}\ddot{\theta}^{\text{mass}}_{\text{X}} = -c_{\text{X}}\dot{\theta}^{\text{mass}}_{\text{X}} + k_{\text{X}}\left(\theta^{\text{in}}_{\text{X}} - \theta^{\text{mass}}_{\text{X}}\right), \tag{A.1}$$

$$I_{\text{Y}}\ddot{\theta}^{\text{mass}}_{\text{Y}} = -c_{\text{Y}}\dot{\theta}^{\text{mass}}_{\text{Y}} + k_{\text{Y}}\left(\theta^{\text{in}}_{\text{Y}} - \theta^{\text{mass}}_{\text{Y}}\right), \tag{A.2}$$

and for the two gears

$$0 = k_{\text{X}}\left(\theta^{\text{in}}_{\text{X}} - \theta^{\text{mass}}_{\text{X}}\right) - T + N, \tag{A.3}$$

$$0 = k_{\text{Y}}\left(\theta^{\text{in}}_{\text{Y}} - \theta^{\text{mass}}_{\text{Y}}\right) - N, \tag{A.4}$$

since a non-zero resultant torque would result in infinite acceleration. The moments of inertia and damping coefficients of the X- and Y-rotors are given by $I_{\text{X,Y}}$ and $c_{\text{X,Y}}$,

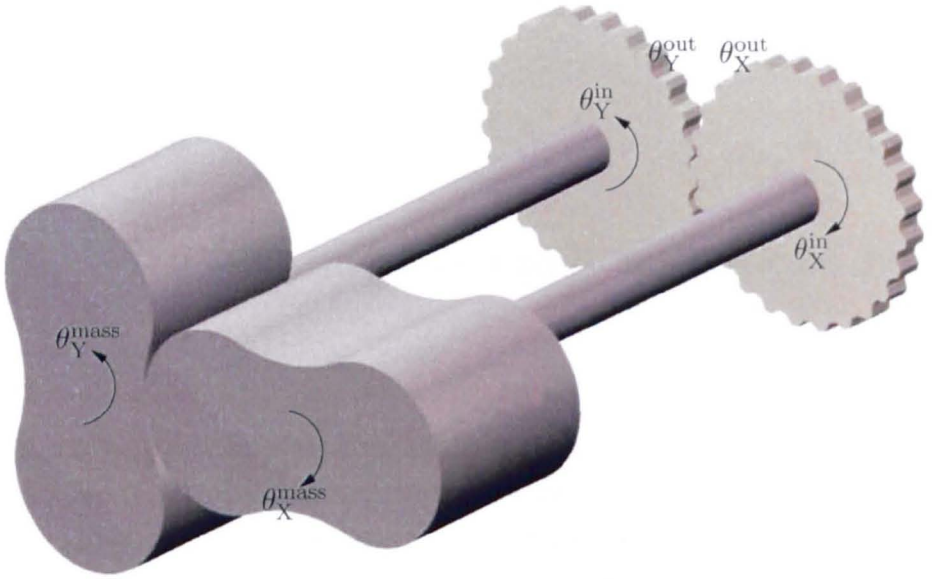

Figure A.1. Schematic diagram illustrating the parallel arrangement of rotors, shafts and gears and where the new variables are measured. Note that we have not illustrated the electric motor on the X-shaft.

respectively and $k_{X,Y}$ are the torsional stiffnesses acting on the X- and Y-shafts. The motor torque is given by T. Here N is the interaction torque between the gears, so that when the gears are in contact $N > 0$. Note that in freeplay when the gears are out of contact we have $N = 0$.

In addition we have two equations which describe the relationships between $\theta_{X,Y}^{in}$ (the rotational displacements measured about the eccentric axis of rotation of the gears) and $\theta_{X,Y}^{out}$ (which parameterise the outer radius of the gear where meshing occurs). These are

$$\theta_X^{out} = \theta_X^{in} + \varepsilon_X \cos(2\pi\Omega\tau + p_X), \tag{A.5}$$

$$\theta_Y^{out} = \theta_Y^{in} + \varepsilon_Y \cos(2\pi\Omega\tau + p_Y), \tag{A.6}$$

which can be combined to give

$$\theta_X^{in} - \theta_Y^{in} = \theta_X^{out} - \theta_Y^{out} - \varepsilon \cos(2\pi\Omega\tau + p), \tag{A.7}$$

where ε is given by the total (non-dimensional) effective eccentricity

$$\varepsilon = \sqrt{\varepsilon_X^2 + \varepsilon_Y^2 - 2\varepsilon_X\varepsilon_Y \cos\xi}. \tag{A.8}$$

We note that the ordinary differential equations (ODEs) (A.1)-(A.3) and (A.7) hold for all time, irrespective of whether the gears are in contact. The model is closed by prescribing the freeplay or contact conditions. In freeplay the gears are out of contact, so the interaction torque $N = 0$. From ODE (A.4) this gives

$$\theta_{\mathrm{Y}}^{\mathrm{in}} = \theta_{\mathrm{Y}}^{\mathrm{mass}}. \tag{A.9}$$

When the gears are in contact we have expressions to describe the relationships between the two co-ordinates ($\theta_{\mathrm{X}}^{\mathrm{out}}$ and $\theta_{\mathrm{Y}}^{\mathrm{out}}$) which parameterise the outer radius of the gear at the meshing point. In linear contact $\theta_{\mathrm{X}}^{\mathrm{out}} - \theta_{\mathrm{Y}}^{\mathrm{out}} = \beta$ (where, as before, β is the half-backlash width). Therefore, from (A.7) we have

$$\theta_{\mathrm{X}}^{\mathrm{in}} - \theta_{\mathrm{Y}}^{\mathrm{in}} = \beta - \varepsilon\cos(2\pi\Omega\tau). \tag{A.10}$$

In torque reversal $\theta_{\mathrm{X}}^{\mathrm{out}} - \theta_{\mathrm{Y}}^{\mathrm{out}} = -\beta$, so from (A.7) we have

$$\theta_{\mathrm{X}}^{\mathrm{in}} - \theta_{\mathrm{Y}}^{\mathrm{in}} = -\beta - \varepsilon\cos(2\pi\Omega\tau). \tag{A.11}$$

Conditions (A.9)-(A.11) allow algebraic elimination of $\theta_{\mathrm{Y}}^{\mathrm{in}}$ (the angular displacement of the Y-gear) in each of the regimes.

In Section 2.2.2 in Chapter 2 we described how the mean torque T balances the drag torque, and need not be given as a separate parameter. We show that this is also the case for our more refined modelling approach. Adding ODEs (A.4) and (A.3) we have

$$T = k_{\mathrm{X}}\left(\theta_{\mathrm{X}}^{\mathrm{in}} - \theta_{\mathrm{X}}^{\mathrm{mass}}\right) + k_{\mathrm{Y}}\left(\theta_{\mathrm{Y}}^{\mathrm{in}} - \theta_{\mathrm{Y}}^{\mathrm{mass}}\right), \tag{A.12}$$

which holds for all time. If we assume that the system is in quasi-steady operation, i.e., there is no torque ripple, and we average ODEs (A.1) and (A.2) over one gross rotation, we obtain

$$k_{\mathrm{X}}\langle\theta_{\mathrm{X}}^{\mathrm{in}} - \theta_{\mathrm{X}}^{\mathrm{mass}}\rangle = c_{\mathrm{X}}\langle\dot{\theta}_{\mathrm{X}}^{\mathrm{mass}}\rangle, \tag{A.13}$$

$$k_{\mathrm{Y}}\langle\theta_{\mathrm{Y}}^{\mathrm{in}} - \theta_{\mathrm{Y}}^{\mathrm{mass}}\rangle = c_{\mathrm{Y}}\langle\dot{\theta}_{\mathrm{Y}}^{\mathrm{mass}}\rangle. \tag{A.14}$$

By assuming $c_{\mathrm{X}} = c_{\mathrm{Y}} =: c$ and $\langle\dot{\theta}_{\mathrm{X}}^{\mathrm{mass}}\rangle = \langle\dot{\theta}_{\mathrm{Y}}^{\mathrm{mass}}\rangle = 2\pi c\Omega$, we have

$$\langle T\rangle = 4\pi c\Omega, \tag{A.15}$$

as before.

We now check to ensure that under certain assumptions, namely that the moments of inertia, damping and torsional stiffnesses are the same for both shaft assemblies, we

recover the equations of motion in the one degree-of-freedom model, ODEs (2.27)–(2.29) derived in Section 2.2.3. Firstly, we assume that $k_X = k_Y =: k$, then from equation (A.12) we can find an algebraic constraint on θ_X^{in}:

$$\theta_X^{in} = -\theta_Y^{in} + \frac{T}{k} + \theta_X^{mass} + \theta_Y^{mass}. \tag{A.16}$$

If we use the appropriate equation from (A.9)–(A.11) to substitute into (A.16), we can write differential equations for θ_X^{mass} and θ_Y^{mass} in the three regimes (linear contact, freeplay and torque reversal):

(a) X-shaft drives Y-shaft (linear contact) :

$$I_X\ddot{\theta}_X^{mass} + c_X\dot{\theta}_X^{mass} + \frac{k}{2}(\theta_X^{mass} - \theta_Y^{mass} + \varepsilon\cos(2\pi\Omega t + p) - \beta) = \frac{T}{2}, \tag{A.17}$$

$$I_Y\ddot{\theta}_Y^{mass} + c_Y\dot{\theta}_Y^{mass} - \frac{k}{2}(\theta_X^{mass} - \theta_Y^{mass} + \varepsilon\cos(2\pi\Omega t + p) - \beta) = \frac{T}{2}. \tag{A.18}$$

(b) Freeplay :

$$I_X\ddot{\theta}_X^{mass} = -c_X\dot{\theta}_X^{mass} + T, \tag{A.19}$$

$$I_Y\ddot{\theta}_Y^{mass} = -c_Y\dot{\theta}_Y^{mass}. \tag{A.20}$$

(c) Y-shaft drives X-shaft (torque reversal) :

$$I_X\ddot{\theta}_X^{mass} + c_X\dot{\theta}_X^{mass} + \frac{k}{2}(\theta_X^{mass} - \theta_Y^{mass} + \varepsilon\cos(2\pi\Omega t + p) + \beta) = \frac{T}{2}, \tag{A.21}$$

$$I_Y\ddot{\theta}_Y^{mass} + c_Y\dot{\theta}_Y^{mass} - \frac{k}{2}(\theta_X^{mass} - \theta_Y^{mass} + \varepsilon\cos(2\pi\Omega t + p) + \beta) = \frac{T}{2}. \tag{A.22}$$

(Note that when the gears are in contact the motor torque is divided equally between the equations for θ_X^{mass} and θ_Y^{mass}.)

In addition to these equations, we must calculate the conditions for the gears to re-establish contact from freeplay. To find this condition we must find the first time τ at which $\theta_X^{out} = \theta_Y^{out} \pm \beta$. From (A.10) and (A.11) we observe that this is equivalent to finding the first time τ at which

$$\theta_X^{in} - \theta_Y^{in} = \pm\beta - \varepsilon\cos(2\pi\Omega\tau + p). \tag{A.23}$$

From (A.12) the condition for re-contact can be calculated as

$$\theta_X^{mass} - \theta_Y^{mass} = \pm\beta - \frac{T}{k} - \varepsilon\cos(2\pi\Omega\tau + p). \tag{A.24}$$

For algebraic convenience we introduce a new variable Φ such that

$$\Phi = \theta_{\mathrm{X}}^{\mathrm{mass}} - \theta_{\mathrm{Y}}^{\mathrm{mass}} + \varepsilon\cos(2\pi\Omega\tau + p) + \frac{4\pi c\Omega}{k}. \tag{A.25}$$

Therefore the condition for re-contact can be expressed, as for the lumped model by

$$\Phi = \pm\beta. \tag{A.26}$$

For each pair of equations in each regime we then subtract the ODE for $\theta_{\mathrm{Y}}^{\mathrm{mass}}$ from the corresponding ODE for $\theta_{\mathrm{X}}^{\mathrm{mass}}$. Substituting for Φ, and assuming $I_{\mathrm{X}} = I_{\mathrm{Y}} =: I$ and $c_{\mathrm{X}} = c_{\mathrm{Y}} =: c$, yields the three ODEs:

(a) X-shaft drives Y-shaft,

$$I\ddot{\Phi}+c\dot{\Phi}+k\Phi = 4\pi c\Omega+k\beta-2\pi c\Omega\varepsilon\sin(2\pi\Omega\tau+p))-4\pi^2\Omega^2 I\varepsilon\cos(2\pi\Omega\tau+p). \tag{A.27}$$

(b) Freeplay,

$$I\ddot{\Phi} + c\dot{\Phi} = 4\pi c\Omega - 2\pi c\Omega\varepsilon\sin(2\pi\Omega\tau + p)) - 4\pi^2\Omega^2 I\varepsilon\cos(2\pi\Omega\tau + p). \tag{A.28}$$

(c) Y-shaft drives X-shaft,

$$I\ddot{\Phi}+c\dot{\Phi}+k\Phi = 4\pi c\Omega-k\beta-2\pi c\Omega\varepsilon\sin(2\pi\Omega\tau+p))-4\pi^2\Omega^2 I\varepsilon\cos(2\pi\Omega\tau+p). \tag{A.29}$$

If we non-dimensionalise with the rotation period, as before, we recover the same ODEs (2.27), (2.28) and (2.29), up to a factor of two in the stiffness coefficient k. The discrepancy arises because of where the stiffnesses are measured.

A.1 Round-up discussion

(From Mike Galtry, Edwards Ltd)

> "Most vacuum systems with Roots boosters spend a significant proportion of their life running at ultimate pressure, with the booster in an unloaded condition. Thus, intermittent gear noise is an issue for all vacuum pump manufacturers. The impact of this issue is increased with the trend towards faster rotation of the Roots booster and for larger system sizes. Intermittent behaviour is always very difficult to investigate experimentally and therefore an analytical approach identifying the cause of the problem has proved of value. This has enabled Edwards Ltd. to take relatively low cost approaches to address the intermittent noise issue as well as develop more expensive solutions for those systems that present greater challenges."

References

[1] `http://www.edwardsvacuum.com/`. Website of Edwards Ltd.

[2] Dry pumps and boosters. BOCE training handout from the "Practical Vacuum Technology" course.

[3] `http://www.maplesoft.com/`. Maple software package.

[4] `http://www.mathworks.com/`. Matlab software package.

[5] A. Back, J. Guckenheimer, M.R. Myers, F.J. Wicklin, and P.A Worfolk. DsTool: Computer assisted exploration of dynamical systems. *Notices of the American Mathematical Society*, 39:303–309, 1992.

[6] C.J. Budd and F. Dux. Chattering and related behaviour in impact oscillators. *Philosophical Transactions of the Royal Society of London A*, 347:365–389, 1994.

[7] C.J. Budd and F. Dux. Intermittency in impact oscillators close to resonance. *Nonlinearity*, 7:1191–1224, 1994.

[8] C.J. Budd, F. Dux, and A. Cliffe. The effect of frequency and clearance variations on single-degree-of freedom impact oscillators. *Journal of Sound and Vibration*, 184:475–502, 1995.

[9] G. Dahlquist and A. Björck. *Numerical Methods.* Prentice-Hall, 1974.

[10] T. Davenne. BOC Edwards. Personal communications.

[11] T. Davenne. Calculation of critical eccentricity. Technical report, BOC Edwards, 2005.

[12] T. Davenne. Gear assembly. WO patent 2005093293, 2005.

[13] S.L.T. de Souza and I.L. Caldas. Basins of attraction and transient chaos in a gear-rattling model. *Journal of Applied Mechanics*, 7:849–862, 2001.

[14] S.L.T. de Souza, I.L. Caldas, R.L Viana, and J.M. Balthazar. Sudden changes in chaotic attractors and transient basins in a model for rattling in gear boxes. *Chaos, Solitons and Fractals*, 21:763–772, 2004.

[15] S.L.T. de Souza, I.L. Caldas, R.L Viana, A.M. Batista, and T. Kapitaniak. Noise-induced basin hopping in a gearbox model. *Chaos, Solitons and Fractals*, 26: 1523–1531, 2005.

[16] M. di Bernardo, C.J. Budd, and A.R. Champneys. Grazing, skipping and sliding: analysis of the nonsmooth dynamics of the DC/DC buck converter. *Nonlinearity*, 11:858–890, 1998.

[17] M. di Bernardo, C.J. Budd, A.R. Champneys, and P. Kowalczyk. *Piecewise-smooth Dynamical Systems: Theory and Applications.* Springer-Verlag, 2007.

[18] S.H. Doole and S.J. Hogan. A piecewise linear suspension bridge model: nonlinear dynamics and orbit continuation. *Dynamical Systems*, 11:19–47, 1996.

[19] J.E. England, B. Krauskopf, and H.M. Osinga. Computing one-dimensional stable manifolds of planar maps without the inverse. *SIAM Journal of Applied Dynamical Systems*, 3:161–190, 2004.

[20] M. Gray. BOC Edwards. Personal communications.

[21] J. Guckenheimer and P. Holmes. *Nonlinear Oscillations, Dynamical Systems, and Bifurcations of Vector Fields.* Springer-Verlag, 1983.

[22] M.H. Hablanian. Design and performance of oil-free pumps. *Vacuum*, 41:1814–1818, 1990.

[23] C.K. Halse. *Nonlinear Dynamics of the Automotive Driveline.* PhD thesis, University of Bristol, 2004.

[24] C.K. Halse, R.E. Wilson, M. di Bernardo, and M.E. Homer. Coexisting solutions and bifurcations in mechanical oscillators with backlash. *Journal of Sound and Vibration*, 305:854–885, 2007.

[25] N.S. Harris. *Modern Vacuum Practice.* McGraw-Hill, 1990.

[26] W.T. Holmes. *Plane Geometry of Rotors in Pumps and Gears.* The Scientific Publishing Company, 1978.

[27] C.S. Hsu. *Cell-to-Cell Mapping. A Method of Global Analysis for Nonlinear Systems.* Springer-Verlag, 1987.

[28] C.S. Hsu and R.S. Guttalu. An unravelling algorithm for global analysis of dynamical systems: An application of cell-to-cell mappings. *Journal of Applied Mechanics*, 47:940–948, 1980.

References

[29] A. Kahraman and G. Blankenship. Effect of involute contact ratio on spur gear dynamics. *Journal of Mechanical Design*, 121:112–118, 1999.

[30] K. Karagiannis and F. Pfieffer. Theoretical and experimental investigations of gear-rattling. *Nonlinear Dynamics*, 2:367–387, 1991.

[31] B. Krauskopf and H.M. Osinga. Investigating torus bifurcations in the forced Van der Pol oscillator. In E.J. Doedel and L.S. Tuckerman, editors, *Numerical Methods for Bifurcation Problems and Large-Scale Dynamical Systems*, pages 198–208. Springer-Verlag, 2000.

[32] Y.A. Kuznetsov. *Elements of Applied Bifurcation Theory.* Springer-Verlag, 2003.

[33] H. Lamba and C.J. Budd. Scaling of Lyapunov exponents at nonsmooth bifurcations. *Physical Review E*, 50:84–90, 1994.

[34] G. Litak and M.I. Friswell. Dynamics of a gear system with faults in meshing stiffness. *Nonlinear Dynamics*, 41:415–421, 2005.

[35] P. Long. Gear measurement and resetting instructions. Technical report, BOC Edwards, 2003.

[36] J.F. Madden. Constant frequency bifilar vibration absorber. US patent 4218187, 1980.

[37] J.F. Mason. Mathematical modelling of gear rattle in dual-shaft vacuum pumps. Master's thesis, University of Bristol, 2004.

[38] J.F. Mason, M.E. Homer, and R.E. Wilson. Mathematical models of gear rattle in Roots blower vacuum pumps. *Journal of Sound Vibration*, 308:431–440, 2007.

[39] J.F. Mason, P.T. Piiroinen, R.E. Wilson, and M.E. Homer. Basins of attraction in nonsmooth models of gear rattle. *To appear in the International Journal of Bifurcation and Chaos*, 2009.

[40] H.E. Merritt. *Gear Engineering.* Pitman Publishing, 1971.

[41] T.M. Nester, A.G. Haddow, S.W. Shaw, J.E. Brevick, and V.J. Borowski. Vibration reduction in variable displacement engines using pendulum absorbers. In *Proceedings of the SAE Noise and Vibration Conference and Exhibition*, 2003.

[42] D.E. Newland. Nonlinear aspects of the performance of centrifugal pendulum vibration absorbers. *Journal of Engineering for Industry*, 86:257–263, 1964.

[43] A.B. Nordmark. Personal communications.

[44] A.B. Nordmark. Non-periodic motion caused by grazing incidence in an impact oscillator. *Journal of Sound and Vibration*, 2:279–297, 1991.

[45] A.B. Nordmark and P.T. Piiroinen. Simulation and stability analysis of impacting systems with complete chattering. *To appear in Nonlinear Dynamics*, 2009.

[46] G. Osorio, M. di Bernardo, and S. Santini. Chattering and complex behaviour of a cam-following system. In *Proceedings of European Nonlinear Oscillations Conference*, 2005.

[47] J.R. Ottewill, R.E. Wilson, and S.A. Nield. An experimental analysis of the dynamics of lightly damped subcritically excited gear pairs. In *International Design Engineering Technical Conferences and Computers and Information in Engineering Conference*. American Society of Mechanical Engineers, 2007.

[48] H.N. Özgüven and D.R. Houser. Mathematical models used in gear dynamics – a review. *Journal of Sound and Vibration*, 121:383–411, 1988.

[49] A. Parey and N. Tandon. Spur gear dynamic models including defects: a review. *The Shock and Vibration Digest*, 35:465–478, 2003.

[50] M. Sharif-Bakhtiar and S.W. Shaw. The dynamic response of a centrifugal pendulum vibration absorber with motion-limiting stops. *Journal of Sound and Vibration*, 126:221–235, 1988.

[51] S.W. Shaw. Personal communications.

[52] S.W. Shaw, P.M. Schmitz, and A.G. Haddow. Tautochronic vibration absorbers for rotating systems. *Journal of Computational and Nonlinear Dynamics*, 1:283–293, 2006.

[53] S. Theodossiades and S. Natsiavas. Non-linear dynamics of gear-pair systems with periodic stiffness and backlash. *Journal of Sound and Vibration*, 229:287–310, 2000.

[54] W.T. Thomson. *Theory of Vibration with Applications*. Chapman and Hall, 1993.

[55] P. Thota and H. Dankowicz. TC-HAT ($\widehat{\text{TC}}$) : A novel toolbox for the continuation of periodic trajectories in hybrid dynamical systems. *SIAM Journal of Applied Dynamical Systems*, 7:1283–1322, 2008.

[56] A.P. Troup and N.T.M. Dennis. Six years of "dry pumping": A review of experiences and issues. *Journal of Vacuum Science and Technology A*, 9:2048–2052, 1990.

References

[57] R.E. Wilson and A.R. Champneys. Confidential report prepared for BOC Edwards Phase 1. Technical report, Bristol Laboratory for Advanced Dynamics Engineering, 2003.

[58] R.E. Wilson and A.R. Champneys. Confidential report prepared for BOC Edwards Phase 2. Technical report, Bristol Laboratory for Advanced Dynamics Engineering, 2003.

[59] H. Wycliffe. Mechanical high-vacuum pumps with oil-free swept volume. *Journal of Vacuum Science and Technology A*, 5:2608–2611, 1987.

UNIVERSITY OF BRISTOL LIBRARY